



저작자표시-비영리-변경금지 2.0 대한민국

이용자는 아래의 조건을 따르는 경우에 한하여 자유롭게

- 이 저작물을 복제, 배포, 전송, 전시, 공연 및 방송할 수 있습니다.

다음과 같은 조건을 따라야 합니다:



저작자표시. 귀하는 원저작자를 표시하여야 합니다.



비영리. 귀하는 이 저작물을 영리 목적으로 이용할 수 없습니다.



변경금지. 귀하는 이 저작물을 개작, 변형 또는 가공할 수 없습니다.

- 귀하는, 이 저작물의 재이용이나 배포의 경우, 이 저작물에 적용된 이용허락조건을 명확하게 나타내어야 합니다.
- 저작권자로부터 별도의 허가를 받으면 이러한 조건들은 적용되지 않습니다.

저작권법에 따른 이용자의 권리는 위의 내용에 의하여 영향을 받지 않습니다.

이것은 [이용허락규약\(Legal Code\)](#)을 이해하기 쉽게 요약한 것입니다.

[Disclaimer](#)

공학박사학위논문

**Strain-induced dynamical  
heterogeneity and local viscoelastic  
behavior in complex fluids**

변형에 의한 복잡유체의 동적불균일성 및  
미세유변학적 특성에 관한 연구

2014년 2월

서울대학교 대학원

화학생물공학부

강희경



# **Abstract**

## **Strain-induced dynamical heterogeneity and local viscoelastic behavior in complex fluids**

Heekyoung Kang

School of Chemical and Biological Engineering

The Graduate School

Seoul National University

When stress or strain is applied to the complex fluids, they exhibit unusual mechanical responses due to the geometrical hindrances that the phase coexistence induces. Their rheological properties can be attributed to characteristics such as highly disorder, caging, and clustering on multiple length scales. With it, the dynamics of complex fluids receives attentions as it's deeply related to the microstructure and rheological property. To supplement the conventional rheometry, we suggest particle tracking microrheology using direct visualization as an alternative. Using this method,

we can observe the local viscoelastic behavior of materials as well as the dynamics on micron length scale. As a first step, we verify the experimental setup of microrheology with totally homogeneous materials such as various polymer solutions by comparing with the results from conventional rheometer. Then, as a second step, we try to control a step of developing mechanism of biofilms by measuring rheological properties of biofilms. It composed with extracellular polymeric substances (EPS) and bacterial cells which have been known to show viscoelastic behavior and have heterogeneous microstructures. From measuring the mean square displacements (MSDs) on the micro-scale, the dynamical heterogeneities of the biofilms are evaluated using van Hove correlation function and non-Gaussian parameter. The dynamical heterogeneity of the biofilms decreased as the wall shear rate increased, analogizing the structural heterogeneity of the biofilms on the different wall shear rate. By determining the local  $G'$  and  $G''$  at the low wall shear rate, the structures of biofilms are characterized as void, loose and dense network structures respectively. These kinds of structural diversity in the biofilms give a strong dynamical heterogeneity at low wall shear rate. In contrast, the narrow distribution of MSDs at the high wall shear rate was caused by the dense structure of biofilms. This result clearly gives the strong point of particle tracking microrheology on localized

measurement. Finally, as a third step, we modified the previous microrheological method to report the effect of dynamical heterogeneity on the theoretical modeling of nonlinear elastic modulus and Brownian stress of colloidal depletion gels that have undergone yielding in high-rate step strains by modifying previous tracking method on the open system. When we apply step strains to colloidal gels with short-ranged depletion attraction using simple shear equipment, we find the existence of a subpopulation of slow and fast particles. Within this flow regime, small aggregates of particles connected by weak bonds are broken, leaving behind a network consisting of slowly-diffusing particles. These slow clusters form rigid cores that contribute to the remnant stress supported by the sample. Based on this observation, we compare the measured rheology to the theoretical elastic modulus calculated only with the localization length of the slow clusters. We find that this approach produces a far better agreement between theory and experiment. In this thesis, the dynamical heterogeneity of complex fluids gives a vehicle to characterize the structural heterogeneity under varied shear stress. Finally, the findings in this study set the importance of dynamical heterogeneity in the rheology of complex fluids such as bacterial community biofilms and depleting colloidal gels.

**Keywords:** particle tracking microrheology, complex fluids, bacterial community biofilms, depleting colloidal gels, dynamical heterogeneity, structural heterogeneity, local viscoelasticity, microstructure, shear stress, Mode Coupling Theory, nonlinear elasticity

**Student Number:** 2007-21170

# Contents

Abstract.....	i
List of Contents.....	v
List of Tables.....	ix
List of Figures.....	x
1. Introduction.....	1
1.1. Microrheology.....	1
1.2. Controlling the bacterial biofilms .....	5
1.3. Dynamics of post-yielding colloidal gels.....	9
1.4. Outline of the thesis .....	12
2. Theory.....	16
3. Materials and methods.....	27
3.1. Polymer solutions.....	27
3.1.1. Materials preparation.....	27



3.1.2.	Tracking process.....	29
3.1.3.	Rotational rheometry.....	30
3.2.	Bacterial community biofilms.....	31
3.2.1.	Model bacterial strain.....	31
3.2.2.	Experimental setup for measuring bacterial motion on the surface.....	31
3.2.3.	Additional data processing on the bacterial motion.....	36
3.2.4.	Experimental setup for measuring viscoelastic property of biofilms.....	38
3.2.5.	Measurement 3D structure of biofilms using CLSM.....	40
3.3.	Depleting attractive colloidal gels.....	42
3.3.1.	Preparation of colloidal gels.....	42
3.3.2.	Static and dynamic error.....	46
3.3.3.	Experimental setup and procedures.....	49
3.3.4.	Correction of drift velocity.....	50
4.	Verification of the particle tracking microrheology.....	56
4.1.	The slope of the MSD curves.....	56
4.2.	Dynamic moduli.....	62

5. Controlling and removal of the bacterial community biofilm	71
5.1. The dynamics of bacteria on the anodic electrode	71
5.1.1. Effect of current density on bacterial displacement	71
5.1.2. Effect of ionic strength on displacement of PAO1s	83
5.1.3. Applicability for biofilm control	86
5.2. The local viscoelastic behavior of biofilms	90
5.2.1. Effect of $\dot{\gamma}_{at\ the\ wall}$ applied during developing phase on the dynamical heterogeneities in biofilms	90
5.2.2. The local dynamics at low $\dot{\gamma}_{at\ the\ wall}$ (88.9/s)	95
5.2.3. The local dynamics at high $\dot{\gamma}_{at\ the\ wall}$ (237.0/s)	103
6. Dynamics of post-yielding colloidal gels	110
6.1. The MSD curves of post-yielding colloidal gels	110
6.2. Strain-induced dynamical heterogeneities in colloidal gels	113
6.3. Modulus-dynamics relationship	118
7. Conclusions	129

Bibliography.....	132
국문요약.....	147
Curriculum Vitae.....	151

# List of Tables

<b>Table 1.1.</b> Type of microrheology.....	3
<b>Table 1.2.</b> Type and characteristics of passive microrheology.....	4
<b>Table 4.1.</b> Modulus coefficient ( $G_j$ ) and relaxation time coefficient ( $\tau_j$ ) obtained from Maxwell model for PEO solution (MW 2M). Two modes were used for 2.0wt% solution. ....	64

# List of Figures

<b>Figure 2.1.</b> The principle of microrheology.....	21
<b>Figure 2.2.</b> The basic scheme of microrheology.....	23
<b>Figure 2.3.</b> The van Hove correlation function of 1.2 wt% PEO aqueous solution (M.W. 600k) at the $\Delta t = 0.033, 0.33, 1.0,$ and $5.0$ s. The solid line showed the Gaussian fitting. Inset: the non-Gaussian parameter ( $\alpha_2(\tau)$ ) as a function of $\Delta t$ .....	25
<b>Figure 3.1.</b> The rate sweep test of 2M PEO solutions using conventional rheometer (ARES) .....	28
<b>Figure 3.2.</b> (a) The representative image of bacterial cells adhered on the glass surface, (b) the schematic of flow chamber. ....	32
<b>Figure 3.3.</b> The LSV measurement to confirm the oxygen evolution potential under anodic electric field in three electrodes system with Ag/AgCl (sat. KCl) as reference electrode.....	34
<b>Figure 3.4.</b> (a) The schematic of experimental setup for incubate biofilms. (b) The representative images of the biofilms at $(1.3 \times 1.3\text{mm})$ from Confocal microscope and $(80 \mu\text{m} \times 80 \mu\text{m})$ observing view from up-light microscope.....	41

<b>Figure 3.5.</b> The synthesized PMMA particle obtained by SEM.....	43
<b>Figure 3.6.</b> Gelation, phase separation and interaction potentials.....	44
<b>Figure 3.7.</b> (a) The general curves of overall force for our system calculating using the Asakura and Oosawa equation with different depleting polymer concentration. (b) The MSD curves of colloidal gels with increased $c/c^*$ ...	45
<b>Figure 3.8.</b> (a) The 2D images (b) The MSD curves (c) van Hove correlation function of quiescent colloidal gels as increasing waiting time to create gel structure at $c/c^*=0.375$ .....	47
<b>Figure 3.9.</b> (a) van Hove correlation function (b) non-Gaussian parameter of quiescent colloidal gels as increasing waiting time to create gel structure at $c/c^*=0.375$ .....	48
<b>Figure 3.10.</b> (a) The custom-built shearing device to apply the shear stress to the colloidal gels. (b) the scheme of the experimental setup.....	50
<b>Figure 3.11.</b> Rate sweep test using rotational type conventional rheometer (AR-G2) of quiescent colloidal gels.....	51
<b>Figure 3.12.</b> van Hove correlation function of pre-(open symbol) and post-(closed symbol) correction of drift velocity.....	53
<b>Figure 3.13.</b> Verification of correction code. (a) trajectories of probe	

particles before and after applying correction code (b) the MSD curves of before and after correction.....55

**Figure 4.1.** Mean square displacement of PEO (MW 2M) aqueous solutions with varied concentration (0.04 – 3.0 wt%).....57

**Figure 4.2.** The slope of MSD curve as a function of polymer concentration for MW 2M PEO (▲), MW 600k PEO (●) and MW 5-6M PAA (◇). The slope is from sub-diffusion region,  $\Delta t \leq 0.2$  s.....59

**Figure 4.3.** The relation between the slope of MSD curve at short times from microrheology measurements and  $G'$  at 10 rad/s from bulk rheometry as a representative degree of elasticity.....61

**Figure 4.4.** Dynamic moduli of PEO (MW 2M) solution from particle tracking microrheology using Euler's equation ( $\Delta$ , ▲), Maxwell model ( $\circ$ , ●) and from conventional rheometry ( $\square$ , ■). Closed symbols are storage modulus, and open symbols are loss modulus. (a) 0.4 wt%, (b) 1.0 wt%.....63

**Figure 4.5.** Comparison of dynamic moduli of PEO (MW 2M) aqueous solution obtained from particle tracking microrheology with those from bulk rheometry: (a)  $G'$  (b)  $G''$  at concentration of 0.1 wt% (●), 0.4 wt% (▲,  $\Delta$ ), 1.0 wt% (■,  $\square$ ) and 2.0 wt% solution (◆, ◇). Closed symbols are from

particle tracking microrheology, and open symbols are from conventional rheometry.....66

**Figure 4.6.** Comparison of dynamic moduli of PEO (MW 600k) solution from particle tracking microrheology with those from bulk rheometry: (a)  $G'$  (b)  $G''$  at concentration of 0.3 wt% (●), 1.0 wt% (▲, △), 1.5 wt% (■, □) and 3.0 wt% solution (◆, ◇). Closed symbols are from particle tracking microrheology, and open symbols are from conventional rheometry.....68

**Figure 4.7.** Comparison of dynamic moduli of PAA (MW 1-2M) solution from particle tracking microrheology with those from bulk rheometry: (a)  $G'$  (b)  $G''$  at concentration of 0.1 wt% (●), 0.7 wt% (▲, △), 1.0 wt% (■, □), and 5.0 wt% solution (◆, ◇). Closed symbols are from particle tracking microrheology, open symbols are from conventional rheometry.....69

**Figure 5.1.** (a) Averaged mean square displacement (MSD) of bacterial cells on an anode surface depending on current densities at an ionic strength of 20 mM. (b) Averaged  $\sqrt{MSD}$  of bacterial cells moving on an anode surface or  $\Delta t = 10$  s as a function of current density.  $N = 3$ ; SD shown.....73

**Figure 5.2.** MSD curves of individual bacterial cells on the whole bacterial community on an anode surface at an ionic strength of 20 mM at current density of (a)  $7.5 \mu\text{A}/\text{cm}^2$  and (b)  $30 \mu\text{A}/\text{cm}^2$ . To show the curves distinguished, the MSD curves of 20 bacterial cells were selected randomly among 200 bacterial cells in each plot.....75



**Figure 5.3.** Trajectories of bacterial cells moving on an anodic surface at ionic strength of 20 mM at various current densities captured for 50 s at a frame rate of 30 Hz. The x and y axes are the directional coordinates, and each point is the centroid of an individual bacterium. The number of bacteria is  $200 \pm 50$  /picture. (a) Current density =  $7.5 \mu\text{A}/\text{cm}^2$  , (b)  $15 \mu\text{A}/\text{cm}^2$  , (c)  $22.5 \mu\text{A}/\text{cm}^2$  , and (d)  $30 \mu\text{A}/\text{cm}^2$ .....77

**Figure 5.4.** Movement of bacterial cells under cathodic and anodic electrodes, and the detachment mechanism suggested by Poortinga et al.....79

**Figure 5.5.** The distributions of  $\sqrt{MSD}$  of bacterial cells moving on an anode surface for 10 s at current densities of  $7.5 \mu\text{A}/\text{cm}^2$  (●) and  $30 \mu\text{A}/\text{cm}^2$  (★) at an ionic strength of 20 mM. The lines are fitted distributions with the Weibull distribution function (equation (3.1)) expressed using scale parameter ( $\lambda$ ) and shape parameter ( $k$ ).....81

**Figure 5.6.** The  $\sqrt{MSD}$  of bacterial cells moving on an anodic surface for 10 s depending on ionic strength 10 - 50 mM at a current density of  $15 \mu\text{A}/\text{cm}^2$ . These data were calculated from equation (2.15), and averaged for every set of data. ....83

**Figure 5.7.** The Schematic to show the effect of ionic strength on the anodic surface.....85

**Figure 5.8.** Confocal laser scanning microscopy (CLSM) images acquired after 24 h of biofilm growth (scale bar: 50  $\mu\text{m}$ ), (a) biofilms growth under

non electric field, (b) biofilm growth under applied electric current ( $15 \mu\text{A}/\text{cm}^2$ ).....87

**Figure 5.9.** The microstructure of biofilms depending on wall shear rate

( $\dot{\gamma}_{at\ the\ wall} = \frac{3Q}{2(h_0/2)^2 w_0}$ ) during developing phase controlling by flow rate of

nutrient solution which obtained using Confocal laser scanning microscope (CLSM) on the observing view with  $1.3 \text{ mm} \times 1.3 \text{ mm}$ . (a)  $\dot{\gamma}_{at\ the\ wall} = 38.5$ , (b) 65.2, (c) 88.9, (d) 118.5, (e) 177.8, (f) 237.0 /s. The green color showed the bacterial cells and red color showed the fluorescent particles dispersed inside biofilms for tracking.....90

**Figure 5.10.** (a) Non-Gaussian parameter ( $\alpha_{2\_x}$ ) on the vorticity direction

under varied  $\dot{\gamma}_{at\ the\ wall}$  (38.5 - 237.0 /s) calculated from equation (2.25) using particle tracking microrheological method on the observing view ( $80 \mu\text{m} \times 80 \mu\text{m}$ ) after 24 h developing to show the dynamical heterogeneity. (b) Averaged  $\alpha_2$  at  $\Delta t=1\text{s}$  under varied  $\dot{\gamma}_{at\ the\ wall}$  (38.5 - 237.0 /s) with x- (vorticity) and y-axis (flow). On each  $\dot{\gamma}_{at\ the\ wall}$ , we selected four different regions randomly inside biofilms to get a representative value and calculate the error bar. ....92

**Figure 5.11.** The MSD plots of individual particles over time inside

observing view ( $80 \mu\text{m} \times 80 \mu\text{m}$ ). (a) Biofilms at  $\dot{\gamma}_{at\ the\ wall} = 88.9$  /s, at a height of  $20 \mu\text{m}$  and at ages of 24 h. They are classified to three groups of particles (A1, A2, and A3) where their positions according to the slope of

MSD curve and order of MSD. (b) MW 600k Polyethylene oxide (PEO) 1.2 wt% aqueous solution as a reference material.....94

**Figure 5.12.** A spatial map of mechanical microenvironments of the particle trajectories inside biofilm structure. The each color means the one particle’s motion for 10 s. There is no long-range spatial correlation, suggesting that the length scale of heterogeneity is small—of the order of a particle diameter. (MSD: Mean Square Displacement).....96

**Figure 5.13.** The average viscoelastic moduli of biofilm after 19 h ( $\Delta$ ,  $\blacktriangle$ ) and 24 h ( $\circ$ ,  $\bullet$ ) obtained using particle tracking microrheological measurement at height = 20  $\mu\text{m}$  from the glass surface. Closed symbol for storage modulus ( $G'$ ), and open symbol for loss modulus ( $G''$ ). Inset: The slope of MSD curve during developing phase at height = 10  $\mu\text{m}$  from the surface. (MSD: Mean Square Displacement).....98

**Figure 5.14.** The local viscoelastic moduli from particle tracking microrheology calculated with individual MSD plot of Figure 5.11(a) at  $\dot{\gamma}_{at\ the\ wall} = 88.9$  /s inside observing view (80  $\mu\text{m}$   $\times$  80  $\mu\text{m}$ ). (a)  $G'$ (closed symbol) and  $G''$ (open symbol) for region A1(circle), A2(triangle), and A3(square) as shown in Figure 5.11(a) were calculated from the Euler’s equations (equation (2.20)). The error bar was calculated with the individual MSDs at each region. (b) Dynamic viscosity  $|\eta^*|$  was calculated using equation (2.24) from Figure 5.14(a).....100

**Figure 5.15.** The MSD tracks of individual particles over time inside

observing view ( $80 \mu\text{m} \times 80 \mu\text{m}$ ) biofilms at  $\dot{\gamma}_{\text{at the wall}} = 237 \text{ /s}$ , at a height of  $20 \mu\text{m}$  and at ages of 24 h. (a) Region A  $\dot{\gamma}_{\text{at the wall}} = 237 \text{ /s}$  with averaged  $\alpha_2 = 0.75$ , and (b) Region B  $\dot{\gamma}_{\text{at the wall}} = 237 \text{ /s}$  with averaged  $\alpha_2 = 2.48$ . Region A  $\dot{\gamma}_{\text{at the wall}} = 237 \text{ /s}$ : The MSD curves showed gel-like motion. Region B  $\dot{\gamma}_{\text{at the wall}} = 237 \text{ /s}$ : They are classified to two groups of particles (B1 and B2) where their positions according to the slope of MSD curve and order of MSD.....102

**Figure 5.16.** Van Hove correlation function at  $\dot{\gamma}_{\text{at the wall}} =$  (a)  $88.9 \text{ /s}$ , and (b)  $237 \text{ /s}$  at  $\Delta t = 1 \text{ s}$ . The results were calculated using all dispersed probe particles in the observing view with ( $80 \mu\text{m} \times 80 \mu\text{m}$ ) at each region. The solid line fitted the Gaussian distribution at each van-Hove correlation function. (a) the data of MSDs were used from region A  $\dot{\gamma}_{\text{at the wall}} = 88.9 \text{ /s}$  ( $\alpha_2 = 20.0$ ) in Figure 5.11(a). (b) the van Hove correlation function of two representative regions ( $\alpha_2 = 0.75$  (A  $\dot{\gamma}_{\text{at the wall}} = 237 \text{ /s}$ ) and  $2.48$  (B  $\dot{\gamma}_{\text{at the wall}} = 237 \text{ /s}$ )) was plotted separately as shown in Figure 5.15. The van Hove correlation function of MW 600k PEO 1.2 wt% aqueous solution was suggested as a reference set (see Figure 2.3).....105

**Figure 6.1.** Mean-squared displacement (MSD) curves of colloidal gels after applying a step strain with  $\gamma = 0.1$  to  $80$  at  $\dot{\gamma} = 40 \text{ s}^{-1}$ . (a) Evolution of  $\langle x^2 \rangle$  as a function of  $\Delta t$  from a completely arrested gel state (black open symbols) to a completely fluidized suspension (solid line), with the following applied deformations:  $\gamma = 0.1$ ,  $\gamma = 0.6$ ,  $\gamma = 6.0$ ,  $\gamma = 30$ , and  $\gamma = 80$ . Closed black

symbols represent static noise level obtained from photo-polymerized sample.

(b) Localization lengths in the  $x$  (vorticity) directions as a function of strain for  $\Delta t = 9.78, 20.2,$  and  $40.4$  s. Error bars shown here are standard deviations from 3 independent measurements.....110

**Figure 6.2.** Superimposed bimodal single particle displacement distributions of sheared colloidal gels showing slow and fast subpopulations. Comparison between the  $G_s(\Delta t = 9.78$  s) of quiescent colloidal gels (purple open symbols) and that of gels sheared at (a)  $\gamma = 0.1,$  (b)  $\gamma = 6.0,$  and (c)  $\gamma = 80.$  Red closed symbols represent data for gels that have undergone yielding, with Gaussian distributions fit to their slow (solid line) and fast (dashed line) subpopulation of particles.....113

**Figure 6.3.** Self-part of van Hove correlation for all strains.....115

**Figure 6.4.** The non-Gaussian parameter ( $\alpha_2$ ) of post-yielding colloidal gels under varied strain (0.1-80) .....116

**Figure 6.5.** MSD curves for slow and fast particles in sheared colloidal gels. The change in localization length of fast-moving particles ( $\langle r^2_{\text{fast}}(\Delta t) \rangle,$  open symbols) versus slowly-diffusing aggregates ( $\langle r^2_{\text{clust}}(\Delta t) \rangle,$  closed symbols) as a function of  $\gamma,$  for  $\Delta t = 9.78$  s,  $20.2$  s, and  $30.0$  s.....118

**Figure 6.6.** Relative abundance of fast particles as a function of  $\gamma,$  obtained from Gaussian fits to  $G_s(\Delta t = 9.78$  s) for the fast subpopulation.....120

<b>Figure 6.7.</b> Strain sweep raw data. Error bars are standard deviations. (Working on replication of lower frequencies).....	122
<b>Figure 6.8.</b> Stress relaxation raw data for all strains.....	123
<b>Figure 6.9.</b> $G_B$ defined as the Brownian stress measured immediately after the cessation of the step strain.....	124
<b>Figure 6.10.</b> Comparison of bulk rheological measurements to theoretical predictions from MCT-PRISM. The experimental measurements consist of: 1) the elastic modulus from oscillatory strain sweep normalized by the linear value at $\gamma = 0.1$ , for $\omega = 0.1$ rad/s (red), 1.0 rad/s (orange), 10 rad/s (green), and 40 rad/s (purple); and 2) the Brownian stress from stress relaxation measurements, normalized by the linear value at $\gamma = 0.1$ , after application of a step strain (blue closed symbols). Errors bars are standard deviations from the mean. The theoretical predictions are that from the combined MSD from slow and fast particles (open triangles), and from the MSD of the slow subpopulation (solid line) at $\Delta t = 9.78$ s. Dashed line represents the confidence interval of the theoretical prediction based on standard deviations carried over from the MSD values.....	126



# 1. Introduction

## 1.1. Microrheology

Conventional rheometry is widely used to characterize the viscoelastic behavior of the complex fluids. However, it is difficult to precisely determine their rheological properties when the viscosity of the fluid is not high enough to induce sufficient signal that the equipment can detect reliably. Dilute polymer solutions or dilute suspensions fall under this case. In addition, we can only obtain averaged properties over finite size of measuring geometry with conventional rheometry. Hence it fails to detect local variation of properties in heterogeneous systems such as biological cell, biopolymer, and colloidal suspension, where locally variable information could be critical to describe their bulk behavior.

To overcome these limitations of bulk rheometry, microrheology has been developed in recent decades. Microrheology is the rheology in micron size domain, and therefore has advantages over bulk rheometry on detecting weak signal and heterogeneity. First of all, sample volume required for experiment is small, in the order of several micro-liters. Hence it has strength in determining rheological properties of biological samples, which are mostly expensive and prepared by only limited volume. Second,



microstructure of the sample is not destroyed during experiment with this method since very small or no external force is applied to the sample during the test. The third advantage of microrheology technique is extended range of frequency applicable in dynamic measurements. For example, applicable range of frequency reaches  $10^4$  Hz for semi-flexible polymers using diffusing wave spectroscopy (DWS) technique [1]. Fourth, the local heterogeneity of the material in micro scale can be exclusively examined using microrheology, through small observing window adopted in the method. With these advantages, microrheology has been found more suitable method to determine the rheological properties of dilute suspension [2], semi-flexible polymer solution [3], polymer gel [4], wormlike micellar solution [5, 6] and biological materials such as F-actin [7, 8] and live cells [1, 9]. Also, particularly with the advantage of being able to detect heterogeneity, the change in rheological properties during polymerization or gelation has been determined using microrheology technique [4, 10].

Microrheology is separated to two categories, active and passive methods depending on the existence of external force exerted on the test domain. Particle tracking microrheology technique used in this study is one of passive methods, which exploits the Brownian motion of the tracing particles in a test material to obtain local rheological properties of it. Compared to other

**Table 1.1.** Type of microrheology

Passive microrheology	Active microrheology
Thermal fluctuation	External force
Video particle tracking	Magnetic tweezer
Laser deflection	Optical tweezer
Diffusing wave spectroscopy	AFM

**Table 1.2.** Type and characteristics of passive microrheology

Video particle tracking	<ul style="list-style-type: none"> <li>- Low temporal and spatial resolution</li> <li>- Preserves individual particle information and tracking of many particles at a time</li> <li>- Sample's viscoelasticity and local heterogeneity can easily be determined</li> <li>- Simple apparatus required compared to DWS or LDPT</li> </ul>
Laser deflection	<ul style="list-style-type: none"> <li>- Weak powered laser is used as interferometer</li> <li>- Detect the movement of particle from beam's axis</li> <li>- Extremely high temporal and spatial resolutions</li> <li>- Ensemble averaging is difficult</li> <li>→ limitations in quantitative analysis</li> </ul>
DWS	<ul style="list-style-type: none"> <li>- Utilizes multiple scattering from monodisperse colloidal probe particles</li> <li>- Intensity fluctuations of scattered light</li> <li>→ dynamics of medium</li> <li>- Fast and high resolution</li> <li>- Individual probe particle information is lost</li> <li>- Local heterogeneity data can not be obtained</li> </ul>

microrheological methods, apparatus of particle tracking microrheology is relatively simple and easier to setup. Also, the local information of each particle in medium can be individually traced, unlike DWS technique, the other passive method.

However, the performance of microrheological method has rarely been verified systematically using various materials. Most of previous studies suggested results of one model polymer solution to verify the performance of the method [1, 8, 11-14]. Though Breedveld and Pine [15] derived an effective upper limit for the viscosity and/or elasticity applicable to microrheology technique based on the distance a probe particle travels during measurement and on the resolution of visualization equipment, it was only theoretical work and they did not verify the results experimentally.

## **1.2. Controlling the bacterial biofilms**

Biofilms are complex aggregate of microorganisms surrounded by the slime they secrete. It is composed of bacteria, void and extracellular polymeric substances (EPS). Bacteria adhered on the surface induce biofilms by producing extracellular polymeric substances at surface [16-21]. In many environments, such as underwater structures [22], membrane processes for water treatment [23-25], foods [26], and biomedical applications [27], the

control of biofilm growth is of major importance, because EPS lead to undesirable effects. For examples, bacterial biofilm prevents the flow of materials inside pipeline and often causes infection on the surface of medical devices like catheters and prosthetics. Besides, the developing mechanism of biofilms needs to be understood, because the biofilms are a kind of ways to control the pollutants in the water during water treatment process. To remove biofilms effectively, understanding film-forming mechanism and mechanical properties of biofilms is essential. Biofilms are developed by three steps: first step is attachment of bacteria, and then growth of EPS and finally, detachment of bacteria. In this study, we tried to control the bacterial community biofilms with two kinds of method, the one is applying electric current on the adhered bacteria and the other is measuring the local viscoelastic behaviors of biofilms.

There are several biofilms control techniques, but approaches for controlling bacterial adhesion by the application of electric fields have attracted wide attention, because it is an environmentally friendly method, which can be conveniently applied to any solid surface [28, 29]. The electrical approach typically uses a low electric current to control bacterial motility via external forces. Different bacterial motilities have been observed at cathode and anode [30]. Under cathodic polarization the electrophoretic

motility of bacteria is the major factor contributing to bacterial detachment. The bacterial surface mainly carries a net negative charge, so the electrostatic repulsive force between bacteria and the cathodically polarized electrode overcomes the bacterial adhesive force to a surface, thereby resulting in bacterial detachment [31]. Bacterial detachment by cathodic polarization is known to be influenced by environmental conditions, such as electric current density and ionic strength [29]. In contrast, the oscillating motion of bacteria and bacterial inactivation under anodic polarization has been suggested as mechanisms of bacterial detachment [30, 32]. The oscillating motion of bacteria accompanied by shear stress diminishes bacterial adhesion force and promotes bacterial detachment [30]. The bacterial motility might influence the microstructural development of the biofilm as well as bacterial adhesion. Thus, the characterization of bacterial motility on an electrode surface is important for effective biofilm control, but quantitative information on bacterial motion has not been reported, especially under the influence of an anodic electric field.

As the second method to control biofilms, the rheological measurement has been suggested. Although biofilms contain DNA and protein, the most part is composed with polysaccharides. Based on this component, biofilms are the representative materials showing viscoelastic behavior [33-35]. There

are many researches about resistance of biofilms to the flow [21, 36-42]. Here, it's important to know the structure of biofilms and kinetic behavior which are dependent on the applied shear stress [37, 40, 42, 43]. Therefore, the rheological properties of biofilms need to study along with structural properties under varied shear stress [33, 36].

The structural changes by external stress (shear stress or environmental stress such as concentration of salt) have been reported [36, 40, 43, 44]. Stewart et al. have suggested the cellular connectivity ( $\sim 6 \mu\text{m}$ ) is decreased by environmental stress which compared to the unstressed biofilms ( $\sim 30 \mu\text{m}$ ) [36]. Liu et al. and Vieira et al. have researched that the biofilms forms thinner and more compact structure under increased shear stress applied during growth phase [43, 44]. On the other hand, Paris et al. have shown that the biofilms develop more heterogeneous structure at higher  $\dot{\gamma}_{at\ the\ wall}$  as the high  $\dot{\gamma}_{at\ the\ wall}$  cause the rise of the cellular concentration adhered to the surface [45]. In this way, although the researches of bulk structure such as thickness have been progressed, there have been not many researches that state the structural and dynamical heterogeneities in biofilms.

People have designed some method to measure the rheological properties of biofilms, especially, using bulk rheology or simulation method. At first, in case of simulation method, there is a limitation to model the physiological

bacteria perfectly since they show more complex mechanism than particles. There have been studies on measuring mechanical properties of biofilm using conventional rotational rheometer. But, in this case, the microstructure of biofilm can be destroyed due to large oscillation. Also, the heterogeneity of biofilm structure cannot be characterized, nor the developing process of biofilm cannot be observed using this conventional bulk rheometry. To overcome these disadvantages Rogers et al. selected microrheology as a novel method, and measured the local compliance of *Staphylococcus aureus* and *Pseudomonas aeruginos* biofilms in vitro [46]. However, because they track the bacteria's dynamics, the results might have included the motion caused by flagella along with the Brownian motion [46-49]. Then, it can cause some error to calculate the compliance of biofilms. Also, in case of *Pseudomonas aeruginosa* which are the rod-shape cell, the Brownian motion of ellipsoidal particle show different aspect with the one of sphere [50]. Therefore, in our study we try to apply the microrheological method by dispersing probe particles inside biofilms instead of tracking bacteria's dynamics.

### **1.3. Dynamics of post-yielding colloidal gels**



Colloidal depletion gels are formed by the addition of a non-adsorbing polymer to particles suspended in a solvent to generate short-ranged attractive interactions [51]. The solid-like properties imparted by colloidal gels are used in a variety of applications such as nanoemulsions, tissue scaffolding, membranes, and printing [52-56], where the relationship between microstructure and rheology is particularly rich and not fully understood. Colloidal gels and glasses are known to undergo yielding under an externally applied flow, in which they can exhibit large structural changes [57-62]. Rupture is a complex phenomenon that is highly dependent on the structural and dynamical heterogeneity of the system. Attractive glasses and gels are known to display two clear signatures associated with bond and cage breaking [59, 63, 64]. When sheared, they 'shed' their outer layer of particles that are weakly bonded, leaving behind rigid clusters that contribute to the measured rheology [58, 64]. Multiple experimental observations of soft pivot points in gels also relate to this hypothesis [60, 65, 66]. The coupling between microstructure and particle dynamics has been studied for many quiescent colloidal systems, especially when traversing phase boundaries [67]. However, particle dynamics have not been investigated at the high shear rates required for significant structural breakup.

Mode coupling theory (MCT) has been extended from the regime of super-cooled fluids to the colloidal realm, and has shown reasonable success in describing the inverse relationship between the linear rheology and the mean squared displacement of particles in colloidal gels [68, 69]. However, due to their ensemble-averaging assumption that all particles within the system contribute equally to the elastic stress, they often over-predict the measured rheology in non-homogenous systems. Models that distinguish particle-level from cluster-level contribution to the modulus in heterogeneous glasses have shown good agreement between the theoretical and experimental shear modulus [70].

In this thesis, we extend the idea that particles in sheared colloidal gels can be categorized based on their mean-squared displacement, and that only slow moving clusters can support an elastic stress in shear flow. This local dynamical heterogeneity has been previously observed in quiescent gels, where a divergence of slow and fast particles exist close to the gelation transition [71]. These simulation results are experimentally supported by confocal microscopy of quiescent colloidal suspensions with attractive interactions [72, 73]. In sheared depletion gels, diffusing wave spectroscopy studies show that colloids remain in clusters that exhibit convection motion even after flow ceases [69]. The existence of dynamical heterogeneity

suggests that ensemble-averaged theories, as MCT, may not accurately describe the divergence in local dynamics of colloidal suspensions under shear.

## **1.4. Outline of the thesis**

The objectives of this study are to measure the local dynamics in complex fluids using particle tracking microrheological method, and to quantify strain-induced dynamical heterogeneities which induced by microstructural change under varied shear stress.

In section 2, the theory of particle tracking microrheology will be introduced.

In section 3, the test materials and the experimental protocol will be detailed.

In section 4, prior to apply the microrheological method to the complex fluids, we need to verify the experimental setup of particle tracking microrheology with totally homogeneous materials. Therefore, we compare the zero shear viscosity and dynamic moduli of polymer solutions with varying concentration, experimentally determined by particle tracking microrheology and conventional rheometry. The dynamic moduli calculated using Maxwell model and Euler's equation are compared to those from bulk

rheometry Also, the relation between the slope of mean square displacement and storage modulus are suggested. Based on these results, we conclude our findings on applicable range of microrheology technique in obtaining rheological properties of any material.

In section 5.1, we try to quantify the translational displacement of a bacterial community under an anodic electric field using a particle tracking method. The particle tracking method, which has been originally used for rheological analysis, was selected for characterizing bacterial motion [30, 74, 75], because the tracking method is simple to set up and allows the comparison of the motilities of several strains [74]. This technique provides quantitative information on the behavior of individual motile bacteria, including the trajectories of bacterial motion [30]. The translational displacement of bacteria was measured quantitatively in terms of 2 variables, that is, amplitude of current density and ionic strength. The displacements of a large number of bacteria were measured and the directional properties of bacterial motion (circular or oscillating) were identified. The dynamics of a bacterial community observed under an anodic electric field is discussed in terms of the electro-hydrodynamic force and the electro-osmotic force. The possible application of this method with respect to the control of biofilm growth was also partly demonstrated.

In section 5.2, we try to quantify the dynamical heterogeneities of biofilms on micron length scale under varied  $\dot{\gamma}_{atthewall}$ . Firstly, we measured the 3D images of biofilms using Confocal Laser Scanning Microscope (CLSM) by changing  $\dot{\gamma}_{atthewall}$  during growth phase. At the same time, the dynamical heterogeneities of biofilms were evaluated with van Hove correlation function and non-Gaussian parameter for each  $\dot{\gamma}_{atthewall}$  obtained from particle tracking microrheological method. To see the relation with  $\dot{\gamma}_{atthewall}$  and dynamical heterogeneity, the local viscoelasticity was calculated using Euler's equation with microrheological results. Based on these results, we discussed the effect of  $\dot{\gamma}_{atthewall}$  to the structural and dynamical heterogeneity of biofilms.

In section 6, we modified the previous particle tracking microrheological method to apply for the open material system with the weak external flow. Then, we measure the strain-dependent dynamics of colloidal gels using confocal microscopy and calculate the linear elastic modulus from mode coupling theory – polymer reference interaction side model (MCT-PRISM) [68, 76]. By separating the bimodal dynamics that we observe in sheared samples, we find that our corrected predictions are in much better agreement with our experimental measurements. Then, we tested the modulus-dynamics

relationship suggested by Chen and Schweizer theory using the strain dependent localization length. Based on our results, we discussed the limitation of the Chen and Schweizer theory for dynamics of the yielded depleting colloidal gels. Also, previous yielding mechanisms that explain structure rupture at initial state of yielding were compared with our results [68, 76].

In section 7, above researches are summarized.

## 2. Theory

Probe particles embedded in the solution experience two kinds of forces if external force is not applied: Brownian random force and frictional force.

From the equation of motion, the formula becomes:

$$m \frac{dv(t)}{dt} = f_R(t) - \zeta v(t) \quad (2.1)$$

,where the  $m$  is mass of particle,  $v(t)$  is particle velocity,  $f_R(t)$  is Brownian force. When the probe particles were dispersed in a viscoelastic medium, equation (2.1) was modified as generalized Langevin equation. This equation considers inertia with Brownian and frictional forces. In this case, convolution integral include the elasticity as well as viscosity by relating previous velocity effect to the current frictional force [49]:

$$m \frac{dv(t)}{dt} = f_R(t) - \int_0^t \zeta(t-t')v(t')dt' \quad (2.2)$$

,where  $\zeta(t)$  is a memory function. The Brownian force in this equation was assumed to be a Gaussian random variable with zero mean displacement and to be completely decoupled from previous velocity [49]. Here, frictional force was consisted of convolution integral of memory function and velocity to make the viscous damping. From this process, the energy can be stored

and returned to the elasticity of the medium.

To calculate convolution integral of equation (2.2), the Laplace transform was taken on both side of the generalized Langevin equation:

$$mv(0)(s\tilde{v}(s) - v(0)) = v(0)\tilde{f}_R(s) - v(0)\tilde{\zeta}(s)\tilde{v}(s) . \quad (2.3)$$

In case of time scale on the general particle tracking, the inertia term could be neglected [11] because our observation time was longer than the relaxation time of the particle in a fluid. Then, this equation was taken:

$$-\langle mv(0)v(0) \rangle = \langle v(0)\tilde{f}_R(s) \rangle - \langle v(0)\tilde{\zeta}(s)\tilde{v}(s) \rangle \quad (2.4)$$

And we could substitute particle kinetic energy to the temperature of the system derived from the equipartition theory:

$$m\langle v(0)v(0) \rangle = m\langle v(t)v(t) \rangle = k_B T \quad (2.5)$$

,where  $k_B$  is the Boltzman constant , and T is the temperature.

As the Brownian force was decoupled with the past velocity and its mean was zero displacement which was derived from equipartition theory, the equation (2.5) was simplified to this equation:

$$k_B T = \langle v(0)\tilde{\zeta}(s)\tilde{v}(s) \rangle \quad (2.6)$$

The right-hand side of equation (2.6) was velocity autocorrelation function that could be obtained from the second order derivative of the mean square displacement [77]:



$$\langle v(0)v(t) \rangle = \frac{1}{6} \left[ \frac{\partial^2 \langle \Delta r^2(t) \rangle}{\partial t^2} \right], \quad \langle \tilde{v}(0)\tilde{v}(s) \rangle = \frac{s^2 \langle \Delta \tilde{r}^2(s) \rangle}{6} \quad (2.7)$$

From the equation (2.6), the memory function was substituted to the mean square displacement of a particle like this:

$$\tilde{\zeta}(s) = \frac{k_B T}{\langle v(0)\tilde{v}(s) \rangle} = \frac{6k_B T}{s^2 \langle \Delta \tilde{r}^2(s) \rangle} \quad (2.8)$$

Then, to get the linear viscoelastic modulus, we used macroscopic stress-strain rate relation and their Laplace transform:

$$\begin{aligned} \tau(t) &= \int_0^t G_r(t-t') \dot{\gamma}(t') dt' \\ \tilde{\tau}(s) &= s \tilde{G}_r(s) \tilde{\gamma}_s(s) \end{aligned} \quad (2.9)$$

,where is  $\tau(t)$  is the stress,  $G_r(t)$  is the relaxation modulus, and  $\dot{\gamma}(t)$  is the strain rate.

The linear viscoelastic modulus in the Laplace space was the coefficient of relation between stress and strain rate:

$$\tilde{G}(s) = s \tilde{G}_r(s). \quad (2.10)$$

For the spherical particle dispersed in a fluid, friction force could be calculated from the following equation with an approximation that the Newtonian viscosity could be replaced to the viscoelastic modulus [12]:

$$F = 6\pi\eta a v_\infty = 6\pi G_r(t) v_\infty \quad (2.11)$$

,where  $v_\infty$  is relative velocity of the fluid, and  $a$  is the particle radius.

By applying the Laplace transform to equation (2.11), we could find the relationship between the modulus and memory function:

$$\tilde{G}(s) = \frac{\tilde{\zeta}(s)}{6\pi a} \quad (2.12)$$

When we put the equation (2.12) and (2.10) into equation (2.8), the generalized Stokes-Einstein equation was like this [13]:

$$\tilde{G}(s) = s\tilde{G}_r(s) = \frac{k_B T}{\pi a s \langle \Delta \tilde{r}^2(s) \rangle} \quad (2.13)$$

where  $s$  is Laplace frequency and  $k_B$  is the Boltzmann constant. Here, several approximations should be applied. First, physical properties around the particle were homogeneous, which was satisfied if the particle size was sufficiently large compared to the characteristic length of a fluid [78]. Second, no-slip boundary condition was applied at the interface of probe particle and the test fluid. Third, material should be dilute suspension of spherical particle in a purely viscous medium at zero frequency, following Stokes law [49].

Equation (2.13) related MSD to modulus defined in the Laplace space. Therefore, if we track particles immersed in a sample and calculate their Laplace transformed MSD, we could get relaxation modulus after inverse

Laplace transformation of the modulus calculated from the generalized Stokes-Einstein equation.

Using Bessel function, mean square displacement of a probe particle in Laplace domain could be transformed to time domain, resulting [79]:

$$G(s) = \frac{k_B T}{\pi a \langle r^2(\Delta t) \rangle \Gamma[1 + (\partial \ln \langle r^2(\Delta t) \rangle / \partial \ln(\Delta t))]} \Big|_{t=\frac{1}{s}} . \quad (2.14)$$

From experimental results, MSD is calculated by taking ensemble average on 2D coordinates of particle centroid in the tracking results [11] :

$$\langle \Delta r^2(t) \rangle = \langle [x(t + \Delta t) - x(t)]^2 + [y(t + \Delta t) - y(t)]^2 \rangle . \quad (2.15)$$

This value for individual particle is again averaged over at least 1,000 particles. When MSD is plotted against lag time  $\Delta t$ , the slope is one for Newtonian fluid following this relation [49] :

$$\langle r^2(\Delta t) \rangle = 2nD\Delta t = 4D\Delta t . \quad (2.16)$$

In contrast, the slope is less than one for viscoelastic fluid due to sub-diffusive motion of probe particle, resulting [49]:

$$\langle r^2 \rangle = 2nDt^\beta \quad (0 < \beta < 1) . \quad (2.17)$$

For purely elastic solid, the slope is zero. In this study, maximum  $\Delta t$  adopted is 10 s, because the number of data becomes insufficient for statistically meaningful data processing above 10 s.

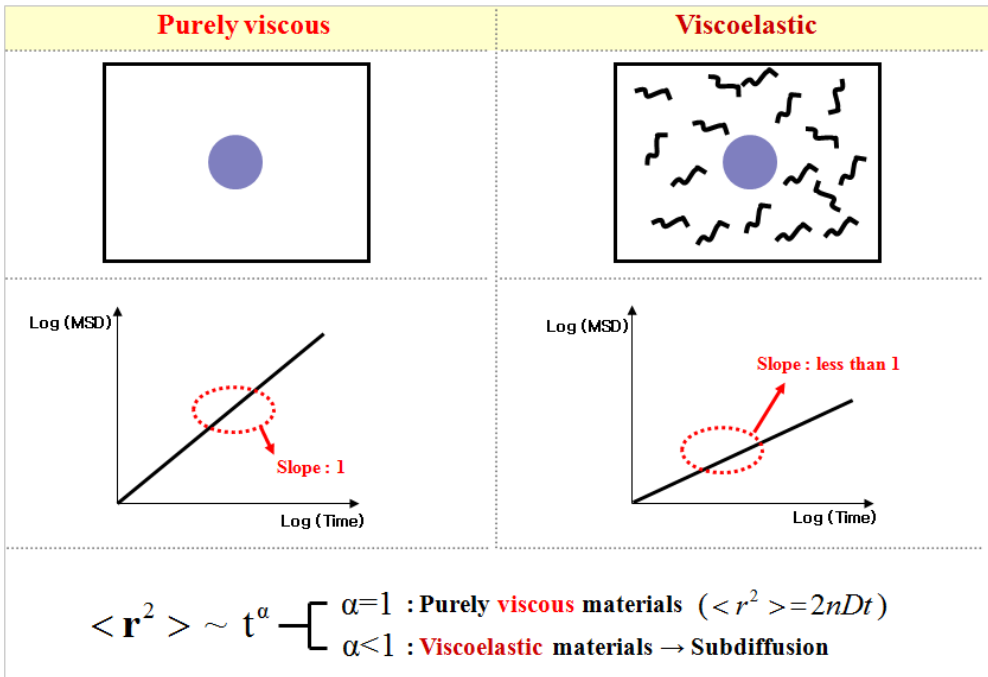


**Figure 2.1.** The basic principle of microrheology.

The resulting MSD from equation (5) is substituted to equation (4) to lead  $G(s)$  from experiment and it is nonlinearly fitted to the following equation [49]:

$$G(s) = \sum_j \frac{G_j s}{(s+1/\tau_j)} \quad (2.18)$$

From the fitting, modulus coefficient  $G_j$  and relaxation time coefficient  $\tau_j$  of each mode  $j$  are determined.

In the next step, viscoelastic models are applied to describe the material function. In this study, Maxwell model and Euler's equation were chosen since these have been most frequently adopted in previous studies [49, 78, 79]. Multiple-mode Maxwell model for dynamic moduli are:

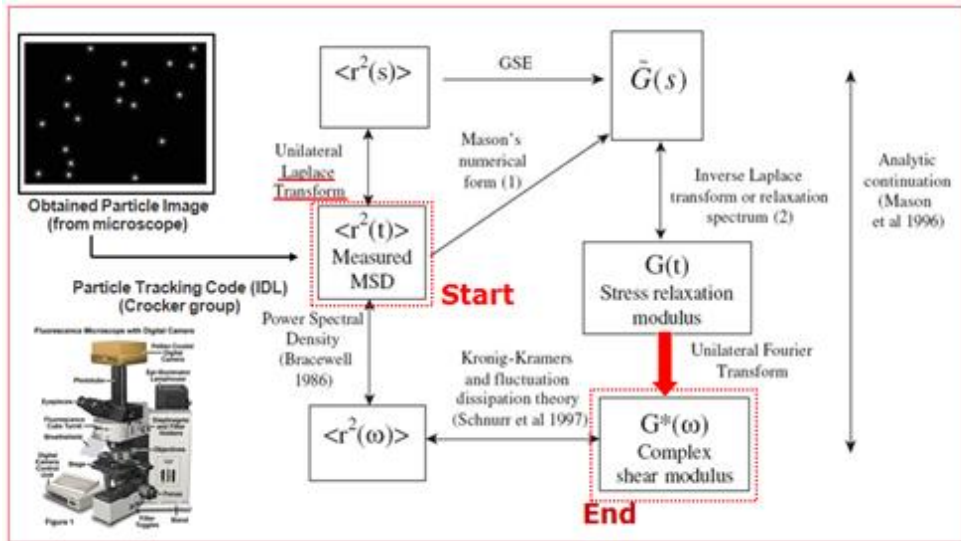
$$G'(\omega) = \sum_j G_j \frac{\omega^2 \tau_j^2}{1 + \omega^2 \tau_j^2} \quad , \text{ and} \quad (2.19.1)$$

$$G''(\omega) = \sum_j G_j \frac{\omega \tau_j}{1 + \omega^2 \tau_j^2} \quad , \quad (2.19.2)$$

where  $\omega$  is frequency.

Euler's equation for dynamic moduli is relatively simple form with single mode [79]:

$$G'(\omega) = |G^*(\omega)| \cos(\pi\alpha(\omega)/2) \quad (2.20.1)$$



MSD plotting  $\longrightarrow G(s) = \frac{k_B T}{\pi a \langle r^2(t) \rangle \Gamma[1 + (\partial \ln \langle \Delta r^2(t) \rangle / \partial \ln t)]} \Big|_{t=1}^s \longrightarrow G(s) = \sum_j \frac{G_j s}{(s + 1/\tau_j)}$ ,

$$G_r(t) = \sum_j G_j e^{-t/\tau_j} \quad G'(\omega) = \sum_j G_j \frac{\omega^2 \tau_j^2}{1 + \omega^2 \tau_j^2}, \quad G''(\omega) = \sum_j G_j \frac{\omega \tau_j}{1 + \omega^2 \tau_j^2} \longleftarrow$$

**Figure 2.2.** The basic scheme of microrheology [12]

$$G''(\omega) = |G^*(\omega)| \sin(\pi\alpha(\omega)/2) . \quad (2.20.2)$$

For these models, the modulus obtained from experimental data using equation (4) is fitted to the absolute value of complex modulus in the model:

$$|G^*(\omega)| \approx \frac{k_B T}{\pi a \langle r^2 \rangle (1/\omega) > \Gamma[1 + (\partial(\omega))]} \quad (2.21)$$

,where the slope of MSD curve becomes:

$$\partial(\omega) = \frac{\ln \langle \Delta r^2(\Delta t) \rangle}{\ln(\Delta t)} . \quad (2.23)$$

And the dynamic viscosity is calculated [80]:

$$|\eta^*| = \sqrt{\left(\frac{G'}{\omega}\right)^2 + \left(\frac{G''}{\omega}\right)^2} . \quad (2.24)$$

Also, to show the dynamical heterogeneity on the micron length scale, van Hove correlation function ( $G_s(\Delta x, \tau)$ ) and non-Gaussian parameter ( $\alpha_2(\tau)$ ) is used [67, 81]:

$$G_s(\Delta x, \tau) = \frac{1}{N} \left\langle \sum_{i=1}^N \delta[x + x_i(0) - x_i(\tau)] \right\rangle = \frac{N(\Delta x, \tau)}{N}, \text{ and} \quad (2.25)$$

$$\alpha_{2-x}(\tau) = \frac{\langle x^4(\tau) \rangle}{3 \langle x^2(\tau) \rangle^2} - 1 \text{ with } \langle x^b(\tau) \rangle = \sum_{i=1}^N x_i^b(\tau) G_s(\Delta x, \tau) \quad (2.26.1)$$

$$\alpha_{2-y}(\tau) = \frac{\langle y^4(\tau) \rangle}{3 \langle y^2(\tau) \rangle^2} - 1 \text{ with } \langle y^b(\tau) \rangle = \sum_{i=1}^N y_i^b(\tau) G_s(\Delta y, \tau) \quad (2.26.2)$$

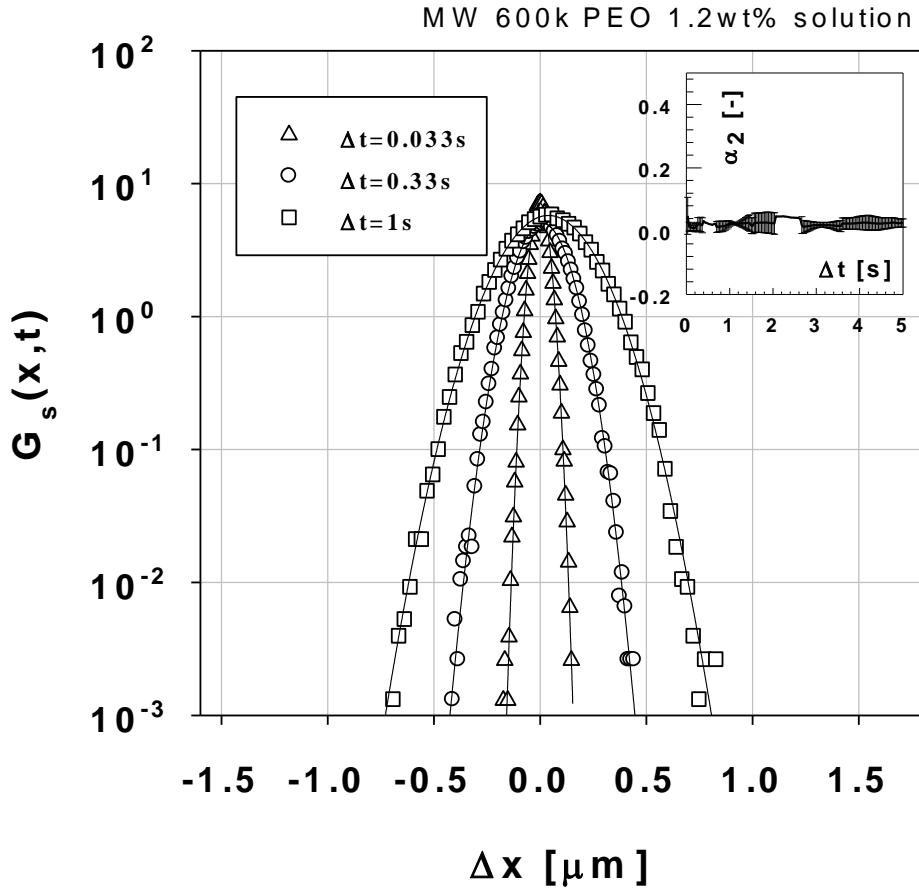


**Figure 2.3.** The van Hove correlation function of 1.2 wt% PEO aqueous solution (M.W. 600k) at the  $\Delta t = 0.033, 0.33, 1.0,$  and  $5.0$  s. The solid line showed the Gaussian fitting. Inset: the non-Gaussian parameter ( $\alpha_2(\tau)$ ) as a function of  $\Delta t$ .



In case of homogeneous materials like well dispersed polymer solution, the probability distribution is well fitted with the Gaussian function, and  $\alpha_2(\tau)$  is close to 0. We carried out the particle tracking microrheological experiment with MW 600k PEO 1.2 wt% aqueous solution as a reference of homogeneous materials (see, Figure 2.3). In contrast, in case of heterogeneous materials such as biofilm, the probability distribution is deviated from the Gaussian function, and  $\alpha_2(\tau)$  is started 20 at small  $\Delta t$  as shown in Figure 5.10 [72]. Also, we calculated dynamical heterogeneity on the vorticity direction ( $\alpha_{2_x}(\tau)$ ) and flow direction ( $\alpha_{2_y}(\tau)$ ) separately by substituting the mean square displacement on two direction  $\langle \Delta x^2 \rangle$  and  $\langle \Delta y^2 \rangle$  in equation (2.15). Using these parameters, the dynamical heterogeneity of biofilm can be quantified on the micro-bead length scale using particle tracking microrheology.

## **3. Materials and methods**

### **3.1. Polymer solutions**

#### **3.1.1. Material preparation**

Two different semi-flexible aqueous polymer solutions with varying molecular weight were used as model viscoelastic fluids. One is poly (ethylene oxide) (PEO, Sigma Aldrich) with two different molecular weights of 2,000,000 and 600,000, and the other is poly (acryl amide) (PAA, Sigma Aldrich) with molecular weight of 1-2,000,000. Solutions were prepared in deionized water by gentle mixing and rolling for 24 hours to avoid degradation of polymer chain. Then polystyrene fluorescent particles modified with carboxylate (Molecular Probes, U.S.A) were added to each polymer solution to give 0.01 wt% solid content. Fluorescence particles were provided in dilute and well-dispersed suspension state (2 wt% solid in distilled water and 2 mM azide) with exciting wave length of 580 nm and emitting wave length of 605 nm. The diameter of the probe particle was 1  $\mu\text{m}$  for low concentration solutions and 500 nm for higher concentration solutions. To disperse probe particles uniformly in polymer solutions and to prevent aggregation, polymer solutions with probe particles were ultra-

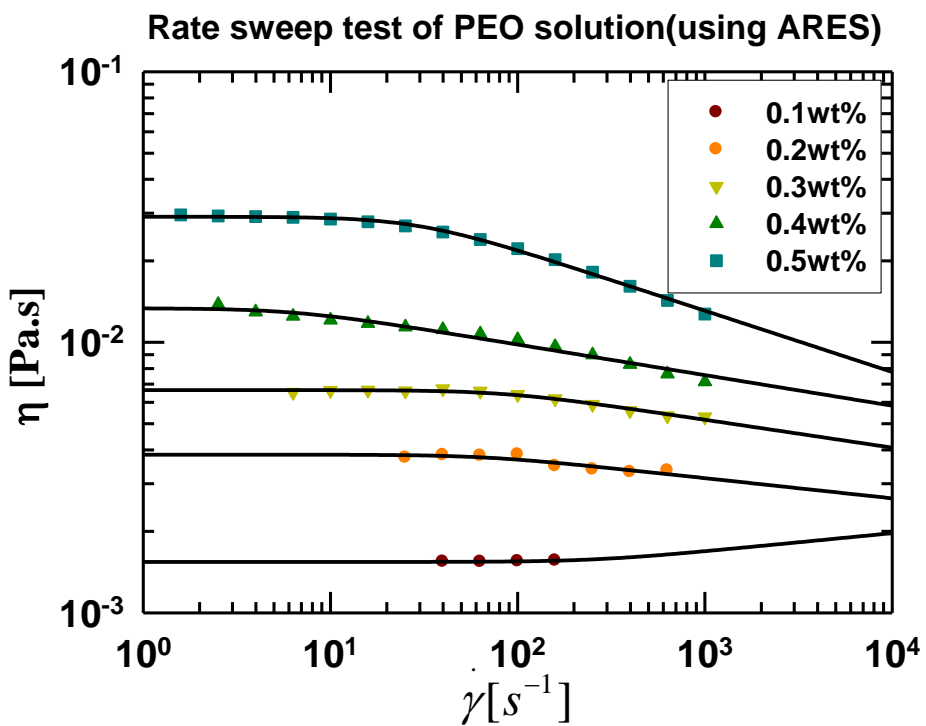


**Figure 3.1.** The rate sweep test of 2M PEO solutions using conventional rheometer (ARES)

sonicated for 5 min before each test.

### **3.1.2. Tracking process**

20  $\mu\text{l}$  of sample solution was loaded to a PC20 CoverWell cell (Grace Bio-Lab) to prevent drying and convectional flows during measurements, and it was mounted onto an inverted fluorescent microscope (IX-71, Olympus, Tokyo, Japan). 100 W mercury lamp was used as the light source and the images of Brownian motion of fluorescent particle under ambient temperature of  $25 \pm 2^\circ\text{C}$  were captured by electron-multiplier cooled CCD camera (C9100-02 Hamamatsu) with frame rate of 30 Hz. Exposure time was down to 500  $\mu\text{s}$ , shortest possible in the current setup to avoid blur of particle images and corresponding dynamic error [82]. CCD camera and PC computer were linked via high performance frame grabber board (PC-Camlink Coreco imaging) to transfer data in high speed without data loss. 3,000 frames were captured in sequence and it was repeated 10 times in each test condition to avoid errors from insufficient number of data points. Over measurement time, particles float freely and can move out of observing 2D plane to result in less number of data for longer measurement times. 1  $\mu\text{m}$  probe particles were observed using the 60X oil immersion type objective lens (Olympus, Tokyo, Japan) with numerical aperture of 1.40, while 500 nm

probe particles were observed using the 100X oil immersion type objective lens with numerical aperture of 1.42. The size of one pixel was 80 nm for 100X objective and 133 nm for 60X objective. Brownian motion of probe particles was analyzed by particle tracking code written in IDL language which was first developed by Crocker [83]. The code was slightly modified for particular purpose upon creator's permission.

### **3.1.3. Rotational rheometry**

The bulk rheological properties of polymer solutions were measured using cone and plate geometry on an ARES strain-controlled rheometer (TA Instruments). Steady shear viscosity and dynamic moduli of polymer solutions were determined using a 50 mm / 0.0398 rad cone with fixed gap of 0.0526 mm. Test temperature was set to be the same as in matching microrheology measurement.

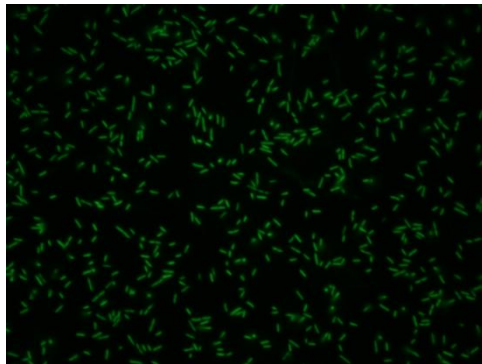
## **3.2. Bacterial community biofilms**

### **3.2.1. Model bacterial strain**

*Pseudomonas aeruginosa* PAO1 cells expressing green fluorescent protein (PAO1, Center for Biofilm Engineering, Montana State University, USA) were used as a model microorganism. Cells were cultured overnight in tryptic soy broth containing 100 µg/mL of carbenicillin at 37°C. PAO1 colonies formed on tryptic soy agar containing 100 µg/mL of carbenicillin were inoculated into a batch culture for 24 h. The PAO1 cells were then diluted into 20 mM potassium phosphate buffer (KH<sub>2</sub>PO<sub>4</sub>, pH 7.1) and adjusted to an optical density of 0.10 (600 nm). The zeta potential of PAO1 was measured as -20 mV using an ELS-8000 (Photal Otsuka Electronics, Japan) at 160 Hz and 80 V.

### **3.2.2. Experimental setup for measuring bacterial motion on the surface**

A flow chamber comprising of FC-81 flow cell (Bio Surface Technologies, USA) containing working and counter electrodes [32] was used as a batch reactor, and the experiments measuring bacterial movement were conducted in a no-flow condition. A transparent indium tin oxide [84] electrode was



(a)



Coverglass coated with ITO

→ working electrode (anode, 100  $\mu$ A)



phosphate buffered solution



Slideglass coated with ITO

(b)

**Figure 3.2.** (a) The representative image of bacterial cells adhered on the glass surface, (b) the schematic of flow chamber.

used as a working electrode to observe bacterial motion. ITO films (200 nm thick, 60 ohm/square) were deposited on a cover slip using a RF sputter (A Tech Co., Korea). ITO-coated glass (Samsung Corning, Korea) was also applied as a counter electrode (180 nm, 20 ohm/square). This flow chamber contains two electrodes without any reference electrode due to limited space. The area of the electrodes in contact with the electrolyte was  $6.5 \text{ cm}^2$ , and the distance between the electrodes was 3.0 mm. Both electrodes were connected with aluminum foil to a potentiostat (PARSTAT 263, Princeton Applied Research, USA). To examine the possible electrochemical reaction on each electrode, linear sweep voltammetry (LSV) was applied in a separate batch-type electrochemical cell using Ag/AgCl (sat. KCl) as a reference electrode. The distance between two electrodes was maintained identical with that in flow chamber with Ag/AgCl (sat. KCl) as reference electrode.

The flow chamber was stabilized by flowing bacteria-free potassium phosphate buffer (20 mM, pH 7.1) for 30 min, after which it was filled with bacterial solution for 10 min at a shear rate of  $1.11 \text{ s}^{-1}$  (flow rate = 1.3 mL/min) using a peristaltic pump (Gilson, USA) [20]. After the bacteria were allowed to adhere to the surface, the flow chamber was rinsed with bacteria-free potassium phosphate buffer to remove any floating cells, since the research is focused on the motion of adhered bacteria. Subsequently, the



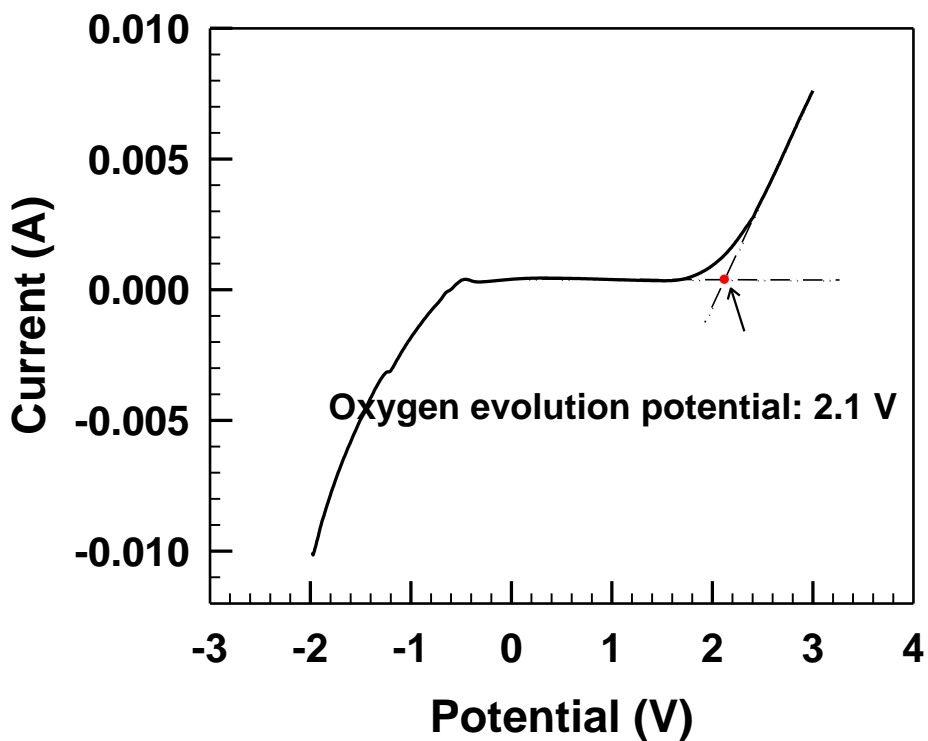


**Figure 3.3.** The LSV measurement to confirm the oxygen evolution potential under anodic electric field in three electrodes system with Ag/AgCl (sat. KCl) as reference electrode.

flow chamber was locked with nippers to maintain no-flow condition. Under an anodic electric current, 1,500 frames were captured at one sequence for 50 s. Two operating variables, amplitude of current density and ionic strength, were then controlled. Amplitude of current density varied from zero to 30  $\mu\text{A}/\text{cm}^2$  at an ionic strength of 20 mM without changing the bacterial solution in the flow chamber. Conversely, the ionic strength varied from 10 mM to 50 mM at a current of 15  $\mu\text{A}/\text{cm}^2$ . In each experiment, the measurements were repeated 5 times to obtain statistically meaningful data for the calculation of the mean square displacement (MSD). The potential between the two electrodes was measured as 2.4 V at 15  $\mu\text{A}/\text{cm}^2$ . All experiments were performed in triplicate under fixed experimental conditions using freshly adhered bacterial cells in order to obtain a representative MSD, which was reported as an average value with a standard deviation. According to previous studies, bacterial inactivation occurs upon long-time exposure to an anodic electric field [30, 31]. To examine the extent of bacterial cell inactivation, we employed a live/dead cell kit. The ratio of PAO1 inactivation was below 10% for each experiment, in which the MSD of more than 1,000 bacterial cells were measured at currents ranging from zero to 30  $\mu\text{A}/\text{cm}^2$ . Therefore, bacterial inactivation under an anodic electric field had only a negligible effect on the motion of the larger bacterial

community. This low ratio of bacterial inactivation may be due to the relatively short time of exposure to the electric field [31]. In addition, the effect on bacteria which were previously exposed to an electric field was examined. Adhered bacteria were completely eliminated from the flow chamber followed by refilling with fresh bacterial solution. The same experiments were then repeated and compared. The MSDs of the two experiments were not so different that the adhered bacteria exposed to the electric field could be used again. However, at high ionic strength (>30 mM), the flow chamber was refilled with fresh bacterial solution for every experiment to easily observe the fluorescence intensity of bacteria over long periods of time.

### **3.2.3. Additional data processing on the bacterial motion**

The motion of the bacterial community was quantified by the method that explained at the Sec.3.1.2. The results were calculated by tracking the centroids of bacteria cells, which are represented by the brightest pixel of each bacterium located near the cross point of the major and minor axes. The translational motion of PAO1s, except for rotational motion, was captured over a time period of 50 s. The number of bacteria adhered to the surface was  $200 \pm 50/\text{picture}$  or  $(1.18 \pm 0.3) \times 10^{10}/\text{cm}^2$ , which was kept constant for all

experiments. The MSD is the sum of square displacement, allowing better evaluation of the real distance travelled by bacteria. This value for an individual cell was again averaged over at least 1,000 bacteria.

Although all experiments were performed for 50 s, the MSD was obtainable for  $\Delta t = 10$  s in this study, since the MSD is normally obtainable for only 20 - 30% of the total measurement time [78]. Total measurement time of 50 s was necessary to increase the amount of data.

To better represent the characteristic motion of a bacterial community, the normalized distribution of  $\sqrt{MSD}$  of bacterial cells was obtained by dividing with the total number of bacteria at  $\Delta t = 10$  s. The Weibull distribution function as expressed in equation (3.1) was used to simulate the normalized distribution of  $\sqrt{MSD}$  of bacterial cells [85]:

$$f(\sqrt{MSD(t)}; \lambda; k) = \frac{k}{\lambda} \left( \frac{\sqrt{MSD(t)}}{\lambda} \right)^{k-1} e^{-(\sqrt{MSD(t)}/\lambda)^k} \quad (3.1)$$

where  $k$  is the shape parameter which express the shape of the distribution function, and  $\lambda$  is the scale parameter such that the larger the scale parameter, the more spread out of the distribution.

### 3.2.4. Experimental setup for measuring viscoelasticity of biofilms

Flow chamber used in this study is FC-271 flow cell (Bio Surface Technologies, Bozeman, MT), which was used as an experimental reactor. This flow cell was modified to capillary type (1-mm wide, 1.5-mm deep, 40-mm long) to prevent the bubble that might be created during flowing step. Flow chamber was mounted onto an inverted fluorescent microscope (IX-71, Olympus, Tokyo, Japan), and connected to pressure sensor and flow meter. This flow chamber is just used as a reactor, and the all experiment to measure the viscoelastic moduli were processed under non-flow state. At first, cell-free potassium phosphate buffer (20 mM, pH 7.1) was flowed for 30 min to stabilize inside flow chamber, and then the bacterial solution cultured overnight was flowed for 10 min at ambient temperature to make bacteria to adhere to the surface. The fluids were supplied at a  $\dot{\gamma}_{at\ the\ wall}$  of  $65.2\ s^{-1}$  (flow rate = 2.2 mL/min) via a peristaltic pump (Gilson, Middleton, WI) at adhesion step. The  $\dot{\gamma}_{at\ the\ wall}$  was calculated using the equation (3.2) for rectangular flow displacement system as described previously [20]:

$$\dot{\gamma}_{at\ the\ wall} = \frac{3Q}{2(h_0/2)^2 w_0} \quad (3.2)$$

where  $Q(m^3/s)$  is the volumetric flow rate,  $h_0(m)$  is the height and

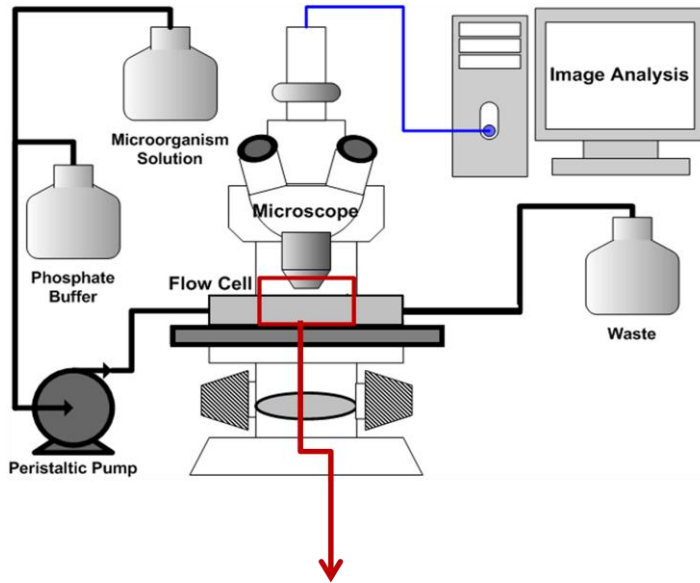
$w_0$  ( $m$ ) is the width of flow chamber.

Then, after stopping the flow, the flow chamber leaved for 4 h for bacteria to attach stably to surface of cover glass. Subsequently, the adhering bacteria was cultured in flowing 1/10-strength Tryptic Soy Broth (Becton, Dickinson and Company, USA) under varying  $\dot{\gamma}_{at\ the\ wall}$ . The  $\dot{\gamma}_{at\ the\ wall}$  of triptic soy broth solution during growth phase was controlled to characterize the microstructure of biofilm from 35.0 to 250.0  $s^{-1}$  (1.3 – 8.0 ml/min). In this state, polystyrene fluorescent particles modified with carboxylate (Molecular Probes, U.S.A) were flowed together. Fluorescence particles were provided in dilute and well-dispersed suspension state (2 wt% solid in distilled water and 2 mM azide) with exciting wave length of 580 nm and emitting wave length of 605 nm. The particles would be dispersed insides biofilm during growth phases. After 24 h, the flow chamber was washed with cell-free potassium phosphate buffer to remove the freely suspending cells and weakly adhering cells. The flow chamber was locked with nippers to measure the Brownian motion of probe particles without the forced flow. We sampled the dynamics of probe particles inside biofilms at the four different regions ( $80\ \mu m \times 80\ \mu m$ ) which were randomly selected at height of  $20\ \mu m$ , and at ages of 24 h. We defined the region of ( $80\ \mu m \times 80\ \mu m$ ) biofilms as

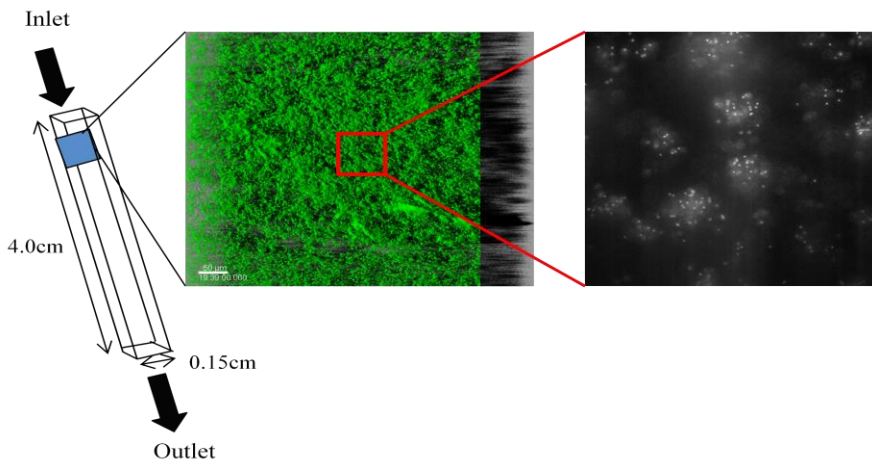
A, and the small spots within the A were defined A1, A2 and A3. This definition using capital letters was applied to the other region, also.

### **3.2.5. Measurement 3D structure of biofilms using CLSM**

Biofilms on this reactor after 24 h growth were observed via confocal laser scanning microscope (CLSM, eclipse 90i, Nikon, Japan) with 10X objective. The obtained 2D images were reconstructed into top-down images utilizing Imaris software (Bitplane, Switzerland) to show 3D structure.



(a)



(b)

**Figure 3.4.** (a) The schematic of experimental setup for incubate biofilms [30]. (b) The representative images of the biofilms at  $(1.3 \times 1.3\text{mm})$  from Confocal microscope and  $(80 \mu\text{m} \times 80 \mu\text{m})$  observing view from up-light microscope.



### 3.3. Depleting attractive colloidal gels

#### 3.3.1. Preparation of colloidal gels

Colloidal gels are made of poly(methyl methacrylate) (PMMA) spheres (diameter  $2a = 900 \text{ nm} \pm 6\%$ ) sterically stabilized with diphenyl-dimethyl siloxane [86, 87]. Fluorescent Nile Red is incorporated into the dispersion polymerization for visualization in confocal microscopy [86]. We select a refractive-index and density matched solvent (55/10/35 vol% cyclohexyl bromide/decalin/dioctyl phthalate) to eliminate dispersion interactions and to avoid sedimentation of the colloids. We add non-adsorbing polystyrene (molecular weight = 900,000 g/mol, radius of gyration  $R_g = 41 \text{ nm}$ , overlap concentration  $c^* = 0.0053 \text{ g/ml}$ ) at a dilute concentration ( $c/c^* = 0.375$ ) to a suspension of PMMA particles, creating gels with volume fraction  $\phi = 0.15$  and short attractive range ( $\zeta = R_g/a = 0.09$ ). Tetrabutylammonium chloride is added at a concentration of  $1 \text{ } \mu\text{M}$  to provide charge screening (Debye length  $\sim 0.16a$ ). To induce the colloids to do gelation, two kinds of conditions should be satisfied. The one is strong and short-range attraction force, for example by the steric stabilization, or van der Waals force, or depletion attraction. The other is the modest electrostatic repulsions that is compatible with gelation. In our study, we tested the gelation of colloids by controlling concentration of depletion polymer, the size of particles, and the surface

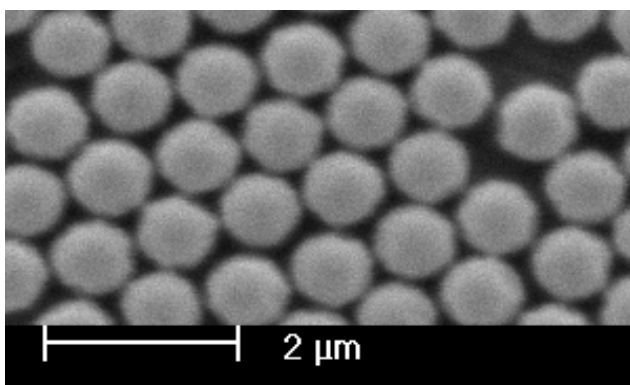


**Figure 3.5.** The synthesized PMMA particle obtained by SEM.

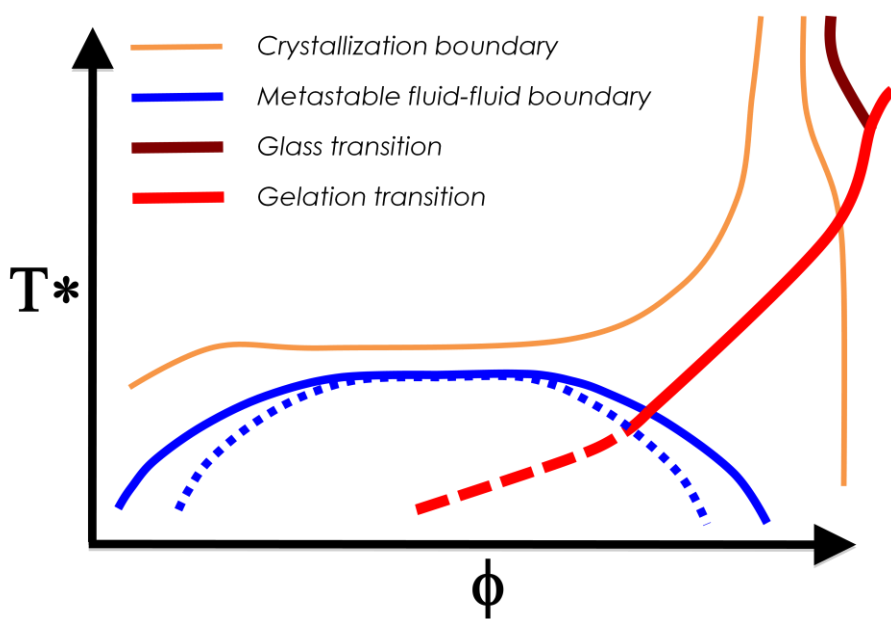
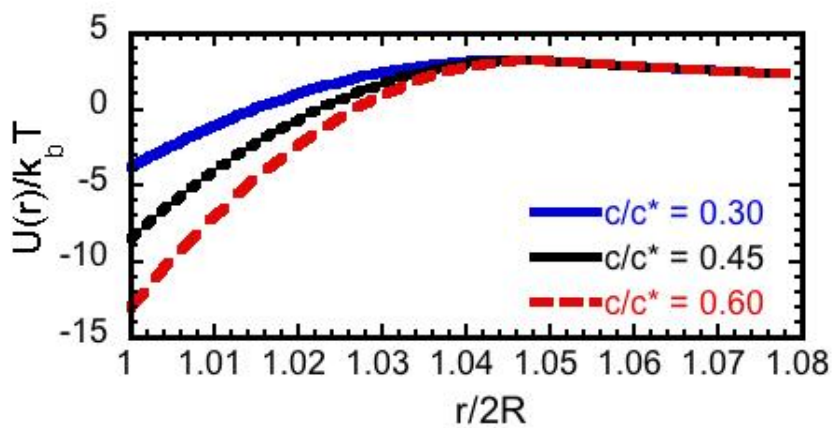
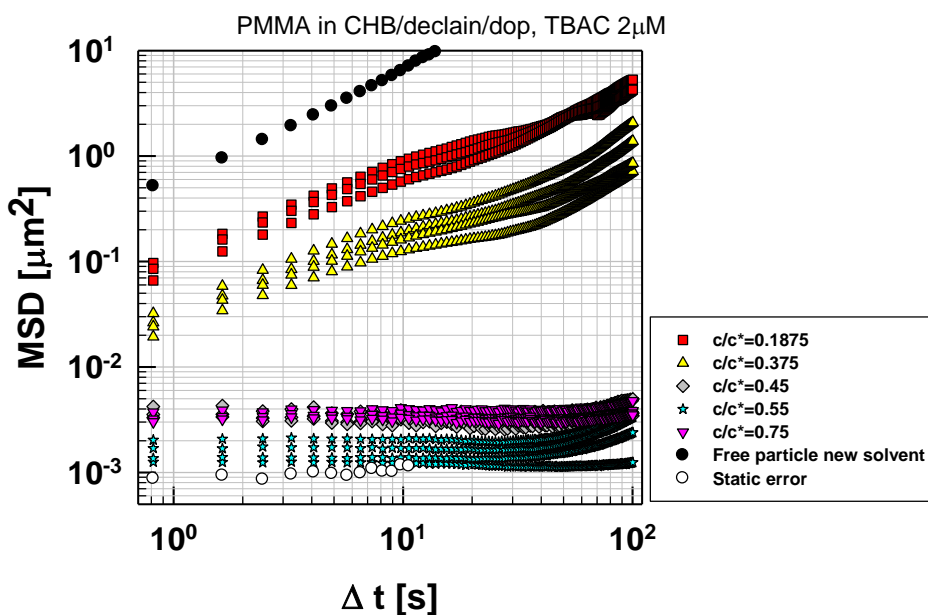


**Figure 3.6.** Gelation, phase separation and interaction potentials [64, 88]



(a)



(b)

**Figure 3.7.** (a) The general curves of overall force for our system calculating using the Asakura and Oosawa equation with different depleting polymer concentration. (b) The MSD curves of colloidal gels with increased  $c/c^*$ .

charge of colloids, and ionic concentration. Using the classical Asakura-Oosawa approximation for depletion attraction and the Yukawa potential for electrostatic repulsion [89, 90]:

$$U_{att}(r) = -\prod_{polymer} V_{overlap} \quad (3.3)$$

$$U_{charge}(r) = \frac{k_b T Z^2 \lambda_B \exp(-\kappa(r - 2R))}{(1 + \kappa R)^2 r} \quad (3.4)$$

,where  $k_B$  is the Boltzmann constant and  $T$  is the temperature ( $T = 298\text{K}$ ). The general curves of overall force for our system by calculating using the Asakura and Oosawa equation are shown in Figure 3.7. We estimate the net inter-particle potential,  $U$ , to be on the order of  $-4k_B T$ . Finally, based on the potential energy curve, we find that our system have a chance to make the gel structure. This type of weak depletion gels are widely studied [Gao's gels are  $3 k_B T$ , Clare's gels are  $U_0=17 k_B T$ , Lu's gels are  $<1 k_B T$ ]. We show representative confocal images of gels as a junction of waiting time in Figure 3.8(a), along with dynamical measures of the gelation process in Figure 3.8(b) and (c).

### 3.3.2. Static and dynamic error

Savin and Doyle have suggested the static and dynamic error in particle tracking microrheology [82]. In our experimental setup, we established the

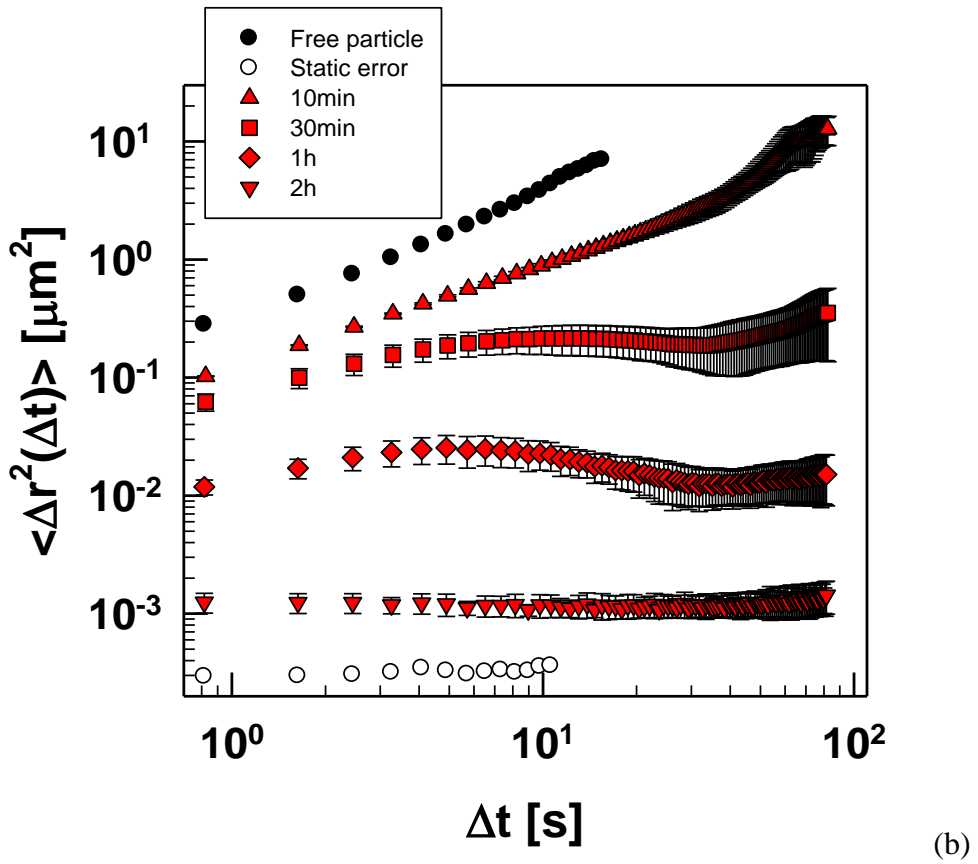
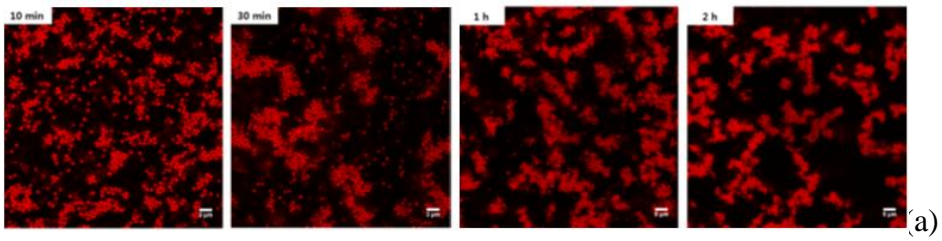
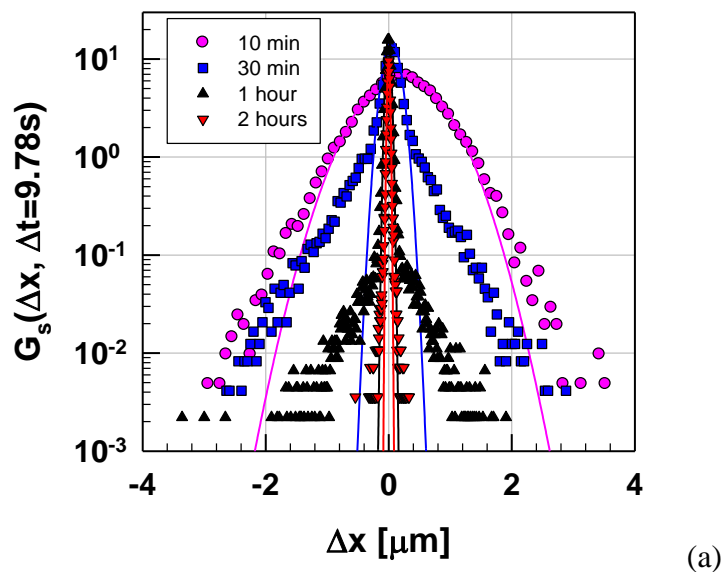
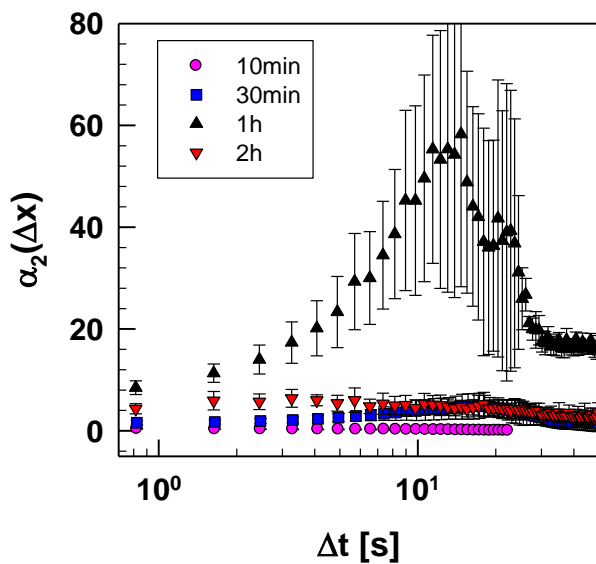


**Figure 3.8.** (a) The 2D images (b) The MSD of quiescent colloidal gels as increasing waiting time to create gel structure at  $c/c^*=0.375$ .



(a)



(b)

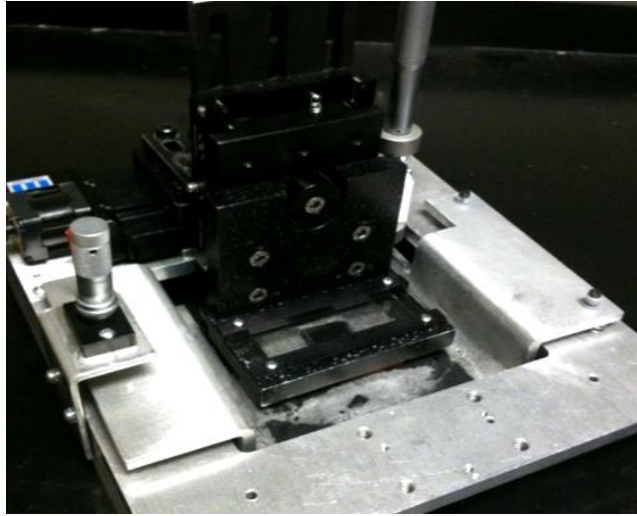
**Figure 3.9.** (a) van Hove correlation function (b) non-Gaussian parameter of quiescent colloidal gels as increasing waiting time to create gel structure at  $c/c^*=0.375$ .

static error, which sets the lower bound on the measurable localization lengths, as following protocol of Savin and Doyle [82]. The probe particles are dispersed in the uncured Sylgard 184 Silicone elastomer base and, added the curing agent with mass ratio 10:1. Then, it's cured at 80 °C oven, making the particles immobilized in the gel. The measured static error is at  $\langle r_{\min}^2(\Delta t) \rangle = 3.20 \times 10^{-4} \mu\text{m}^2$  as shown with dot line in Figure 3.8(b). The dynamic error is happened when the shutter speed of camera is not high enough to capture the vigorous motion of particles, especially [82]. We confirmed that measurable variables are enough to observe the dynamics of colloidal suspensions as shown in Figure 3.10(b).

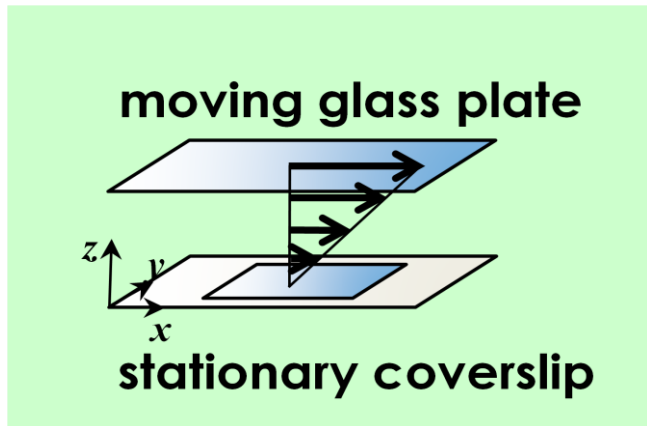
### 3.3.3. Experimental setup and procedures

Quiescent gels are loaded onto a custom-built shearing device that is mounted directly onto a confocal laser-scanning microscope with a 100x, 1.4 numerical aperture oil immersion objective as shown in Figure 3.9 [91]. The gels are allowed to rest for 2 hours in the shear cell, and a range of step strains  $\gamma = 0.1 - 80$  is induced at a shear rate of  $40 \text{ s}^{-1}$ . The high shear rate is chosen to avoid complications from shear banding. We verify the non-existence of shear banding by performing a steady state test on a conventional rheometer as shown in Figure 3.10. Because of visible back-





(a)



(b)

**Figure 3.10.** (a) The custom-built shearing device to apply the shear stress to the colloidal gels. (b) the scheme of the experimental setup.

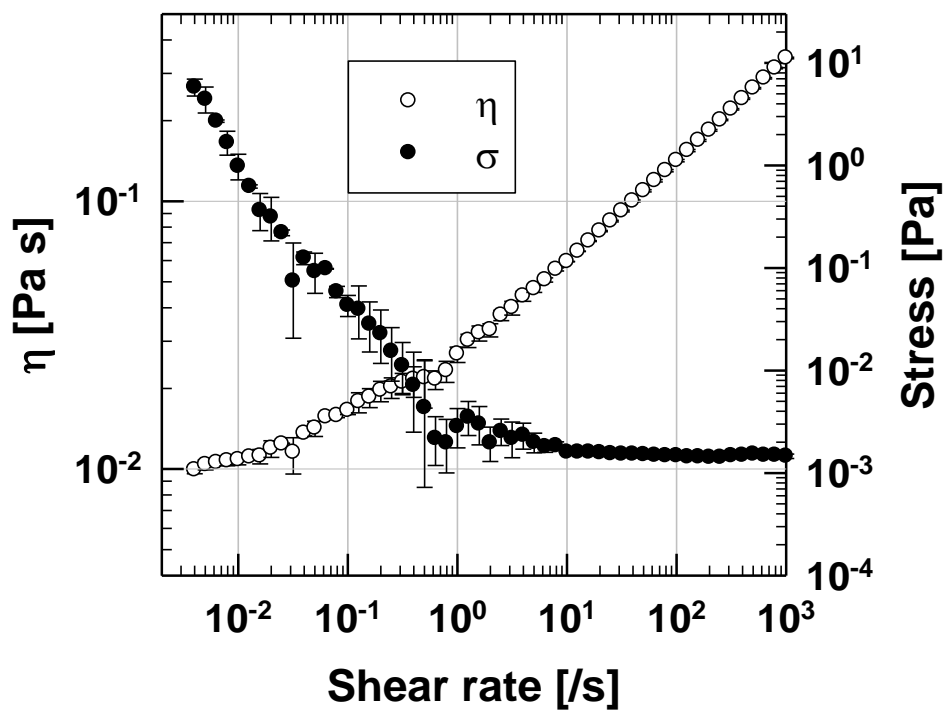


**Figure 3.11.** Rate sweep test using rotational type conventional rheometer (AR-G2) of quiescent colloidal gels.

flow immediately after the cessation of the step strain, we wait an additional 5 minutes prior to image acquisition in case of strain was higher than 30.0 as the backflow was significant at the high strain region. We capture the 2D dynamics of the sheared gels after this waiting time, over a total time period of 130 s with a lag time,  $\Delta t$ , of 0.652 s. A minimum of three experiments are performed for numerical aperture oil immersion objective [91]. The gels are allowed to rest before strain magnitude tested and their results are averaged. Particle tracking is performed with same process as described on the Section 3.1.2. We obtain the mean square displacement (MSD) of gels sheared at each  $\gamma$  as a function of time  $t$ . Then, we correct for sample drift by assuming that the drift velocity is independent of lag time. We obtain the average one-dimensional localization lengths of gels at each  $\gamma$ ,  $\langle r^2(\Delta t) \rangle = (\langle x^2(\Delta t) \rangle + \langle y^2(\Delta t) \rangle)/2$ , where  $x$  and  $y$  are the vorticity and velocity directions of the applied flow respectively [11].

### **3.3.4. Correction of drift velocity**

The basic principle of particle tracking microrheology has been on capturing only Brownian motion of probe particles on the closed system. However, we want to particle tracking microrheology on the open system by characterizing the dynamics of post-yielding colloidal gels right after

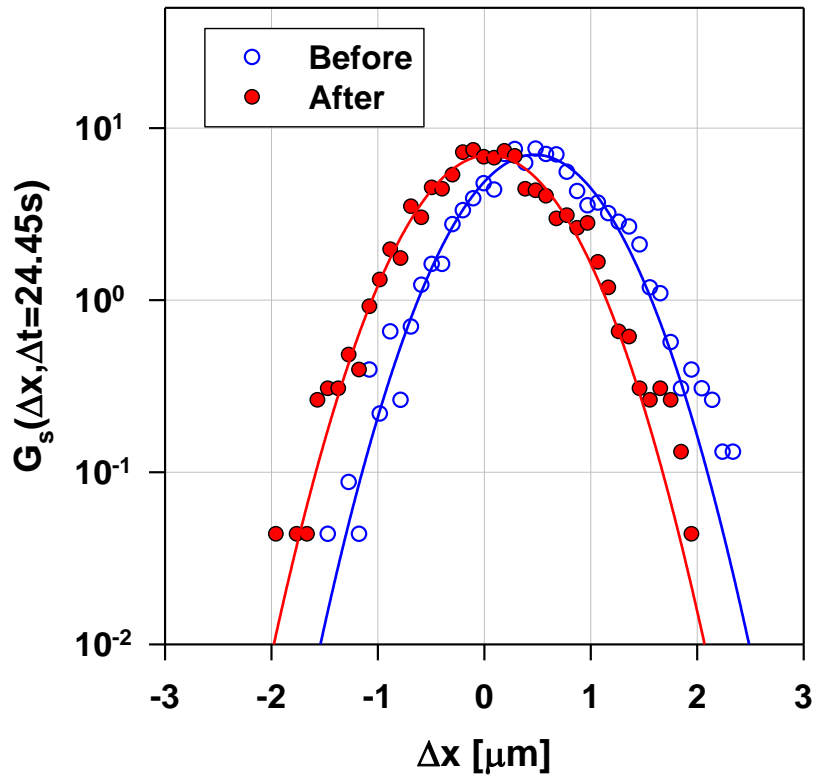


**Figure 3.12.** van Hove correlation function of pre-(open symbol) and post-(closed symbol) correction of drift velocity.

applying strain. Here, the significant back flow has been observed after yielding of colloidal gels. To get the meaningful data, we wrote a code to correct the drift velocity. The basic assumption is that the drift velocity should be linear on the lag time during measurement. Then, the position of particles is corrected on the opposite direction by calculating the mean velocity as shown in Figure 3.10(a).

To verify this code working well, we have a experiment of free PMMA particle suspension dispersed in Dioctyl phthalate(dop) as shown in Figure 3.10(b). The slope of MSD curve is corrected from 1.43 to 0.99 as following the results of Newtonian fluid. When the zero shear viscosity shows 72 cP calculated from MSD curve using Stokes in Figure 3.10(b), the value is corresponding with the one from conventional rheometry 76 cP.

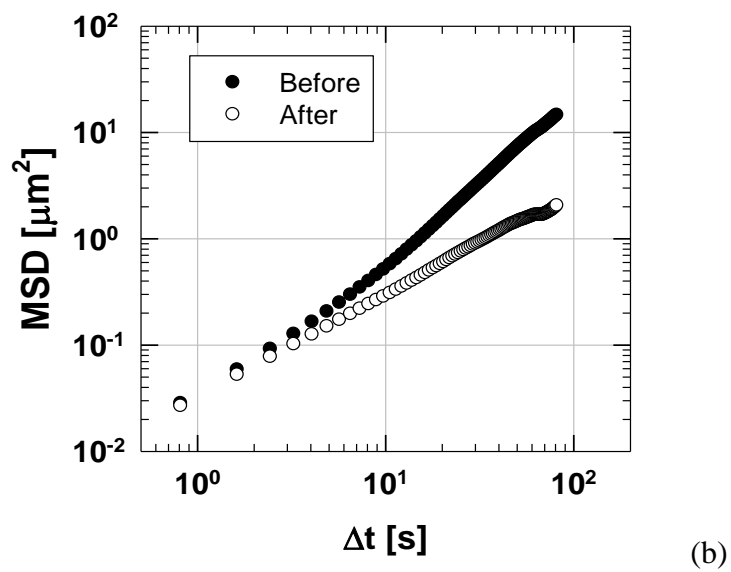
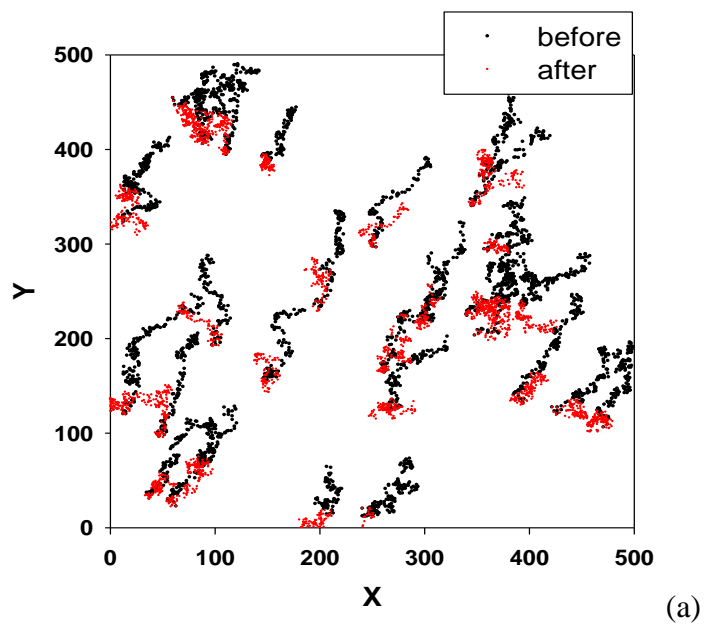


**Figure 3.13.** Verification of correction code. (a) trajectories of probe particles before and after applying correcting code (b) the MSD curves of before and after correction.

## **4. Verification of the particle tracking microrheology**

### **4.1. The slope of MSD curve**

Unlike bulk rheometry, high pre-shear is applied to the test fluid during sample preparation in microrheology measurements via ultra-sonication to evenly disperse the probe particles in the test medium. To evaluate any possible degradation of polymer chain and corresponding change in rheometry results, ultra-sonicated and none-sonicated polymer solutions were compared using bulk rheometry. Zero shear viscosity showed  $15\pm 5\%$  decrease from sonication and it was determined to be not ignorable. Therefore the same sonicated samples were used to both particle tracking microrheology and bulk rheometry.

Figure 4.1. shows the MSD curve of PEO (MW 2M) solutions. The slope at short times is less than one, and at long times it becomes close to one. The slope change is clearer for high concentration polymer solutions, due to physical network formation of polymer chains [92]. At short times, the elastic behavior of entangled polymer network is dominant. However, at long

### MSD plotting of M.W 2M PEO solution

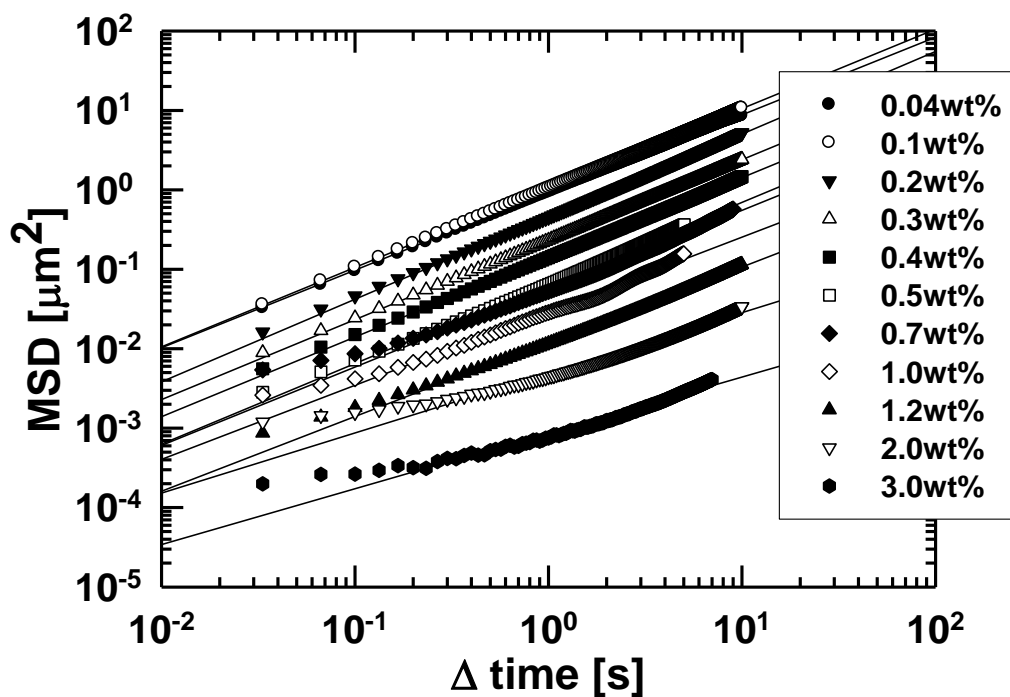


**Figure 4.1.** Mean square displacement of PEO (MW 2M) aqueous solutions with varied concentration (0.04 – 3.0 wt%).



times, the diffusion of polymer chain becomes dominant due to relaxation of the polymer chains through reptation, freeing the entanglement of chains. The slope of MSD curve changes to one as time marches, and the viscous character of the material become dominant. The point where the slope changes in MSD curve corresponds to the relaxation time either defined by Rouse model [80] or reptation model [92]. For 2.0wt% PEO (MW 2M) solution, the order of change point is 1.0 s which accords 2.0wt% PEO (MW 2M) solution, the order of change point is 1.0 s which accords with the relaxation time obtained using bulk rheometry, 1.0 s/rad. However, we cannot capture the point for lower concentration because the change occurs in the range smaller than the limiting detection time 0.033 s of our apparatus, and for higher concentration because the particle cannot diffuse over a distance that exceeds the detection resolution of our visualizing apparatus. The slope change for more PEO solutions with the same MW and varied concentration is shown in Figure 4.2. In case of other polymer solutions, PEO (MW 600k) and PAA (MW 1-2M) aqueous solution, the same trend is observed. The slope of MSD curve at short times decreases as elasticity of the materials increases, and the slope changes when the material transits from sub-diffusive to diffusive region

To measure the elasticity of the material, slope at short times should be

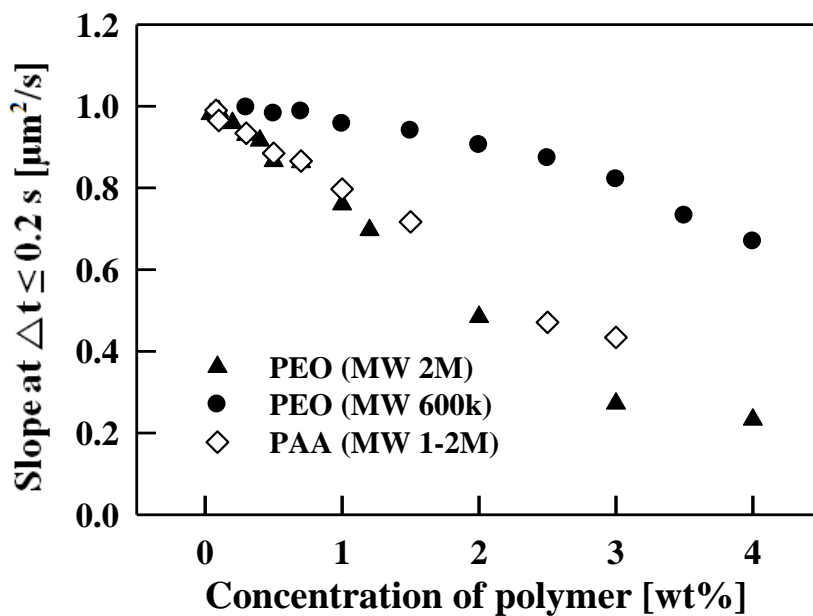


**Figure 4.2.** The slope of MSD curve as a function of polymer concentration for MW 2M PEO ( $\blacktriangle$ ), MW 600k PEO ( $\bullet$ ) and MW 1-2M PAA ( $\diamond$ ). The slope is from sub-diffusion region,  $\Delta t \leq 0.2$  s.

examined. Figure 4.3 shows the relation between the slope at short times and the elasticity as presented by  $G'$  from bulk rheometry at  $\omega = 10$  rad/s. The slope shown in this figure was obtained  $\Delta t$  less than 0.2 s, since the slope for all concentrations was changed after that point. Also, the frequency 10 rad/s was chosen such that both particle tracking microrheology and bulk rheometry can be apply to all polymer solutions studied in this work. The frequency range in particle tracking microrheology measurements was from 0.1 to 30.0 rad/s for all polymer solutions and from 4.0 to 70.0 rad/s in bulk rheometry for the lowest wt% polymer solution. The curve in Figure 4.3. followed the relation:

$$(G' \text{ at } \omega = 10 \text{ rad / s}) = \frac{8}{5 \times (\text{the slope of MSD curve})} - 2, \quad (4.1)$$

and the results were valid for all polymer solutions followed. Using this relation, the degree of elasticity could be estimated from the slope of MSD curve. It can be useful when calculating dynamic moduli is difficult in particle tracking rheology measurements due to the fluctuation in MSD curve, as is often the case in examining the local dynamics of biological materials [1, 8, 9].

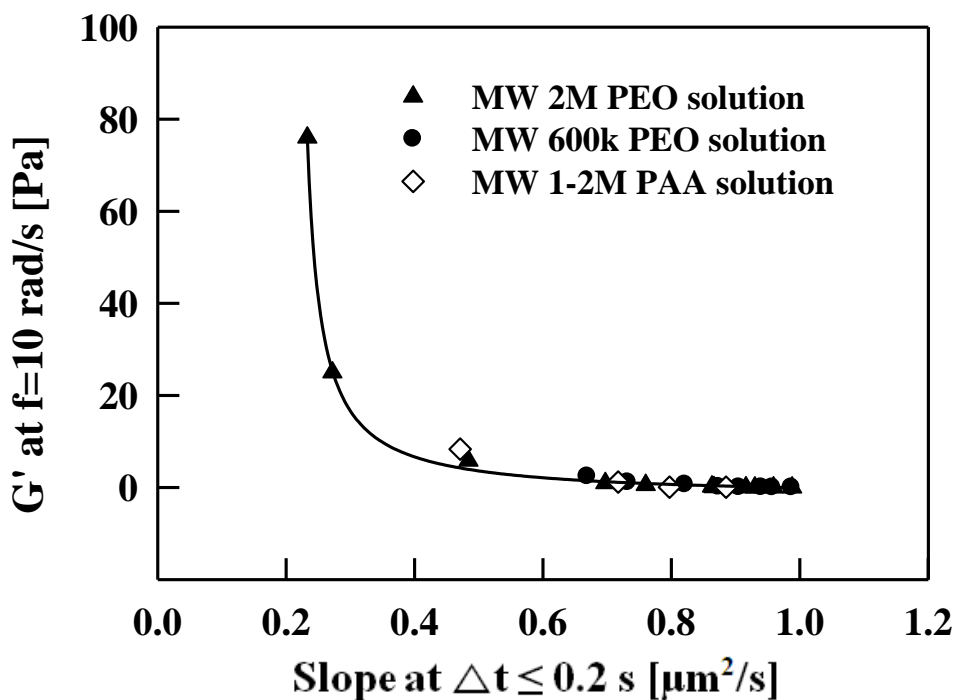


**Figure 4.3.** The relation between the slope of MSD curve at short times from microrheology measurements and  $G'$  at 10 rad/s from bulk rheometry as a representative degree of elasticity.

## 4.2. Dynamic moduli

Maxwell model and Euler's equation were applied to equation (2.19) and (2.20) to result in dynamic modulus and the results are compared with those from bulk rheometry as shown in Figure 4.4.  $G''$  from Euler's equation as well as that from Maxwell model well matches to the one from bulk rheometry for both 0.4 wt% and 1.0 wt% PEO (MW 2M) solutions in Figure 4.4(a) and (b). However,  $G'$  from Euler's equation is unstable at low frequencies and does not match well to the one from bulk rheometry unlike Maxwell model. This is pronounced only in  $G'$  since it is dilute polymer solution and its viscosity is dominant over elasticity. The number of data is reduced at long measurement times and the data are directly substituted to Euler's equation whilst it is smoothed out in the fitting process in using Maxwell model. Euler's equation uses the slope just from neighboring two points, and  $\langle r^2(1/\omega) \rangle$  in equation (2.21) at short times is unstable to be used in calculating  $|G^*(\omega)|$  [3]. At short times, although the number of data points is enough, the distribution due to Brownian motion can be broad. With these results, we conclude that the Maxwell model is more reasonable to use in calculating dynamic moduli in case of low concentration of polymer solution.  $G_j$  and  $\tau_j$  from fitting to Maxwell model are shown in Table 4.1.

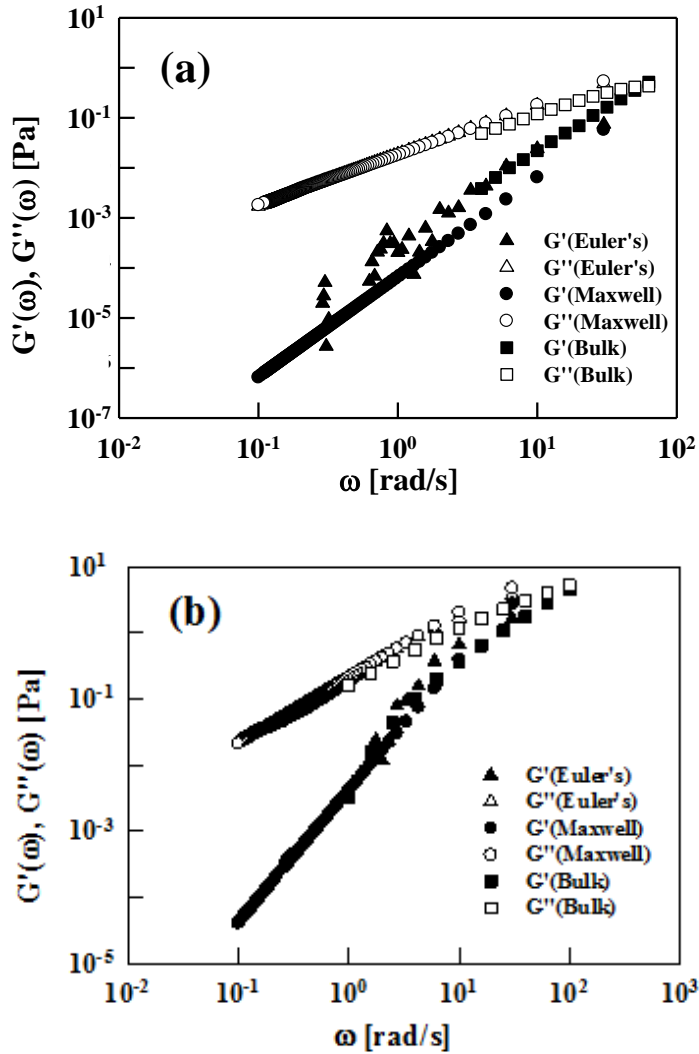


**Figure 4.4.** Dynamic moduli of PEO (MW 2M) solution from particle tracking microrheology using Euler's equation ( $\triangle$ ,  $\blacktriangle$ ), Maxwell model ( $\circ$ ,  $\bullet$ ) and from conventional rheometry ( $\square$ ,  $\blacksquare$ ). Closed symbols are storage modulus, and open symbols are loss modulus. (a) 0.4wt%, (b) 1.0wt%.

**Table 4.1.** Modulus coefficient ( $G_j$ ) and relaxation time coefficient ( $\tau_j$ ) obtained from Maxwell model for PEO solution (MW 2M). Two modes were used for 2.0wt% solution.

Concentration of PEO (MW 2M)	$G_j$ [Pa]	$\tau_j$ [s]
0.1 wt%	0.4	0.0033
0.4 wt%	2.5	0.003
1.0 wt%	3.63	0.019
2.0 wt%	1.56	0.250
	4.06	0.256

For low concentration PEO solutions, single-mode Maxwell mode was used, and two-mode Maxwell model was used for better fitting for 2.0 wt% PEO solution. In Figure 4.5 to Figure 4.7, the dynamic moduli obtained from particle tracking microrheology using Maxwell model are compared with those from bulk rheometry for varied concentration of PEO and PAA solutions. Not only these results matched well for certain range of polymer concentration, but also very weakly elastic materials whose viscosity is close to that of water could be captured using particle tracking microrheology. However, when the concentration of PEO (MW 2M) becomes as high as 2.0 wt%, the slope of  $G'$  starts to deviate from the one from bulk rheometry as in Figure 4.5. Bredveld and Pine (2003) suggested equation:

$$\eta_{\max} = \frac{2k_B T}{3\pi a \delta^2} \Delta t, G_{\max} = \frac{2k_B T}{3\pi a \delta^2} \quad (4.2)$$

,for upper limit modulus  $G_{\max}$  in applying the microrheological measurement. The zero shear viscosity of 2.0 wt% PEO solution, 2.1 Pa·s, is close to  $\eta_{\max}$ , 1.8 Pa·s as calculated from equation (4.2), and  $G'$  is 18 Pa from bulk rheometer at  $\omega=70$  rad/s, and  $G_{\infty}$  is close to the upper limit storage modulus 54 Pa as calculated by equa. For other polymer solutions, the dynamic modulus of PAA (MW 1-2M) solution starts to deviate from at 2.5 wt% where  $G'$  is 26 Pa at  $\omega=100$  rad/s as shown in Figure 4.7.



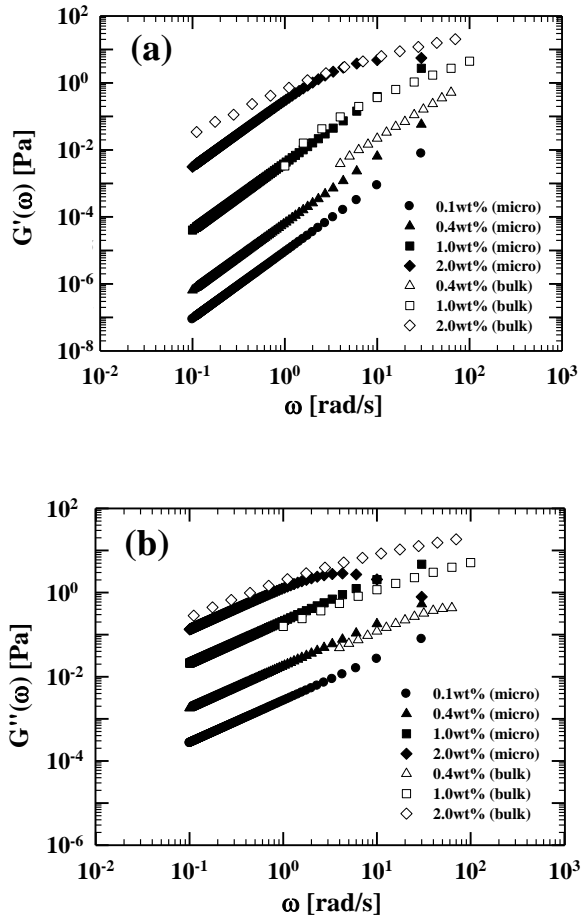


**Figure 4.5.** Comparison of dynamic moduli of PEO (MW 2M) aqueous solution obtained from particle tracking microrheology with those from bulk rheometry: (a)  $G'$  (b)  $G''$  at concentration of 0.1 wt% ( $\bullet$ ), 0.4 wt% ( $\blacktriangle$ ,  $\triangle$ ), 1.0 wt% ( $\blacksquare$ ,  $\square$ ) and 2.0wt% solution ( $\blacklozenge$ ,  $\diamond$ ). Closed symbols are from particle tracking microrheology, and open symbols are from conventional rheometry.

Finally, we found that the concentration of polymer solution at which the modulus starts to deviate is the same as the one at which the viscosity starts to deviate. Therefore, the measurement from microrheological method can be verified by considering the upper limit viscosity.

We compared rheological properties of various polymer solutions as measured by particle tracking microrheology and conventional rheometry. First, zero shear viscosity was obtained using Stokes-Einstein equation at longer times of mean square displacement (MSD) curve in particle tracking microrheology, and compared to the one determined by rotational-type bulk rheometer. The zero shear viscosity from particle tracking microrheology matched well with the one from bulk rheometry. Second, dynamic modulus was determined using two models, Maxwell model and Euler's equation, since these have been most frequently adopted in previous studies. When Euler's equation was used, loss modulus matched well with the one from bulk rheometry for all frequency range. However, storage modulus was unstable at low frequencies, stemming from non-smoothing out in fitting process. When the Maxwell model was used, two results agreed well at low concentration of polymer solution, and the dynamic modulus at small frequency region which are difficult to detect in bulk rheometry could also be measured. However, both zero shear viscosity and dynamic modulus at

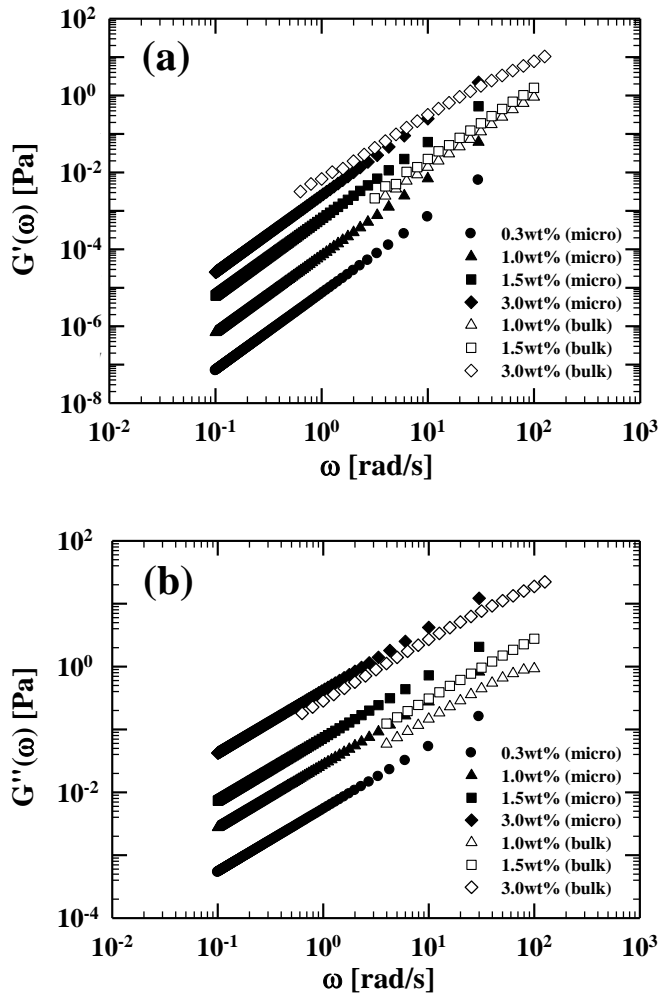


**Figure 4.6.** Comparison of dynamic moduli of PEO (MW 600k) solution from particle tracking microrheology with those from bulk rheometry: (a)  $G'$  (b)  $G''$  at concentration of 0.3 wt% (●, ◆), 1.0 wt% (▲, △), 1.5 wt% (■, □) and 3.0 wt% solution (◆, ◇). Closed symbol are from particle tracking microrheology, and open symbol are from conventional rheometry.

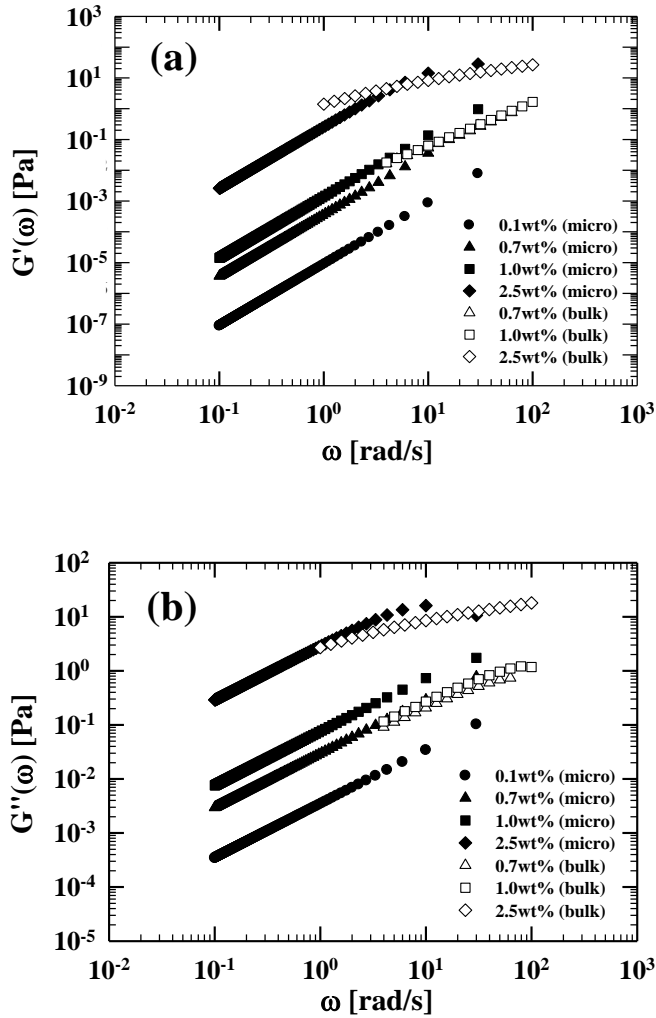


**Figure 4.7.** Comparison of dynamic moduli of PAA (MW 1-2M) solution from particle tracking microrheology with those from bulk rheometry: (a)  $G'$  (b)  $G''$  at concentration of 0.1 wt% (●), 0.7 wt% (▲, △), 1.0 wt% (■, □), and 5.0 wt% solution (◆, ◇). Closed symbols are from particle tracking microrheology, open symbols are from conventional rheometry.

higher concentration from particle tracking microrheology deviated from those from bulk rheometry, due to the error caused by limited resolution of the apparatus. Based on these results, we presented a guideline for the reliable performance of this new technique.

# 5. Controlling and removal of the bacterial community biofilms

## 5.1. The dynamics of bacteria on the anodic electrode

In this section, we have approached for controlling bacterial adhesion by the application of electric fields.

### 5.1.1. Effect of current density on bacterial displacement

Figure 5.1 shows the averaged MSD of bacteria for 10 s (a) and the averaged  $\sqrt{MSD}$  as a function of current density (b) at an ionic strength of 20 mM. Active bacterial motion was observed immediately the electric current was applied, as shown in Figure 5.1(a), like that previously reported by Hong et al [30]. Little bacterial motion was observed under non-polarized conditions. The cell voltage quickly reached about 2.4 V and was maintained thereafter. Figure 5.1(a) shows that the MSD curves had a power-law relation ( $MSD(\Delta t) = 2nD(\Delta t)^\beta$ ) as a function of lag time ( $\Delta t$ ), where  $D$  [ $m^2/s$ ] is the diffusion coefficient for translational motion and  $n$  is the dimensional factor, which was 2 for 2 coordinate motion [49]. The slopes of the MSD curve at

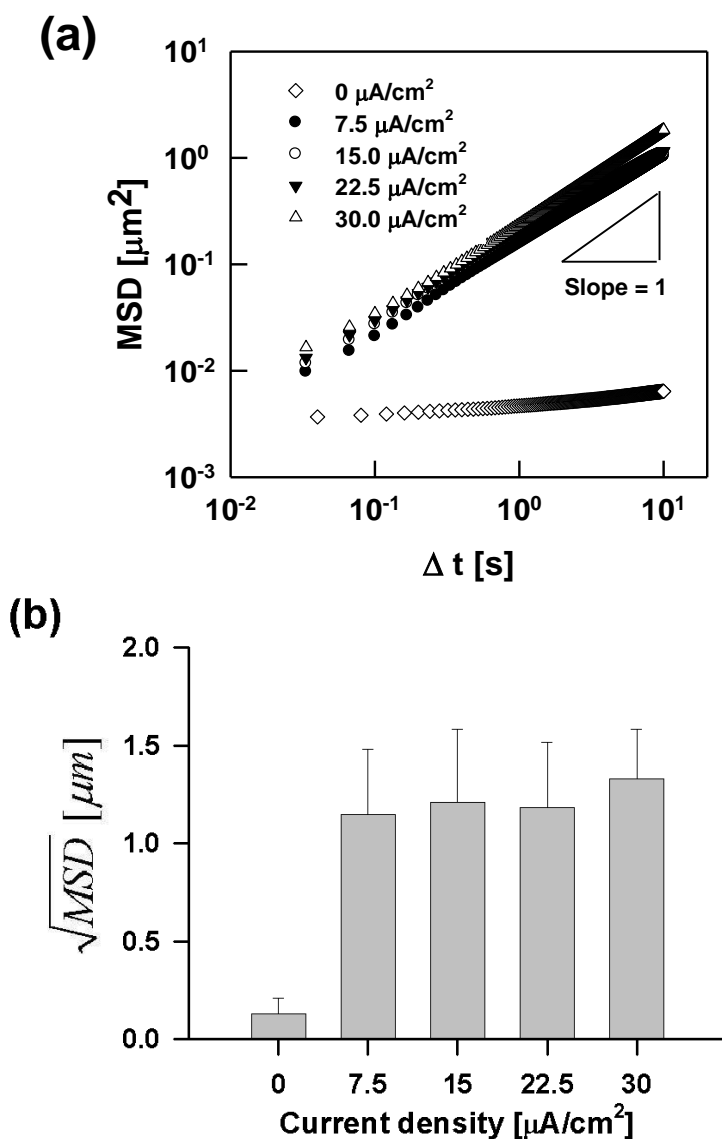


**Figure 5.1.** (a) Averaged mean square displacement (MSD) of bacterial cells on an anode surface depending on current densities at an ionic strength of 20 mM. (b) Averaged  $\sqrt{\text{MSD}}$  of bacterial cells moving on an anode surface or  $\Delta t = 10$  s as a function of current density.  $N = 3$ ; SD shown.

each current density were 0.12, 0.83, 0.75, 0.77, and 0.873 (from 0 to 30  $\mu\text{A}/\text{cm}^2$ ), that is, all were less than one. If the slope of the MSD curve is one, the motion of the cells is diffusive [49]. This means that the cells move freely in the Newtonian medium by Brownian motion, which results in a random walk. This study shows that the bacterial community in Figure 5.1(a) exhibited sub-diffusive motion ( $\beta < 1$ ) under anodic polarization. In contrast, Rogers et al. reported that most bacterial cells suspended in a medium showed super-diffusive motion ( $1 < \beta < 2$ ) in the absence of an electric field [46]. It is important to note the difference in terms of experimental design between these two studies to understand the reasons for the differences of slope. In this study, the motion of bacterial cells that had previously adhered to the surface was measured in the presence of an anodic electric field. In contrast, Rogers et al. measured the motion of bacterial cells in a suspended state in an aqueous solution in the absence of an anodic electric field [46]. An interpretation of the difference of slopes is that in this study, the surface adhesive force of bacterial cells and the electrostatic attractive force combined to slow down bacterial motion, thereby resulting in sub-diffusive motion of the bacterial community. To better compare the bacterial displacement shown in Figure 5.1(a), the MSDs at  $\Delta t = 10$  s were taken square roots. As shown in Figure 5.1(b), the  $\sqrt{MSD}$  s were similar (1.15-



1.32  $\mu\text{m}$ ), regardless of current density (7.5  $\mu\text{A}/\text{cm}^2$  to 30  $\mu\text{A}/\text{cm}^2$ ). However, the displacement was approximately 10 times larger than that with no current density. Note that the  $\sqrt{\text{MSD}}$  under no current density was very small (0.13  $\mu\text{m}$ ). Figure 5.1(b) shows that there is a critical current density between 0 and 7.5  $\mu\text{A}/\text{cm}^2$ , which was large enough to detach PAO1 cells from the surface. Beyond that critical point, any increase in current density did not affect the MSD of PAO1 cells.

Figure 5.2 shows the MSD curves of individual bacterial cells as a function of  $\Delta t$  under 2 conditions, that is, low current density of 7.5  $\mu\text{A}/\text{cm}^2$  (Figure 5.2(a)), and high current density of 30.0  $\mu\text{A}/\text{cm}^2$  (Figure 5.2(b)). The plots in Figure 5.2 indicate the motion of individual bacterial cells, with a total of 20 cells at each current density. The MSD curves of 20 bacterial cells were randomly selected from individual images containing 200 (50 bacterial cells during measurements, to show the distinguished curves. Figure 5.2(a) shows that at a current density of 7.5  $\mu\text{A}/\text{cm}^2$ , most tracks exhibited a sub-diffusive motion that followed a power law,  $\text{MSD}(t) = 2nDt^\beta$ , where  $0 < \beta < 1$ , thereby confirming the results shown in Figure 5.1(a). Some tracks of the 20 cells were observed to exhibit super-diffusive ( $1 < \beta < 2$ ) motion. In contrast, Figure 5.2(b) shows that super-diffusive motion was not observed at 30  $\mu\text{A}/\text{cm}^2$ . Non-diffusive motion [93] of several bacterial cells with a slope of

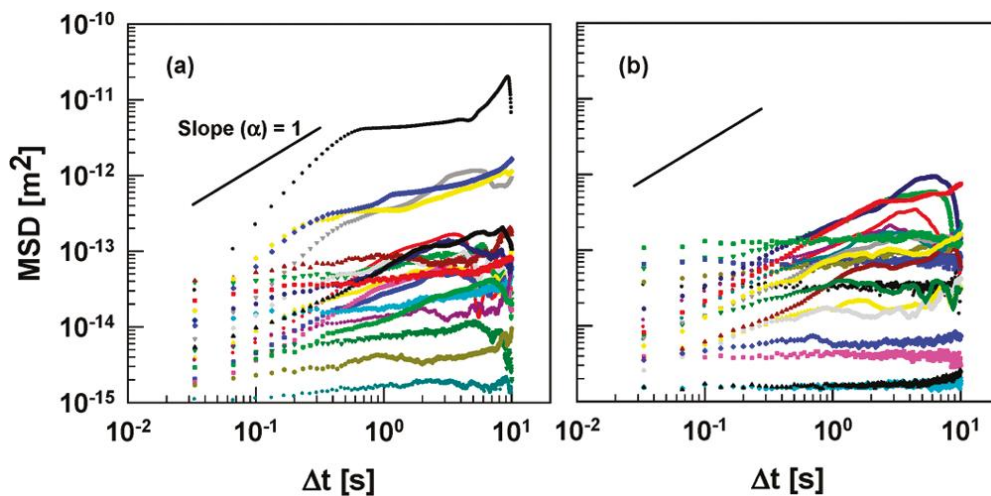


**Figure 5.2.** MSD curves of individual bacterial cells on the whole bacterial community on an anode surface at an ionic strength of 20 mM at current density of (a)  $7.5 \mu\text{A}/\text{cm}^2$  and (b)  $30 \mu\text{A}/\text{cm}^2$ . To show the curves distinguished, the MSD curves of 20 bacterial cells were selected randomly among 200 bacterial cells in each plot.

0 ( $\beta \approx 0$  in  $MSD(t) = 2nDt^\beta$ ) was observed. Thus, the characteristic of bacterial motion at a higher current density was a trend to becoming more sub-diffusive or even non-diffusive. This observation was consistent with the hypothesis that bacterial cells could not overcome the stronger electrostatic attractive force that arose at a higher current density. Most bacterial cells showed sub-diffusive motion under anodic polarization, although some cells showed super-diffusive motion or non-diffusive motion under varying current densities.

Figure 5.3 shows the trajectories of bacterial motion for 50 s as a function of current density. The detailed trajectories of bacterial motion shown in Figure 5.3 indicate that the bacterial dynamics were quite different, although the  $\sqrt{MSD}$  s were similar regardless of the current density, as shown in Figure 5.1(b). Figures 5.3(a) and (b) show 2 types of dynamic motion of PAO1 cells, with random oscillating motion at the adhered position and circular motion over a long length scale, which might be the natural motion of PAO1 cells in the medium. The circular motion of rod-shape cells such as *C. crescentus* [94] or *E. coli* [95] was previously observed under non-polarized conditions. These types of circular motion might correspond with the super-diffusive motion shown in Figure 5.2(a). Rogers et al. interpreted that the super-diffusive motion was caused by a particular motion of bacterial

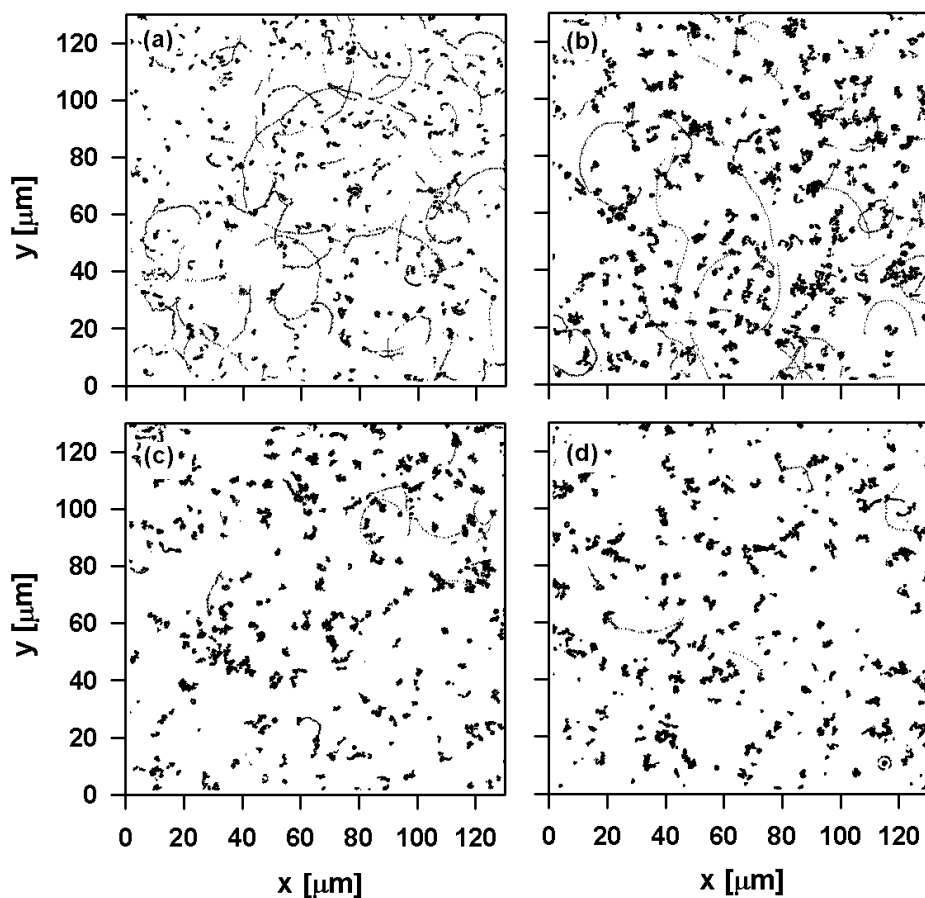


**Figure 5.3.** Trajectories of bacterial cells moving on an anodic surface at ionic strength of 20 mM at various current densities captured for 50 s at a frame rate of 30 Hz. The x and y axes are the directional coordinates, and each point is the centroid of an individual bacterium. The number of bacteria is  $200 \pm 50$ /picture. (a) Current density =  $7.5 \mu\text{A}/\text{cm}^2$ , (b)  $15 \mu\text{A}/\text{cm}^2$ , (c)  $22.5 \mu\text{A}/\text{cm}^2$ , and (d)  $30 \mu\text{A}/\text{cm}^2$ .

cells, such as swimming [46]. The percentage of oscillating cells was approximately 90-95% while the rest exhibited circular motion. As current density increased, the number of the bacterial cells with circular trajectories decreased. At a current density of  $30 \mu\text{A}/\text{cm}^2$ , the majority of bacterial cells were oscillating, which resulted in sub-diffusive motion. In addition, the radii of the trajectory of each oscillating cell at current densities between  $15$ - $30 \mu\text{A}/\text{cm}^2$  was increased when compared with those at  $7.5 \mu\text{A}/\text{cm}^2$ .

The dynamics of bacterial motion under an electric field, as shown in Figure 5.3, might be explained by two mechanisms [96], electro-hydrodynamic flow and electro-osmotic flow, both of which were previously used to characterize the motion of polymer particles under an electric field. Electro-hydrodynamic flow is caused by the migration of ions, such as  $\text{H}_3\text{O}^+$  and  $\text{OH}^-$ , thereby generating convective flow [97]. Active electrolysis is required for significant electro-hydrodynamic flow. Water electrolysis was examined in this study's experimental system by measuring LSV, and the oxygen evolution potential was found to be  $2.1 \text{ V}$  as shown in Figure 3.3. The anode potential at  $15 \mu\text{A}/\text{cm}^2$  with a batch-type electrochemical cell reached almost  $2.1 \text{ V}$  (vs  $\text{Ag}/\text{AgCl}/\text{KCl sat'd}$ ) of oxygen evolution potential. The anode potential is closely related to oxygen evolution potential, so electro-hydrodynamic flow appeared to be present under this study's

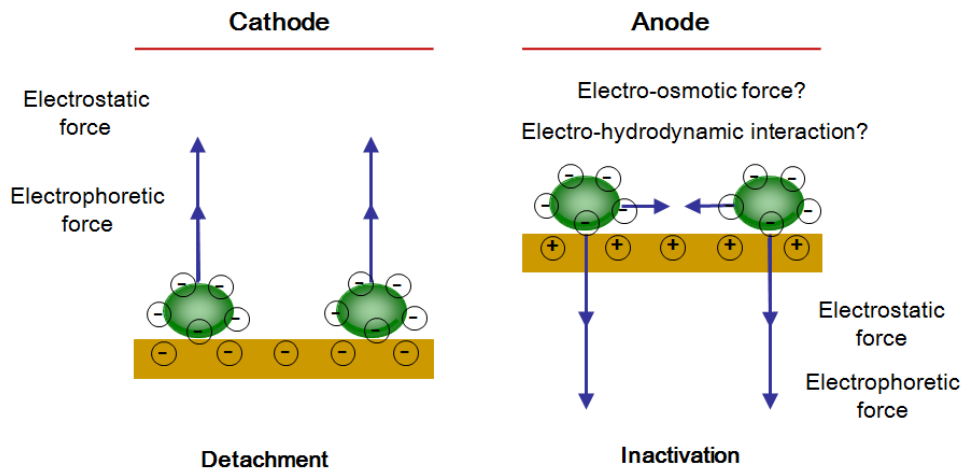


**Figure 5.4.** Movement of bacterial cells under cathodic and anodic electrodes, and the detachment mechanism suggested by Poortinga et al. [31]

experimental condition. However, active generation of gas bubbles was not visibly observed on the electrode surface during the experiment. If electro-hydrodynamic force is a major contributing factor the bacterial motion should also not be localized to the anodically polarized electrode system. Therefore, the electro-hydrodynamic flow may provide only a limited explanation for the bacterial motion. As the current density increased, the electro-hydrodynamic flow may increase as more ions are consumed at the electrodes, so a higher pressure gradient would be generated. The range of current densities that resulted in lateral migration on the electrodes caused by electro-hydrodynamic flow [97, 98] was similar to that reported in the literature. In addition, the electro-osmotic force [30, 31] was asserted to affect bacterial motion. The electro-osmotic force is the motion of a liquid induced by an applied potential across a capillary tube or microchannel [99]. However, an explanation for bacterial motion caused by an electro-osmotic force [30, 31] cannot be considered in this study, because the experimental conditions were different to those in the literature. The induction of electro-osmotic flow requires that the direction of the electric field must follow the surface of the flow channel [99], while the flow must be parallel to the wall. However, the direction of the electric field was perpendicular to the wall in the current study. Therefore, neither electro-hydrodynamic flow nor electro-

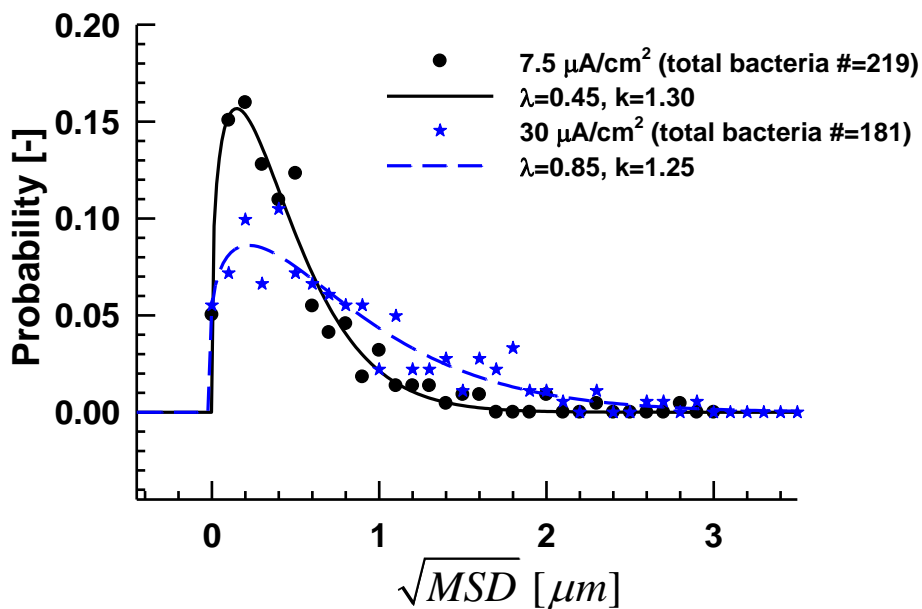


**Figure 5.5.** The distributions of  $\sqrt{MSD}$  of bacterial cells moving on an anode surface for 10 s at current densities of  $7.5 \mu\text{A}/\text{cm}^2$  (●) and  $30 \mu\text{A}/\text{cm}^2$  (★) at an ionic strength of 20 mM. The lines are fitted distributions with the Weibull distribution function (equation (3.1)) expressed using scale parameter ( $\lambda$ ) and shape parameter ( $k$ ).



osmotic flow alone was sufficient to explain the motion of the bacterial community under anodic polarization. Further studies will be necessary to understand the mechanism.

Figure 5.5 shows normalized distributions of  $\sqrt{MSD}$  of bacterial cells moving on an anode surface at two current densities ( $7.5 \mu\text{A}/\text{cm}^2$  &  $30 \mu\text{A}/\text{cm}^2$ ) for 10 s. At  $7.5 \mu\text{A}/\text{cm}^2$ , the majority of PAO1s moved a little displacement with  $0.2 \mu\text{m}$ , except for a small fraction of circularly moving bacteria showing long displacement as shown in Figure 5.3(a). As the current density increased to  $30 \mu\text{A}/\text{cm}^2$ , the distribution of bacterial displacement shifted to the right, and at the same time, the probability of peak displacement was decreased by half, indicating that the number of bacteria moving longer distance increased. The distributions were fitted with the Weibull distribution function (equation 3.1). When the current density increased to  $30 \mu\text{A}/\text{cm}^2$ , the shape parameter ( $k$ ) changed little, keeping the shape of the peak similar. The scale parameter ( $\lambda$ ) at  $30 \mu\text{A}/\text{cm}^2$  was larger than that at  $7.5 \mu\text{A}/\text{cm}^2$  showing broader distribution.

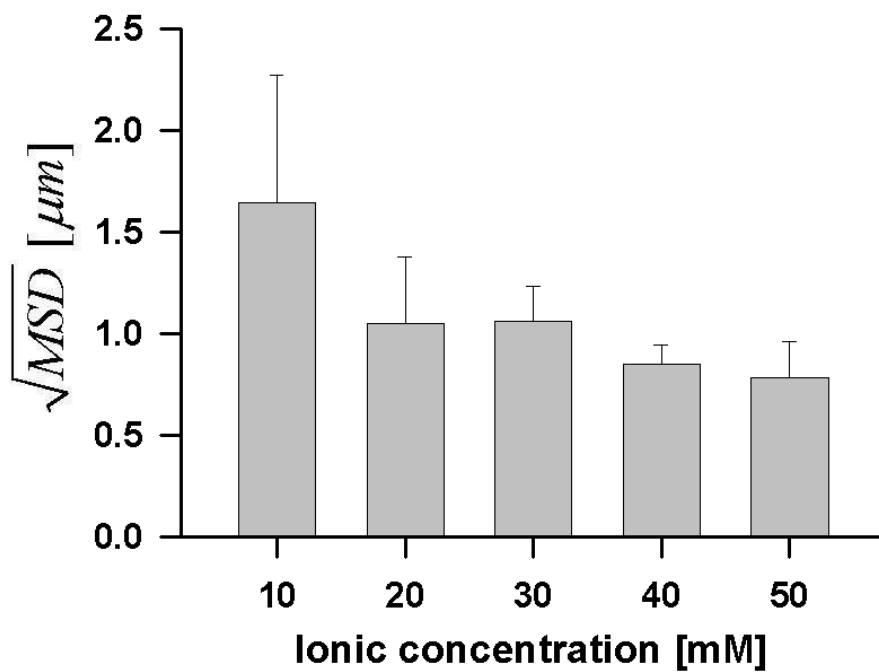


**Figure 5.6.** The  $\sqrt{MSD}$  of bacterial cells moving on an anodic surface for 10 s depending on ionic strength 10 - 50 mM at a current density of  $15 \mu\text{A}/\text{cm}^2$ . These data were calculated from equation (2.15), and averaged for every set of data.

### 5.1.2. Effect of ionic strength on displacement of PAO1s

Figure 5.6 shows the  $\sqrt{MSD}$  of bacterial cells moving on an anode surface for 10 s depending on the ionic strength. The  $\sqrt{MSD}$  decreases with increasing ionic strength. One explanation is that the electrostatic interaction is affected by the ionic strength of the medium. The surface of PAO1 cells forms an electric double layer with ions, and the double layer thickness is reduced as the ionic strength increases [100, 101]. There are two types of forces acting between bacterial cells and the electrode surface, van der Waals and electrostatic interaction force [100]. The van der Waals force is not affected by ionic strength, whereas the electrostatic interaction is increased at a higher ionic strength, leading to more oscillating motion of PAO1s due to bacterial adhesion to the surface. Therefore, the root MSD of cells decreases at high ionic concentration.

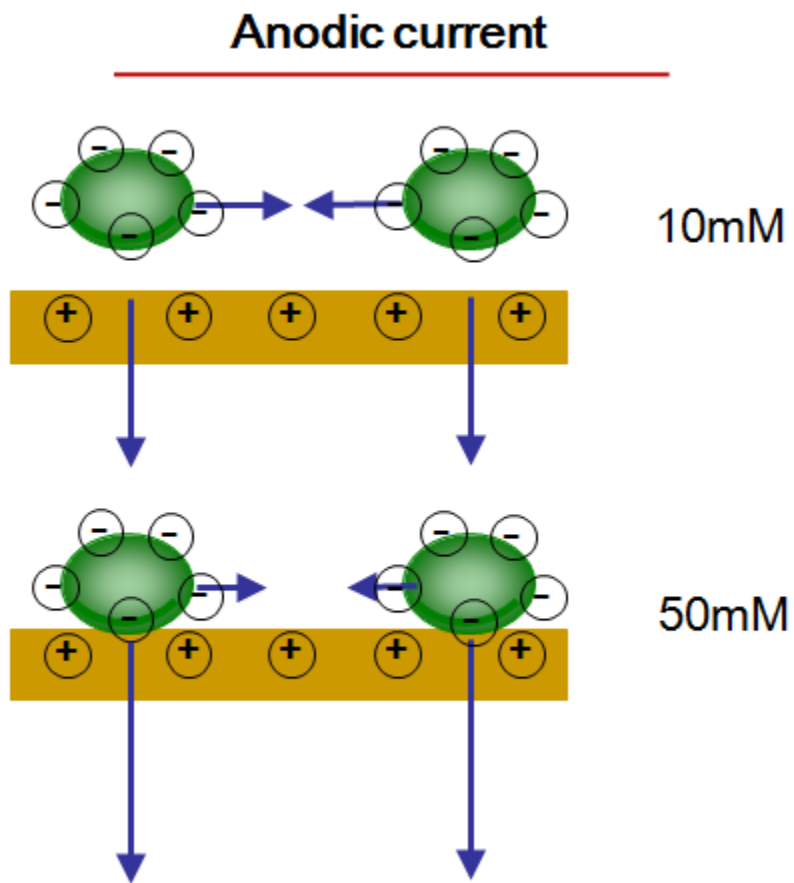


**Figure 5.7.** The schematic to show the effect of ionic strength on the anodic surface.

### 5.1.3. Applicability for biofilm control.

Figure 5.8 shows the effects of anodic polarization on the biofilm growth. Figure 5.8(a) shows a densely packed biofilm structure with an average thickness of 20  $\mu\text{m}$  formed under non-polarized conditions. In contrast, Figure 5.8(b) shows that the structure of biofilms grown under anodic polarization was thinner, with an average thickness of 10  $\mu\text{m}$  and it was looser in comparison with the non-polarized condition. The effect of the anodic electric field in preventing biofilm growth can be interpreted based on bacterial motions on the anodically polarized surface. As shown in Figure 5.3, bacteria could not stably adhere to anodically polarized surface. Therefore, bacterial cells floated slightly on the anodically polarized surface and were easily swept away by the flow of the medium, thereby resulting in reduced growth of the bacterial biofilm. As bacterial motion increases, the rate of biofilm formation would be expected to slow down accordingly.

Finally, we quantified the motion of bacteria under an anodic electric field using a tracking method and evaluated the effects of current density and the ionic strength of the medium. The bacterial displacement expressed as the root-mean-square displacement ( $\sqrt{MSD}$ ) of PAO1 cells was found to remain almost the same, irrespective of current density. However, the local dynamics of bacterial communities were quite different when current densities were

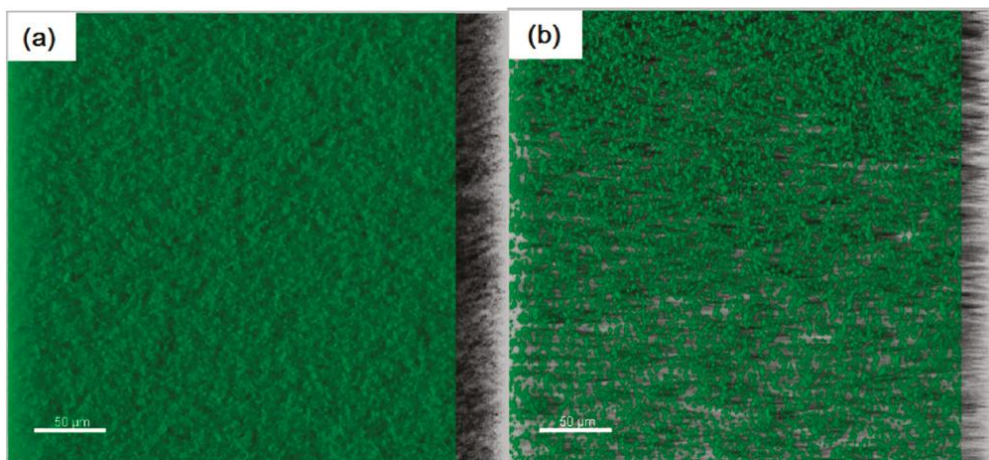


**Figure 5.8.** Confocal laser scanning microscopy (CLSM) images acquired after 24 h of biofilm growth (scale bar: 50  $\mu\text{m}$ ), (a) biofilms growth under non electric field, (b) biofilm growth under applied electric current (15  $\mu\text{A}/\text{cm}^2$ ).

varied. The bacterial displacement distribution shows that as the current density increased, the bacteria were more likely to be oscillating in the adhered position. As the ionic strength increased, the bacterial displacement decreased due to a stronger electrostatic interaction. This study suggests that this tracking method can be used as a valuable tool for quantifying the displacement of bacterial communities on an electrode surface, and for characterizing the dynamics of bacteria under electrical fields. Finally, control of biofilm growth may be possible by changing the motility of bacterial cells under anodic polarization.

## 5.2. The local viscoelastic behavior of biofilms

In this section, as the second method to characterize the biofilms, the heterogeneity and rheological measurement have been suggested.

### 5.2.1. Effect of $\dot{\gamma}_{at\ the\ wall}$ applied during developing phase on the dynamical heterogeneities in biofilms

Figure 5.9 shows the 3D images of biofilms at ages of 24 h obtained from CLSM to see the effect of  $\dot{\gamma}_{at\ the\ wall}$  applied during growth phase, which is controlled by increasing the flow rate of nutrient solution during growth phase. Green color shows the bacterial cell, and red color shows the dispersed probe particles. Consequently, at the all  $\dot{\gamma}_{at\ the\ wall}$ , the biofilms look that they compose the heterogeneous structure, especially  $\dot{\gamma}_{at\ the\ wall}=118.5$  and  $237.0$  /s as shown in Figure 5.9 (d) and (f). However, it's not perfect to evaluate the structural heterogeneities of biofilms imposed by the different  $\dot{\gamma}_{at\ the\ wall}$  with these kinds of images. Here, we try to quantify the dynamical heterogeneities of biofilms using particle tracking microrheological method, and examine the relation with the microstructural heterogeneity of biofilms.

Figure 5.10(a) shows the non Gaussian parameter ( $\alpha_{2-x}$ ) on the vorticity direction as a function  $\Delta t$  (s) calculated from equation (2.26) on the micron



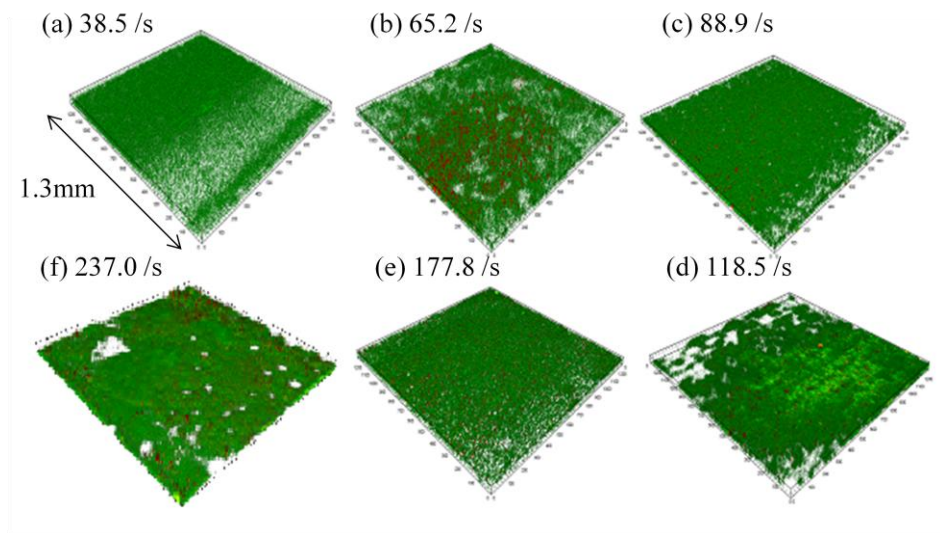


**Figure 5.9.** The microstructure of biofilms depending on wall shear rate

$(\dot{\gamma}_{at\ the\ wall} = \frac{3Q}{2(h_0/2)^2 w_0})$  during developing phase controlling by flow rate of

nutrient solution which obtained using Confocal laser scanning microscope

(CLSM) on the observing view with  $1.3\text{ mm} \times 1.3\text{ mm}$ . (a)  $\dot{\gamma}_{at\ the\ wall} = 38.5$ ,

(b) 65.2, (c) 88.9, (d) 118.5, (e) 177.8, (f) 237.0/s. The green color showed

the bacterial cells and red color showed the fluorescent particles dispersed

insides biofilms for tracking.

length scale observing view ( $80 \mu\text{m} \times 80 \mu\text{m}$ ) which smaller than one of 3D images in Figure 5.9. To see the dynamical heterogeneities of biofilms, the dynamics of probe particles dispersed inside biofilms at age of 24 h and at height of  $10 \mu\text{m}$  from the adhered surface is measured using particle tracking microrheological method. This procedure is repeated with increased  $\dot{\gamma}_{at\ the\ wall}$ . Here, when the particles are dispersed in the homogeneous materials,  $\alpha_2$  becomes close to 0, while  $\alpha_2$  is larger than 0 inside heterogeneous materials [102]. Figure 5.10(b) shows the  $\alpha_2$  on the vorticity ( $\alpha_{2\_x}$ ) and flow direction ( $\alpha_{2\_y}$ ) as a function of  $\dot{\gamma}_{at\ the\ wall}$  at  $\Delta t = 1$  s, that clarify the effect of  $\dot{\gamma}_{at\ the\ wall}$  on the dynamical heterogeneities. Here, to get the representative value, we selected four spot randomly insides biofilms on each  $\dot{\gamma}_{at\ the\ wall}$ . After the dynamical heterogeneity is possessed maximum on  $\dot{\gamma}_{at\ the\ wall} = 88.9$  /s, then they are decreased with  $\dot{\gamma}_{at\ the\ wall} > 88.9$  /s. Respectively, at  $\dot{\gamma}_{at\ the\ wall} = 88.9$  /s, they shows maximum values with  $\alpha_{2\_x} = 40$ , and  $\alpha_{2\_y} = 55$ , while they shows minimum values with  $\alpha_{2\_x}, \alpha_{2\_y} = 1.2$  at  $\dot{\gamma}_{at\ the\ wall} = 237$  /s. However, even the minimum  $\alpha_2$  value at high  $\dot{\gamma}_{at\ the\ wall}$  is larger than  $\alpha_2 = 0.01 - 0.03$  of MW 600k Polyethylene oxide (PEO) 1.2 wt% aqueous solution as a representative totally homogeneous

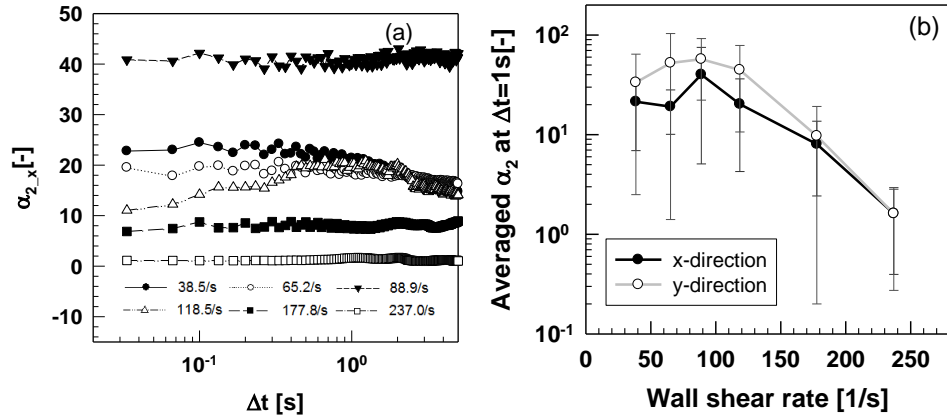


**Figure 5.10.** (a) Non-Gaussian parameter ( $\alpha_{2,x}$ ) on the vorticity direction under varied  $\dot{\gamma}_{at\ the\ wall}$  (38.5 - 237.0 /s) calculated from equation (2.26) using particle tracking microrheological method on the observing view ( $80\ \mu\text{m} \times 80\ \mu\text{m}$ ) after 24 h developing to show the dynamical heterogeneity. (b) Averaged  $\alpha_2$  at  $\Delta t = 1$ s under varied  $\dot{\gamma}_{at\ the\ wall}$  (38.5 - 237.0 /s) with x- (vorticity) and y-axis (flow). On each  $\dot{\gamma}_{at\ the\ wall}$ , we selected four different regions randomly inside biofilms to get a representative value and calculate the error bar.

sample (see Figure 2.3). Also, according to Dibble et al.'s definition, the colloidal gels compose the most heterogeneous structure at  $\alpha_2 = 1.2$  when they measure the dynamical heterogeneity [72]. With referring to the mentioned values, we can conclude that the bacterial community biofilms always compose the heterogeneous microstructure from Figure 5.10, showing more heterogeneous structure at low  $\dot{\gamma}_{at\ the\ wall}$ .

Also, when we compare the vorticity- and flow-directional effect on  $\alpha_2$  in Figure 5.10(b), the difference between  $\alpha_{2\_x}$  and  $\alpha_{2\_y}$  diminish under high  $\dot{\gamma}_{at\ the\ wall}$ . Finally,  $\alpha_{2\_x}$  and  $\alpha_{2\_y}$  are coincided at  $\dot{\gamma}_{at\ the\ wall} = 237$  /s as shown in Figure 5.10(b). Besides, the standard deviation on the flow direction ( $\alpha_{2\_y}$ ) is more significant than one of the vorticity direction ( $\alpha_{2\_x}$ ), which results of the four different spots are randomly sampling. The biofilms under low  $\dot{\gamma}_{at\ the\ wall}$  growth have the structural anisotropy on the xy plane which induced dynamical heterogeneity of Figure 5.10, particularly compose less heterogeneous structure on the vorticity direction. As the one of the causes with structural anisotropy, we might assume that the bacterial cells forms the streamer on the flow direction with higher shear stress [35]. However, further study needs to clarify the mechanism how the anisotropic microstructure has been affected by the  $\dot{\gamma}_{at\ the\ wall}$  on growth phase. Then, at

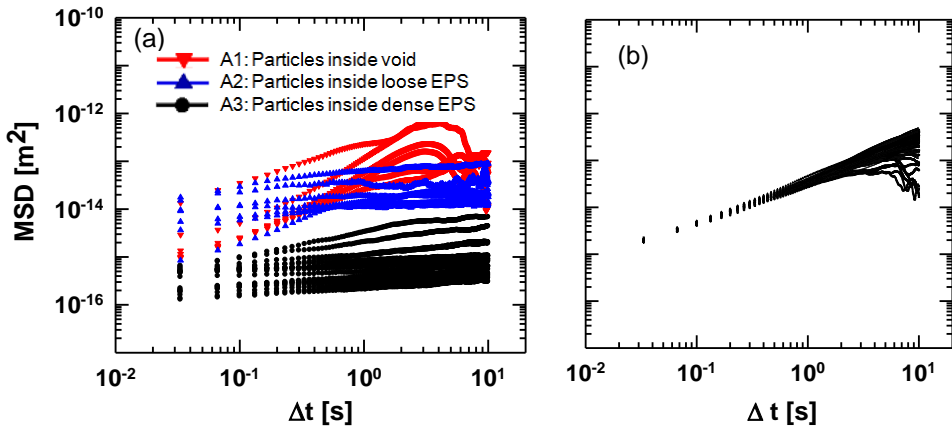


**Figure 5.11.** The MSD plots of individual particles over time inside observing view ( $80 \mu\text{m} \times 80 \mu\text{m}$ ). (a) Biofilms at  $\dot{\gamma}_{at\ the\ wall} = 88.9 \text{ /s}$ , at a height of  $20 \mu\text{m}$  and at ages of 24 h. They are classified to three groups of particles (A1, A2, and A3) where their positions according to the slope of MSD curve and order of MSD. (b) MW 600k Polyethylene oxide (PEO) 1.2 wt% aqueous solution as a reference material.

the next section, we try to find the relation with dynamical heterogeneities and microstructure of biofilms by comparing the local dynamics at  $\dot{\gamma}_{at\ the\ wall} = 88.9 /s$  and  $237 /s$ .

### 5.2.2. The local dynamics at low $\dot{\gamma}_{at\ the\ wall}$ (88.9 /s)

Figure 5.11(a) shows MSD tracks of individual particles dispersed inside biofilms after developing biofilms with  $\dot{\gamma}_{at\ the\ wall} = 88.9 /s$ . The results are observed at one randomly selected region on  $(80 \mu\text{m} \times 80 \mu\text{m})$  among four regions which were used at the Figure 5.10(b). The local dynamics is presented by the MSD as a function of  $\Delta t$ . Figure 5.11(b) shows the MSD tracks of MW 600k PEO 1.2 wt% aqueous solution as a homogeneous reference sample. In Figure 5.11(b), all tracks converge on one curve, especially at the short time scale. In contrast, MSD tracks inside biofilms are spread in the range of  $10^{-12} - 10^{-16} \text{ m}^2$ , following wide distribution. The MSDs and the slope of MSDs are highly dependent on the whether they are in the biofilms as shown in Figure 5.11(a). By analyzing the MSD values and the slope of MSDs, the particles are classified to the three different groups inside measured region of  $(80 \mu\text{m} \times 80 \mu\text{m})$  where they are inside biofilms:

1) Region A1 shows Newtonian fluid behavior with the slope of MSDs ( $\beta$ )

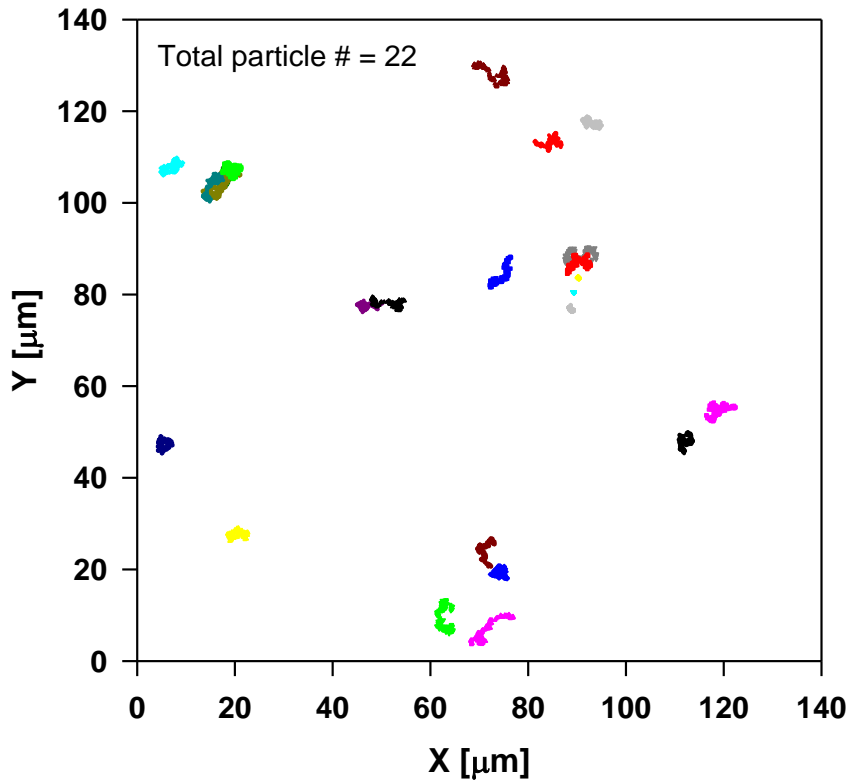


**Figure 5.12.** A spatial map of mechanical microenvironments of the particle trajectories inside biofilm structure. The each color means the one particle's motion for 10 s. There is no long-range spatial correlation, suggesting that the length scale of heterogeneity is small—of the order of a particle diameter. (MSD: Mean Square Displacement)

$\sim 1$  [49].

2) Region A2 and A3 show gel-like behavior with the slope of MSDs ( $\beta$ )  $\sim 0$  [67], while they are on the different MSDs. The EPS has known to a kinds of copolymer material with mass distribution, meaning poly-disperse polymer [103, 104]. Here, as the dynamics of probe particle reflect the local property of poly-disperse polymer on the length scale of probe particles, they are on the wide range of MSDs. As following the EPS property, the biofilms shows spectrum of elastic relaxation times by Shaw et al. [17]. Based on these results, we can find the origin of dynamical heterogeneity on biofilms.

On the other hand, when we calculate mean  $G'$  and  $G''$  using equation (2.20) for four different set of biofilms on observing view ( $80 \mu\text{m} \times 80 \mu\text{m}$ ) (see, Figure 5.13), the rheological property of biofilms were similar or lower 1-2 order than those from the other research [37, 105-108] although the rheological properties of biofilms are dependent on the experimental conditions such as the kinds of strain, the concentration of bacterial cells to growth, the temperature, the set-up and, etc. The relaxation time from microrheological method is 0.033 s as shown in Figure 5.13, which is shorter than the other research (0.1-10 s order) [105]. As we assume that it's induced by the heterogeneous microstructure of biofilms [46], we try to examine the local viscoelastic behavior of biofilms on the length scale of probe particle



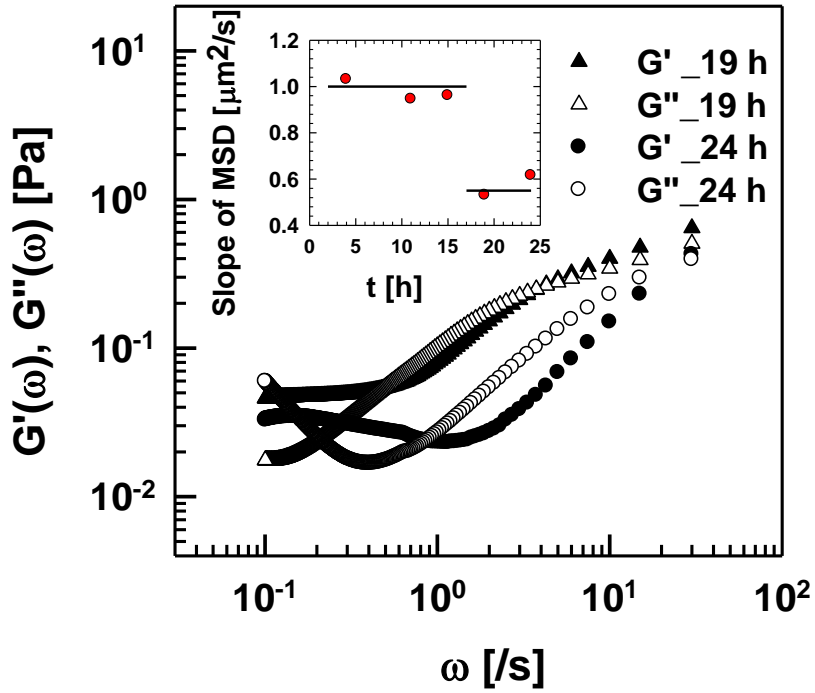


**Figure 5.13.** The average viscoelastic moduli of biofilm after 19 h ( $\Delta$ ,  $\blacktriangle$ ) and 24 h ( $\circ$ ,  $\bullet$ ) obtained using particle tracking microrheological measurement at height = 20  $\mu\text{m}$  from the glass surface. Closed symbol for storage modulus ( $G'$ ), and open symbol for loss modulus ( $G''$ ). Inset: The slope of MSD curve during developing phase at height = 10  $\mu\text{m}$  from the surface. (MSD: Mean Square Displacement)

(~500nm), not the mean property.

Figure 5.14(a) shows local viscoelastic moduli ( $G'$  and  $G''$ ) of individual MSD plots at  $\dot{\gamma}_{at\ the\ wall} = 88.9$  /s in Figure 5.11 using equation (2.20). That is, each curve in Figure 5.14(a) was obtained from the dynamics of each probe particle at a randomly selected region among four regions which were used to calculate dynamical heterogeneity in Figure 5.10. Also, from the local viscoelastic properties in Figure 5.13(a), the local dynamic viscosity was calculated using equation (2.24). Finally, we analyze the microstructure of biofilms by summarizing the individual MSD tracks (Figure 5.11(a)) and local viscoelasticity (Figure 5.14).

1) Region A1:  $G'$  is not captured because this region shows dynamics of Newtonian fluid with slope of MSDs ( $\beta$ )  $\sim 1$  when we apply the equation (2.16). Here,  $G''$  is proportional to the  $\omega$  [80] in Figure 5.14(a). Dynamic viscosity is 0.02 Pa·s which is not dependent to  $\omega$  as shown in Figure 5.14(b) as following the behavior of Newtonian fluid. However, the viscosity inside void is higher than the viscosity of nutrient solution  $\sim 0.005$  Pa·s which is measured using conventional rheometry. This phenomenon is affected by the structure of biofilms, and we suppose some situations are involved with the various kinds of structure inside biofilms. At first, the probe particles might be confined inside the small size of void surrounded by the EPS. In this case,

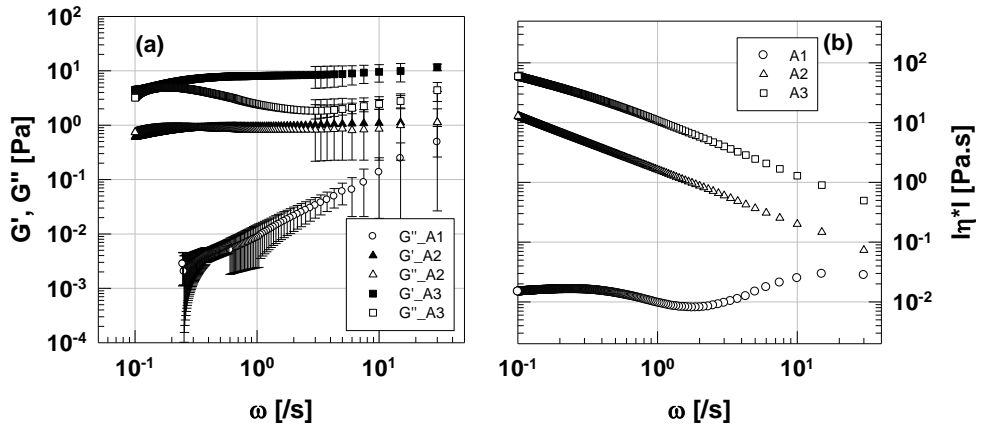


**Figure 5.14.** The local viscoelastic moduli from particle tracking microrheology calculated with individual MSD plot of Figure 5.11(a) at  $\dot{\gamma}_{at\ the\ wall} = 88.9$   $1/s$  inside observing view ( $80\mu m \times 80\ \mu m$ ). (a)  $G'$ (closed symbol) and  $G''$ (open symbol) for region A1(circle), A2(triangle), and A3(square) as shown in Figure 5.11(a) were calculated from the Euler's equations (equation (2.20)). The error bar was calculated with the individual MSDs at each region. (b) Dynamic viscosity  $|\eta^*|$  was calculated using equation (2.24) from Figure 5.14(a).

as the characteristic length of EPS (<100 nm) is smaller than the size of probe particle (500 nm) [109], it's difficult for particles to infiltrate to the network structure from EPS. Here, the EPS structure might be working as a kind of 'soft wall' as arising the interaction between the particles and EPS structure. Zembrzycki et al. [110, 111] has suggested that the Brownian motion of particle near the cylindrical wall has been reduced by interaction with the wall. Secondly, there has a good chance that the particles inside the void with freely moving bacterial cells [47]. Then, the particles have restrictions from the diffusive motion of bacterial cells which arising the interaction each other.

2) Region A2 and A3 which classified in the Figure 5.11(a): the  $G'$  and  $G''$  show constant value, not depending on the  $\omega$ . It means the chemically formed gel-like behavior [112] with  $G' \sim 1$  Pa for region A2, and 10 Pa for region A3. Based on these results, our founding put on emphasis that bacteria have formed the network structure composed with loose and dense domain on the micron length scale at the low  $\dot{\gamma}_{at\ the\ wall}$ . And the structural diversity on micro-scale gives a strong heterogeneity of biofilms as shown in Figure 5.10(b).

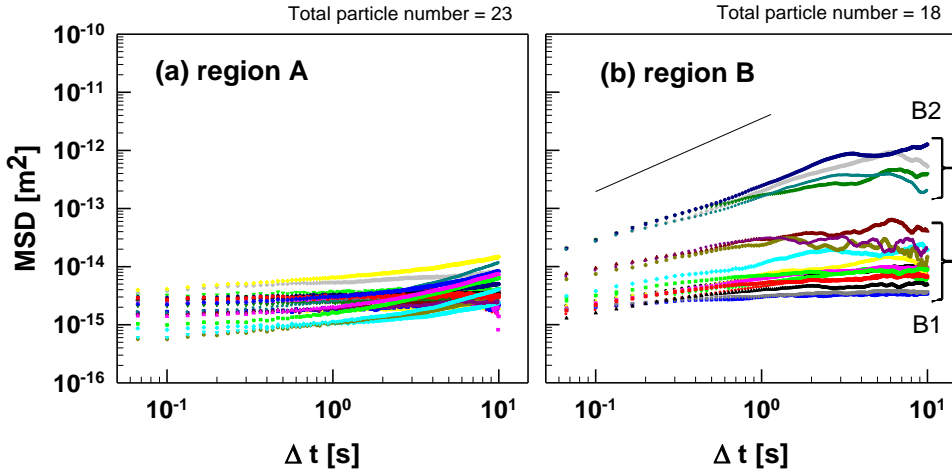


**Figure 5.15.** The MSD tracks of individual particles over time inside observing view ( $80 \mu\text{m} \times 80 \mu\text{m}$ ) biofilms at  $\dot{\gamma}_{\text{at the wall}} = 237 \text{ /s}$ , at a height of  $20 \mu\text{m}$  and at ages of 24 h. (a) Region A  $\dot{\gamma}_{\text{at the wall}} = 237 \text{ /s}$  with averaged  $\alpha_2 = 0.75$ , and (b) Region B  $\dot{\gamma}_{\text{at the wall}} = 237 \text{ /s}$  with averaged  $\alpha_2 = 2.48$ . Region A  $\dot{\gamma}_{\text{at the wall}} = 237 \text{ /s}$ : The MSD curves showed gel-like motion. Region B  $\dot{\gamma}_{\text{at the wall}} = 237 \text{ /s}$ : They are classified to two groups of particles (B1 and B2) where their positions according to the slope of MSD curve and order of MSD.

### 5.2.3. The local dynamics at high $\dot{\gamma}_{atthewall}$ (237 /s)

Figure 5.15 shows individual MSD tracks of two different regions with  $\alpha_2 = 0.75$  (Region A), 2.48 (Region B) at  $\dot{\gamma}_{atthewall} = 237$  /s which the dynamical heterogeneity is lowest as shown in Figure 5.10(b). Here, we try to find why the high shear rate during growth causes the low dynamical heterogeneity in biofilms as shown in Figure 5.10(b). Each region in Figure 5.15 is randomly selected with (80  $\mu\text{m}$   $\times$  80  $\mu\text{m}$ ) inside biofilms. Firstly, in Figure 5.15(a), the all particle in the region A $_{\dot{\gamma}=237/s}$  are captured inside network structure by following  $\langle r^2(\Delta t) \rangle = 2nD(\Delta t)^\beta$  with  $\beta \sim 0$  [49, 72] which is corresponding to the microrheology of gels [112-115]. Besides, the distribution of MSD tracks in Figure 5.15(a) is much narrower than the one of biofilms at  $\dot{\gamma}_{atthewall} = 88.9$  /s in Figure 5.11(a). Secondly, in Figure 5.15(b), the other selected region B $_{\dot{\gamma}=237/s}$  on (80  $\mu\text{m}$   $\times$  80  $\mu\text{m}$ ) shows the pleatau region (B1 $_{\dot{\gamma}=237/s}$ ) and freely motion (B2 $_{\dot{\gamma}=237/s}$ ) at the same time. We calculate the viscosities with MSD tracks following the slopes  $\sim 1$  using equation (2.26) on the B2 $_{\dot{\gamma}=237/s}$ , then the results are on 0.02 - 0.05 Pa·s. When we compare these results with the viscosities at region A1 $_{\dot{\gamma}=88.9/s}$  in Figure 5.14(b), the viscosity of the particles with slope of MSD  $\sim 1$  are

similar, presenting the free particles in the void. However, at  $\dot{\gamma}_{atthewall} = 88.9$  /s, the pleatau MSD tracks in region A2 $_{\dot{\gamma}=88.9/s}$  and A3 $_{\dot{\gamma}=88.9/s}$  are distributed widely positioning on  $10^{-13} - 10^{-16} \text{ m}^2$  as shown in Figure 5.11(a). When we used the equation (2.20), the range of  $G'$  are calculated with 0.05 Pa – 15 Pa as shown in Figure 5.14(a). At  $\dot{\gamma}_{atthewall} = 237$  /s, region A $_{\dot{\gamma}=237/s}$  and B1 $_{\dot{\gamma}=237/s}$ , MSDs are observed on the similar values. Here, the MSDs of elastic region that following  $\langle r^2(\Delta t) \rangle = 2nD(\Delta t)^\beta$  with  $\beta \sim 0$  are  $3 \times 10^{-15} - 4 \times 10^{-16} \text{ m}^2$ , which are substituted to  $G'$  with 1.7 – 11 Pa using equation (2.20). Based on these results, we confirm that the EPS has formed high density gel structure at high  $\dot{\gamma}_{atthewall}$ , showing different appearance with the results at region A $_{\dot{\gamma}_{atthewall}=88.9/s}$  on the local  $G'$ .

Figure 5.16 shows van-Hove correlation function of  $\dot{\gamma}_{atthewall} =$  (a) 88.9 /s, and (b) 237 /s, at  $\Delta t = 1$  s. The results are calculated using all dispersed probe particles in the observing view with (80  $\mu\text{m} \times 80 \mu\text{m}$ ) at each region. Here,  $\Delta x$  is mean displacement of particles, and  $G_s(\Delta x, \Delta t = 1s)$  is probability distribution at each  $\Delta x$ . As following the random Brownian motion,  $G_s(\Delta x)$  shows maximum point at  $\Delta x = 0$ , and the distribution should be symmetric [116]. For homogeneous solution,  $G_s(\Delta x)$  should be

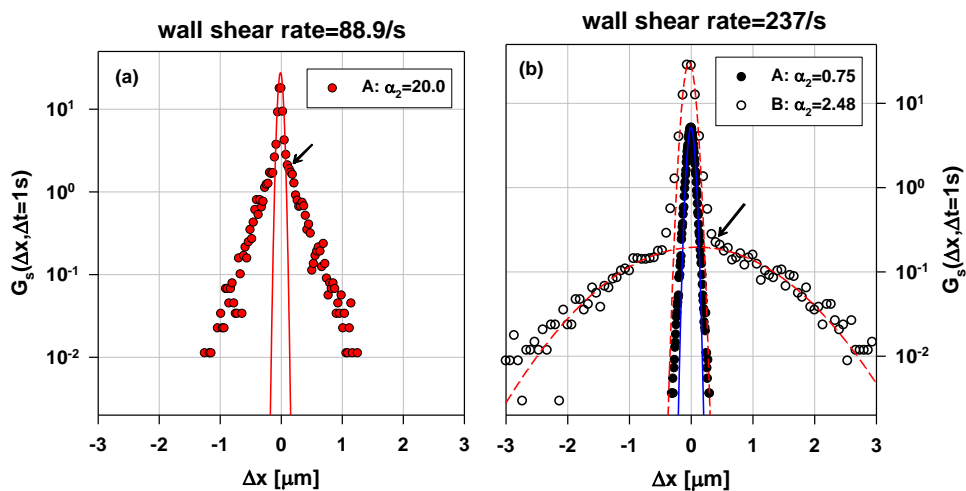


**Figure 5.16.** Van Hove correlation function at  $\dot{\gamma}_{at\ the\ wall} =$  (a) 88.9 /s, and (b) 237 /s at  $\Delta t=1$  s. The results were calculated using all dispersed probe particles in the observing view with (80  $\mu\text{m} \times 80 \mu\text{m}$ ) at each region. The solid line fitted the Gaussian distribution at each van-Hove correlation function.

(a) the data of MSDs were used from region A  $\dot{\gamma}_{at\ the\ wall} =88.9/s$  ( $\alpha_2=20.0$ ) in Figure 5.11(a).

(b) the van Hove correlation function of two representative regions ( $\alpha_2 = 0.75$  (A  $\dot{\gamma}_{at\ the\ wall} =237/s$ ) and 2.48 (B  $\dot{\gamma}_{at\ the\ wall} =237/s$ )) was plotted separately as shown in Figure 5.15. The van Hove correlation function of MW 600k PEO 1.2 wt% aqueous solution was suggested as a reference set (see Figure 2.3).



corresponding with the Gaussian curve (solid line in Figure 2.3) at the all range of  $\Delta x$ . However, in case of biofilms,  $G_s(\Delta x)$  is deviated from the Gaussian curve (red solid line) at  $\dot{\gamma}_{at\ the\ wall} = 88.9 /s$  as shown in Figure 5.16(a). At  $-0.1 < \Delta x < 0.1(\mu m)$ ,  $G_s(\Delta x)$  agrees with Gaussian curve perfectly, but at  $|\Delta x| > 0.1(\mu m)$ ,  $G_s(\Delta x)$  shows big differences with Gaussian curve. In Figure 5.16(b), at  $\dot{\gamma}_{at\ the\ wall} = 237 /s$ , van Hove correlation function of two representative regions ( $\alpha_2 = 0.75$  (A $_{\dot{\gamma}=237/s}$ ) and 2.48 (B $_{\dot{\gamma}=237/s}$ )) was plotted separately as shown in Figure 5.15. In region A $_{\dot{\gamma}=237/s}$ , the  $\alpha_2$  is smaller than the one in region B $_{\dot{\gamma}=237/s}$  because  $G_s(\Delta x)$  (closed symbol in Figure 6(b) corresponds with the Gaussian curve (solid line in Figure 6(b)). In region B $_{\dot{\gamma}=237/s}$ ,  $\alpha_2$  is 2.48 which larger than the one of region A $_{\dot{\gamma}=237/s}$ . Also,  $G_s(\Delta x)$  are separated with two populations clearly in Figure 5.16(b).  $G_s(\Delta x)$  of probe particles showing gel-like motion at  $-0.4 < \Delta x < 0.4(\mu m)$  are similar with those of region A $_{\dot{\gamma}=237/s}$ . But, on the freely dynamics ( $|\Delta x| > 0.4(\mu m)$ ) the width of Gaussian curve was much wider than the one of region A $_{\dot{\gamma}=237/s}$ . This supports that the different dynamic between region B1 $_{\dot{\gamma}=237/s}$  and B2 $_{\dot{\gamma}=237/s}$  in Figure 5.15 is induced by separation with dense elastic EPS and void obviously in Figure 5.15.

Precisely, we fits Gaussian curve for region B1  $\dot{\gamma}=237/s$  and B2  $\dot{\gamma}=237/s$  in isolation using these equations [116]:

$$\begin{aligned} G_{s,fast}(\Delta x, \Delta t = 1s) &= P_1 \exp\left(-0.5\left(\frac{\Delta x + x_0}{b}\right)^2\right) = 0.1963 \exp\left(-0.5\left(\frac{\Delta x + 0.099}{1.0624}\right)^2\right) \\ G_{s,slow}(\Delta x, \Delta t = 1s) &= P_2 \exp\left(-0.5\left(\frac{\Delta x + x_0}{b}\right)^2\right) = 30.7641 \exp\left(-0.5\left(\frac{\Delta x - 0.0036}{0.0775}\right)^2\right) \end{aligned} \quad (5.1)$$

The probability of fast and slow particles was calculated by substituting pre-factor P1 and P2 to this equation:

$$\% \text{ fast}_{-freely} = \frac{P_1}{P_1 + P_2} \text{ and, } \% \text{ slow}_{-gel-like} = \frac{P_2}{P_1 + P_2} \quad (5.2)$$

As a result, 99.36 % of gel-like motion and 0.63 % of freely motion are calculated. Although the portion of freely particles inside biofilms is not high, it might be a condition to induce low dynamical heterogeneity at high  $\dot{\gamma}_{at\ the\ wall}$ . Also, when it compared to the results of  $\dot{\gamma}_{at\ the\ wall} = 88.9 /s$  in Figure 5.16(a), the deviation from Gaussian curve (solid line) appears sharper in case of region B  $\dot{\gamma}=237/s$  as shown in Figure 5.16(b). At low  $\dot{\gamma}_{at\ the\ wall}$ , the separation of two populations is not an abrupt deviation in Figure 5.16(a). It presented that the network of EPS composed with loose and dense structure at the same time as examined in Figure 5.11 and 5.14.

Based on these results, the strong heterogeneity of biofilms appears to be caused by the structural heterogeneities in the system. The bacterial cells

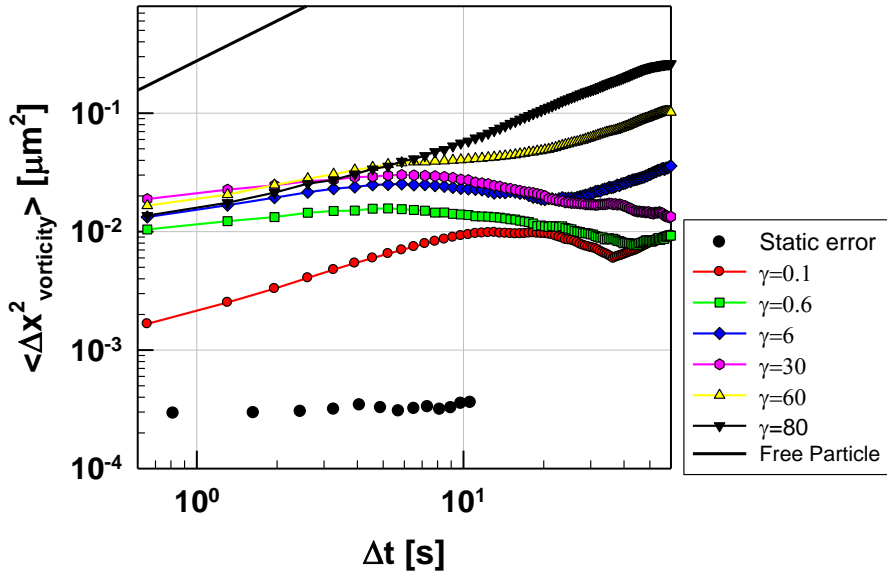
forms network structure of EPS more compact at high  $\dot{\gamma}_{at\ the\ wall}$ . Relatively, the loosely formed network structure presents the strong heterogeneity at low  $\dot{\gamma}_{at\ the\ wall}$  as we confirmed from Figure 5.11 and 5.14. It follows the previous research of Liu et al. and Viera et al. that the density of biofilms increased with high  $\dot{\gamma}_{at\ the\ wall}$  by the cohesive and compact structural property [43, 44]. Therefore, we find that the biofilms is the system of less heterogeneous gel on the micron length scale at high  $\dot{\gamma}_{at\ the\ wall}$ .

In this section, we measured the local viscoelastic behavior using particle tracking microrheological method. And we quantify the dynamical heterogeneities in biofilms under varied  $\dot{\gamma}_{at\ the\ wall}$ . The importance in this study is two-fold: 1) the biofilms shows strong dynamical heterogeneities on the micron length scale when they have grown on the low shear stress conditions. The heterogeneity provides origin of low viscoelasticity when we approach on microrheology. 2) The origin of dynamical heterogeneity on the micron length scale is induced by the diversity of structure inside biofilms such as hollow void, void with freely bacterial cells, and the wide distribution of EPS density. The bacterial cells organize the different network structure (loose or dense density of EPS) depending on the shear stress during growth phase.

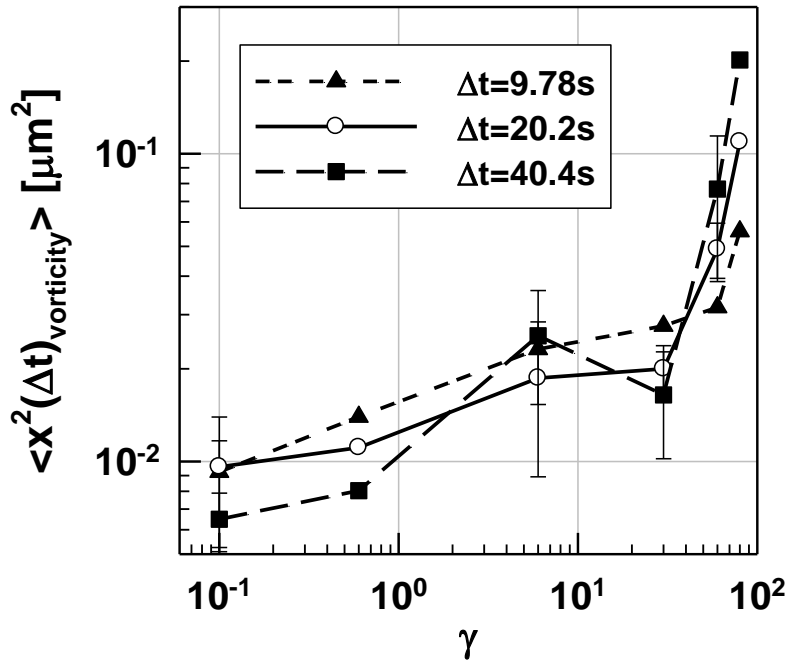
## 6. Dynamics of post-yielding colloidal gels

### 6.1. The MSD curves of post-yielding colloidal gels

We observe a homogenizing effect in which networks break up into clusters that recover rapidly after the cessation of shear. Figure 6.1(a) shows that the slopes of the mean-squared displacement (MSD) for sheared gels increase as a function of the applied strain. This implies that the quiescent gel network breaks down into smaller clusters that exhibit sub-diffusive motion at all applied strains ( $\gamma = 0.1 - 80$ ), with a more pronounced effect at larger applied strains (the MSD slope approaches 0.752 at  $\gamma = 80$ ). At long time scales, the noise seen in some of the MSD curves ( $\gamma = 0.1 - 30$ ) is due to losses in linked trajectories for particles that display vigorous Brownian motion that causes them to drift in and out of the field of view. Figure 6.1(b) shows that the MSD values of the sheared gels (at  $\Delta t = 9.78$  s) increases by an order of magnitude as a function of the applied strain. Because the MSD in the flow direction is larger than that in the vorticity direction for the largest applied strain,  $\gamma = 80$ , we have chosen to consolidate  $\langle x^2(\Delta t) \rangle$  and  $\langle y^2(\Delta t) \rangle$  into an averaged localization length,  $\langle r^2(\Delta t) \rangle$ .



(a)



(b)

**Figure 6.1.** Mean-squared displacement (MSD) curves of colloidal gels after applying a step strain with  $\gamma = 0.1$  to 80 at  $\dot{\gamma} = 40 \text{ s}^{-1}$ . (a) Evolution of  $\langle x^2 \rangle$  as a function of  $\Delta t$  from a completely arrested gel state (black open symbols) to a completely fluidized suspension (solid line), with the following applied deformations:  $\gamma = 0.1$ ,  $\gamma = 0.6$ ,  $\gamma = 6.0$ ,  $\gamma = 30$ , and  $\gamma = 80$ . Closed black symbols represent static noise level obtained from photo-polymerized sample. (b) Localization lengths in the  $x$  (vorticity) directions as a function of strain for  $\Delta t = 9.78, 20.2, 40.4$  s. Error bars shown here are standard deviations from 3 independent measurements.

## 6.2. Strain-induced dynamical heterogeneities in colloidal gels

We use the self-part of the van Hove correlation function in the  $x$ -direction from equation (2.25) where  $N$  is the total number of particles, as a dynamical measure of the single particle displacement probability. A significant deviation from a Gaussian distribution in  $G_s(x, \Delta t)$  is typical for short-ranged attractive systems close to dynamical arrest boundaries [71, 73], and a narrow distribution is typically observed for gels that are deeply quenched. Figure 6.2(a), (b), and (c) show that the van Hove distribution after yielding broadens gradually, as  $\gamma$  increases from 0.1 to 6.0, and finally to 80. The complete  $G_s(x, \Delta t = 9.78 \text{ s})$  data set for all applied strains can be found in Figure 6.3. This is in contrast to the dynamics of the quiescent gels, which follow a much narrower non-Gaussian distribution (open symbols in Figure 6.2(a) and (b)). Gels that have undergone yielding display superimposed bimodal Gaussian distributions, a signature of particles that are diffusing at two distinct velocities [67, 81]. Since the superimposed bimodal distributions deviate from ideality, in Figure 6.4 we quantify the difference using the non-Gaussian parameter,  $\alpha_2$ , as defined elsewhere [72]. The non-Gaussian parameter is typically used to characterize deviations from a completely fluidized sample with a Gaussian distribution, particular at short time scales

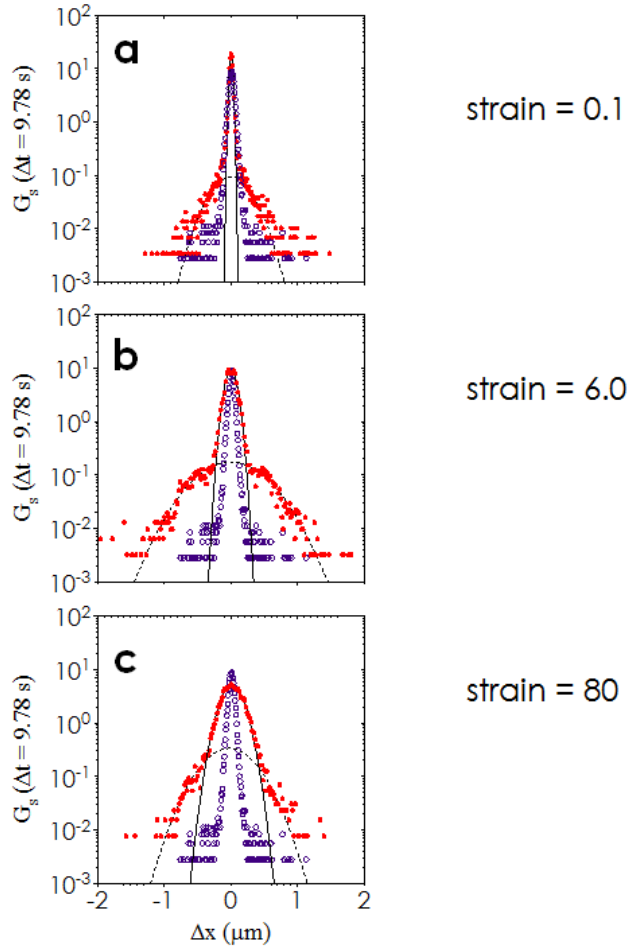


**Figure 6.2.** Superimposed bimodal single particle displacement distributions of sheared colloidal gels showing slow and fast subpopulations. Comparison between the  $G_s(\Delta t = 9.78 \text{ s})$  of quiescent colloidal gels (purple open symbols) and that of gels sheared at (a)  $\gamma = 0.1$ , (b)  $\gamma = 6.0$ , and (c)  $\gamma = 80$ . Red closed symbols represent data for gels that have undergone yielding, with Gaussian distributions fit to their slow (solid line) and fast (dashed line) subpopulation of particles.



[117]. Here,  $\alpha_2$  decreases significantly from its quiescent value after shearing at large deformations ( $\gamma = 80$ ), approaching the value of zero for a completely fluid suspension. At small deformations ( $\gamma = 0.1$ ), the values of  $\alpha_2$  remains similar to the original gel network (see Figure 6.4). We separate the particles in sheared gels into slow (solid lines in Figure 6.2(a) and (b)) and fast subpopulations (dashed lines in Figure 6.2(a) and (b)) based on the discontinuities seen in the van Hove self-correlation function. A discontinuous point is assigned when the difference between the experimental data points and a fitted Gaussian distribution is greater than 1000%. It is interesting to note that at  $\gamma = 0.1$ , the slow colloidal displacement exhibits a similar Gaussian distribution to that seen in the quiescent gel. This suggests that the perturbation at  $\gamma = 0.1$  is insufficient to push the majority of particles in the rigid core out of their attractive potential wells, and that only a small amount of particles are eroded by shear. In contrast, slow clusters diffuse about rapidly at  $\gamma = 80$ , and display a wider Gaussian distribution than the quiescent gel network.

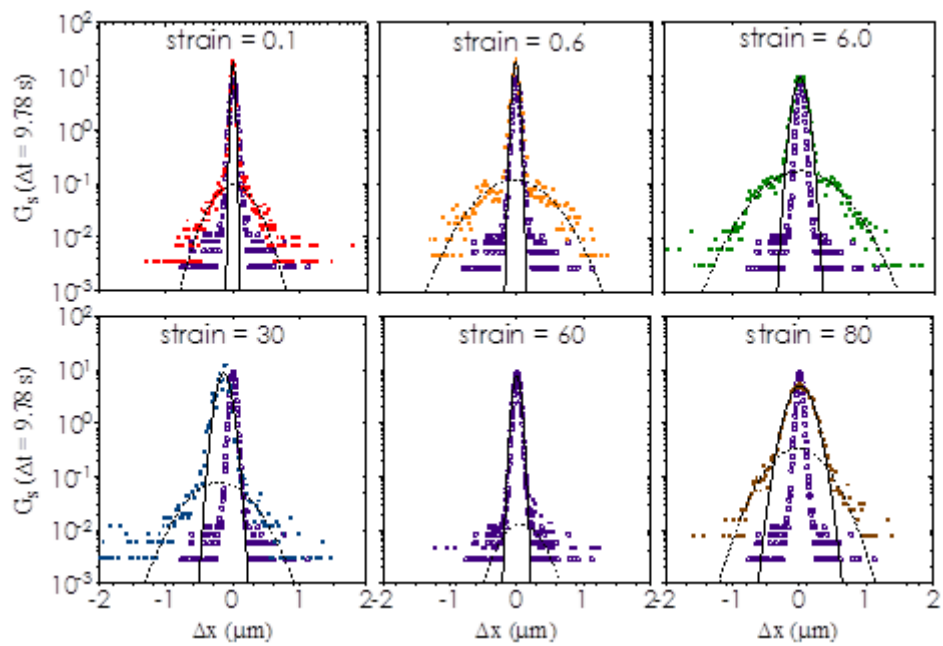


**Figure 6.3.** Self-part of van Hove correlation for all strains.

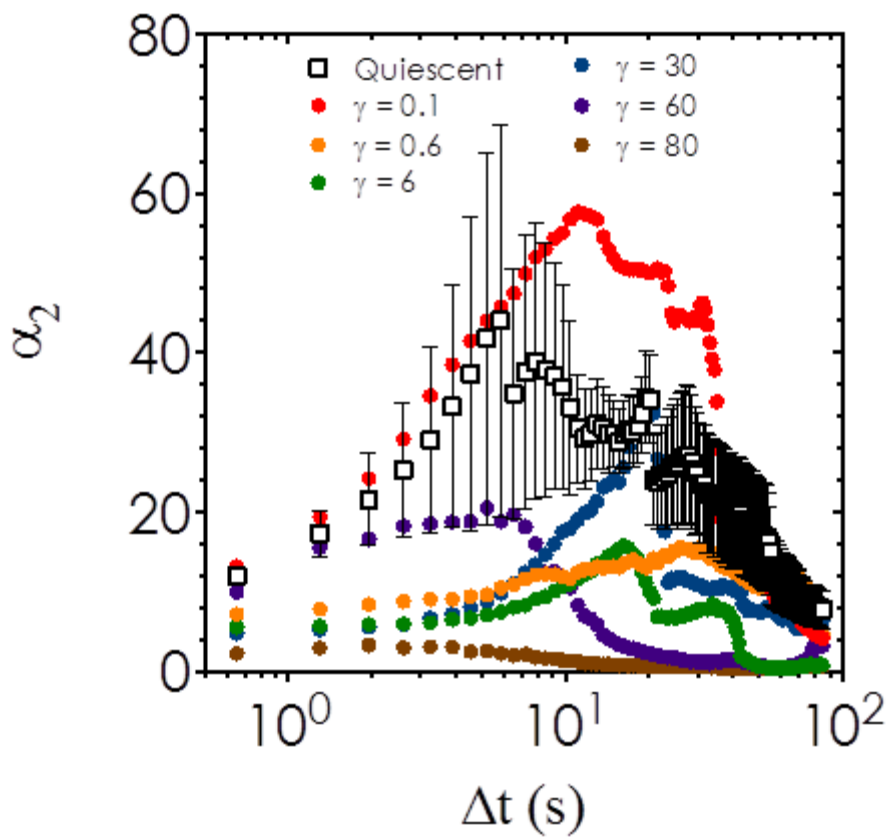


**Figure 6.4.** The non-Gaussian parameter ( $\alpha_2$ ) of post-yielding colloidal gels under varied strain (0.1-80)

### 6.3. Modulus-dynamics relationship

Existing micromechanical models show that attractive colloidal systems often include a gamut of weakly and strongly bonded particles, and that rupture is a result of the collapse of weak bonds [58, 118]. Our observation of a bimodal  $G_s(x, \Delta t)$  distribution after yielding in corroborates this argument by showing evidence of two classes of particles: a fast subpopulation which diffuses freely, and a slow subpopulation which exists in clusters that support an elastic stress after yielding. We develop this idea further by separating the localization lengths of fast and slow particles,  $\langle r_{\text{fast}}^2(\Delta t) \rangle$  and  $\langle r_{\text{clust}}^2(\Delta t) \rangle$ , based on the cutoff criterion defined for the van Hove self-correlation. FIG. 6.5 shows the evolution of  $\langle r_{\text{fast}}^2(\Delta t) \rangle$  and  $\langle r_{\text{clust}}^2(\Delta t) \rangle$  as a function of  $\gamma$  for  $\Delta t = 9.78, 20.2, \text{ and } 30.0 \text{ s}$  [49]. As strain increases, the displacement of fast particles remains relatively constant, while the displacement of slow particles at  $\gamma = 80$  is about four times larger than that at  $\gamma = 0.1$ . The slope of the MSD curves of these fast particles are lower than that of individual free particles, suggesting that fast particles exist in small aggregates that exhibit Brownian motion on the order of their aggregate size. Slow particles exist in slowly diffusing clusters, which become increasingly mobile at  $\gamma > 0.6$ . This increase as a function of strain is a result of the breakage of weak bonds within the rigid network structure.

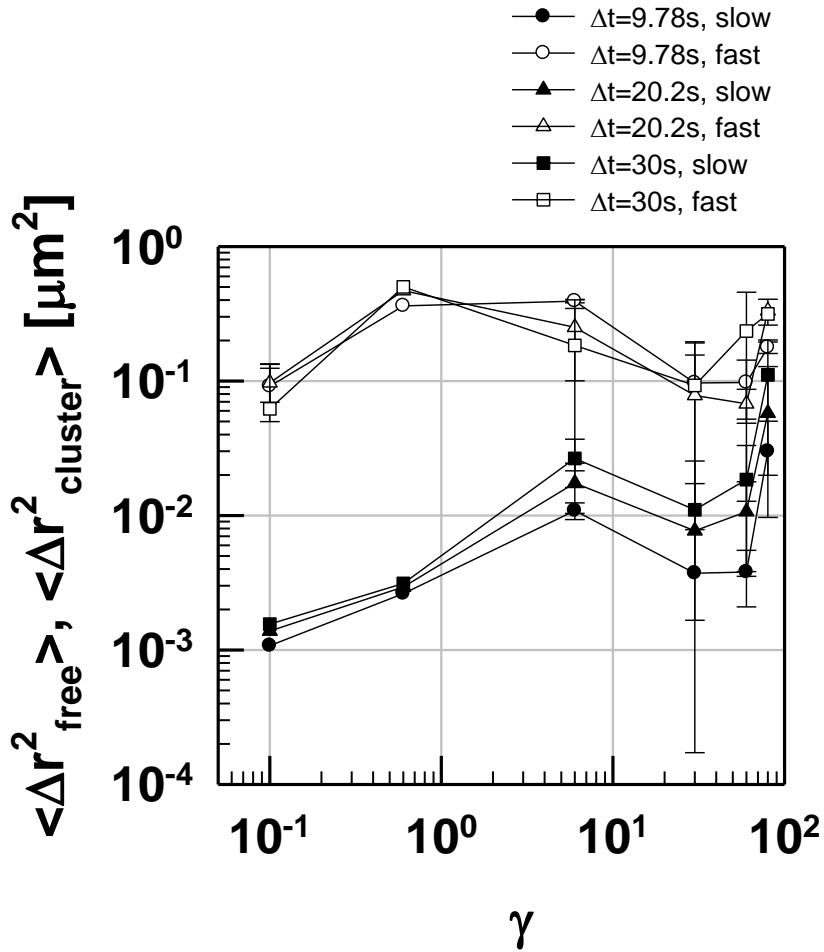


**Figure 6.5.** MSD curves for slow and fast particles in sheared colloidal gels. The change in localization length of fast-moving particles ( $\langle r^2_{\text{fast}}(\Delta t) \rangle$ , open symbols) versus slowly-diffusing aggregates ( $\langle r^2_{\text{clust}}(\Delta t) \rangle$ , closed symbols) as a function of  $\gamma$ , for  $\Delta t = 9.78$  s, 20.2 s, and 30.0 s.

Our idea is that slow particles make up the rigid clusters that remain after the application of step strain, while fast particles diffuse freely and do not contribute to the elasticity of the yielded sample. To test this hypothesis, we aim to connect the microscopic dynamical measurements to the bulk rheology obtained from rheometry, and to directly address any deviations from theoretical predictions using only the dynamics of the slow clusters. We use a stress-controlled rheometer (AR-G2, TA Instruments) with a 40 mm parallel steel plate geometry (gap = 500  $\mu\text{m}$ ) to perform oscillatory strain sweep and nonlinear stress relaxation measurements. A solvent trap is used to reduce evaporation of the volatile solvent. Gels are presheared at 200 rad/s for 2 minutes and allowed to equilibrate for 2 hours prior to measurements. The oscillatory strain sweep experiments are performed at four different angular frequencies ( $\omega = 0.1, 1, 10, 40$  rad/s, see Figure 6.7) to address the effects of frequency on the theoretical zero-frequency prediction of the elastic modulus. To ensure a closer match with the confocal microscopy experiments, we measure the shear stress in the gel samples,  $G(t, \gamma)$ , before and after the application of the following step strains:  $\gamma = 0.1$  ( $\dot{\gamma} = 4 \text{ s}^{-1}$ ),  $\gamma = 0.6$  ( $\dot{\gamma} = 10 \text{ s}^{-1}$ ), and  $\gamma = 6, 30, 60, 80$  ( $\dot{\gamma} = 40 \text{ s}^{-1}$ ) (see Figure 6.8). The lower shear rates chosen at  $\gamma = 0.1$  and  $0.6$  are a result of instrument limitations on the shortest time scale at which measurements can be taken. The Brownian

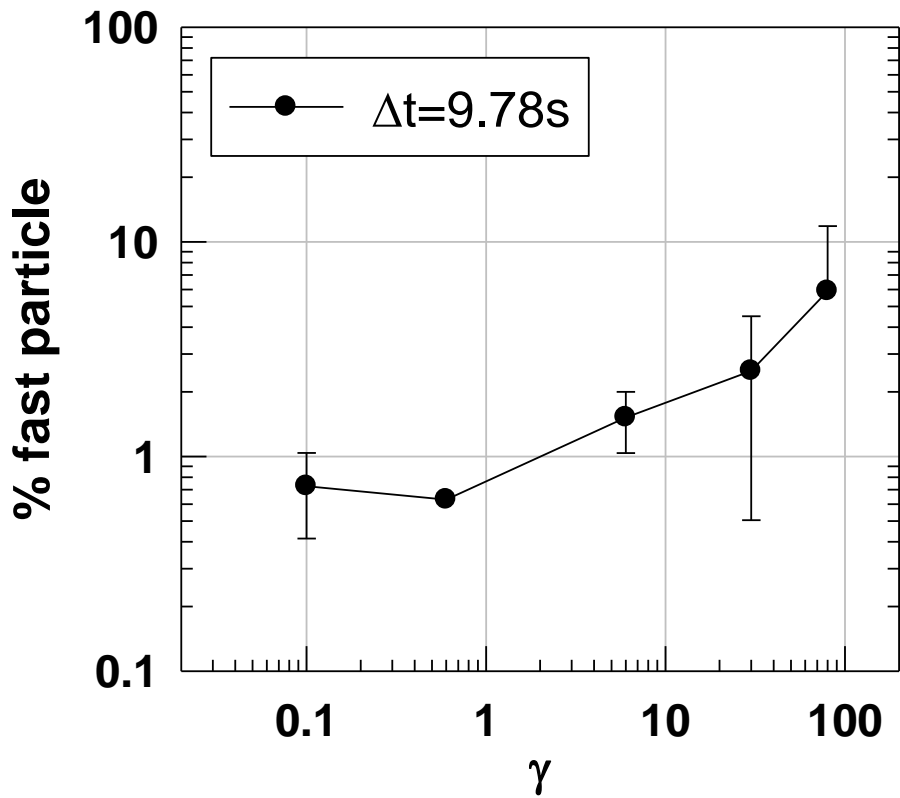


**Figure 6.6.** Relative abundance of fast particles as a function of  $\gamma$ , obtained from Gaussian fits to  $G_s(\Delta t = 9.78\text{ s})$  for the fast subpopulation.

stress,  $G_B(\gamma)$ , defined as the stress measured immediately after the cessation of the applied step strain, shows a steady decrease from 4.34 Pa to 0.0075 Pa as  $\gamma$  increases from 0.1 to 80.

We now demonstrate that decrease in the elastic modulus and the Brownian stress as a function of the applied strain is purely due to the existence of slow-diffusing clusters within the sheared samples. We use MCT-PRISM, a microscopic theory that was developed by Chen and Schweizer to predict the zero-frequency linear elastic modulus of gels with short-ranged attraction,  $G'_{micro}$ :

$$\frac{G'_{micro}(2a)^3}{kT} = 2.32 \frac{\phi a^2}{\langle r^2(\Delta t) \rangle} \quad (6.1)$$

The theoretical prediction shows good agreement with the linear elasticity of silica colloidal gels ( $\phi = 0.20$ ) at a  $\omega = 1$  rad/s [119], but no explanation was given for the choice of a nonzero, fixed frequency in this study. The model over-predicts the modulus by  $\sim 10^2$  when applied to depletion gels at intermediate volume fractions [120]. This was earlier attributed to the formation of dense, non-fractal aggregates. A pre-factor corresponding to the average number of colloids in each cluster has been used to coincide the theoretical predictions with the experimental measurements of elasticity [121]. We begin our test of this theory by substituting  $\langle r^2(\Delta t = 9.78 \text{ s}) \rangle$  for



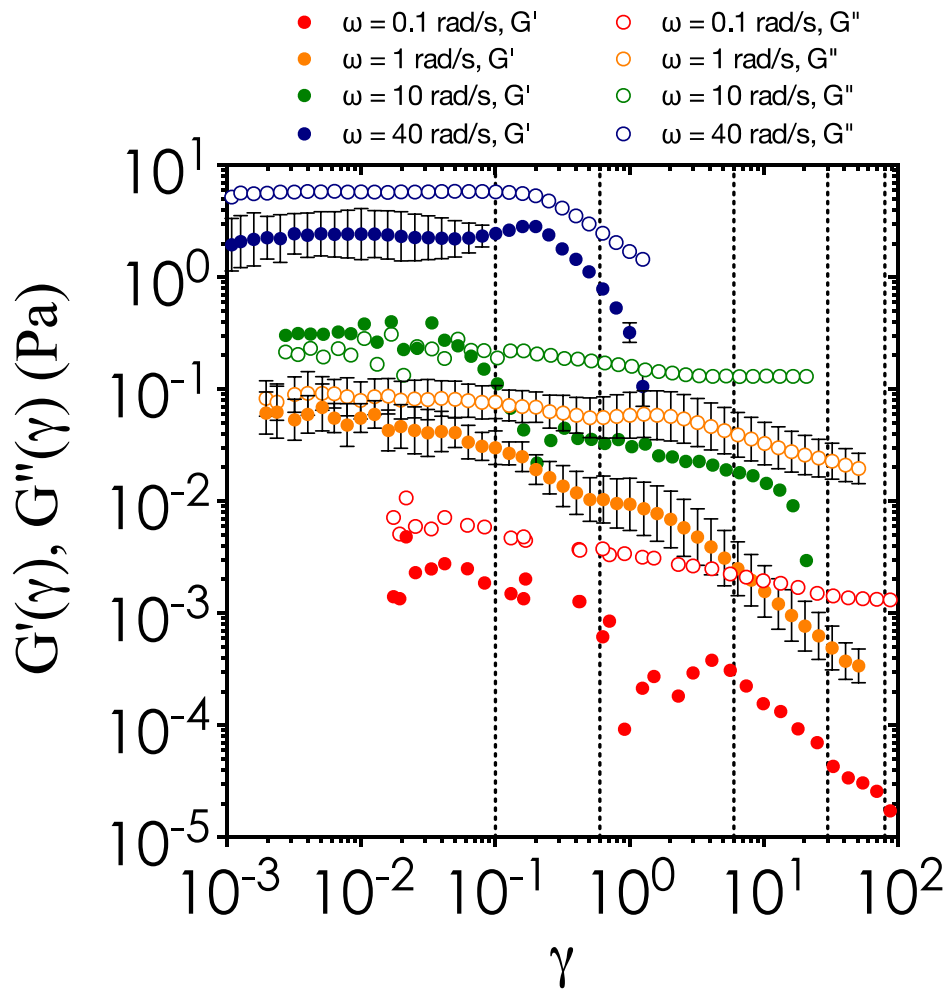


**Figure 6.7.** Strain sweep raw data. Error bars are standard deviations.

(Working on replication of lower frequencies)

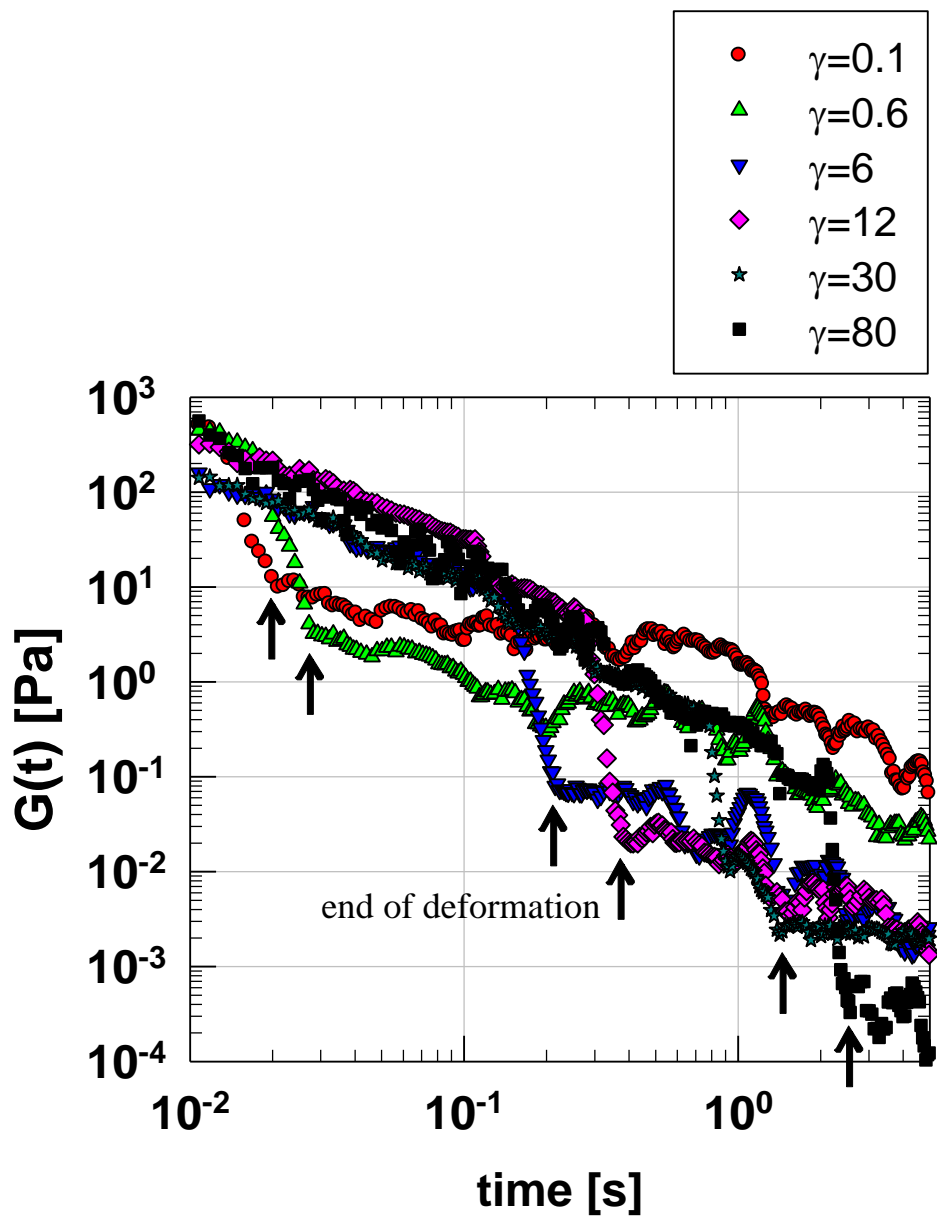
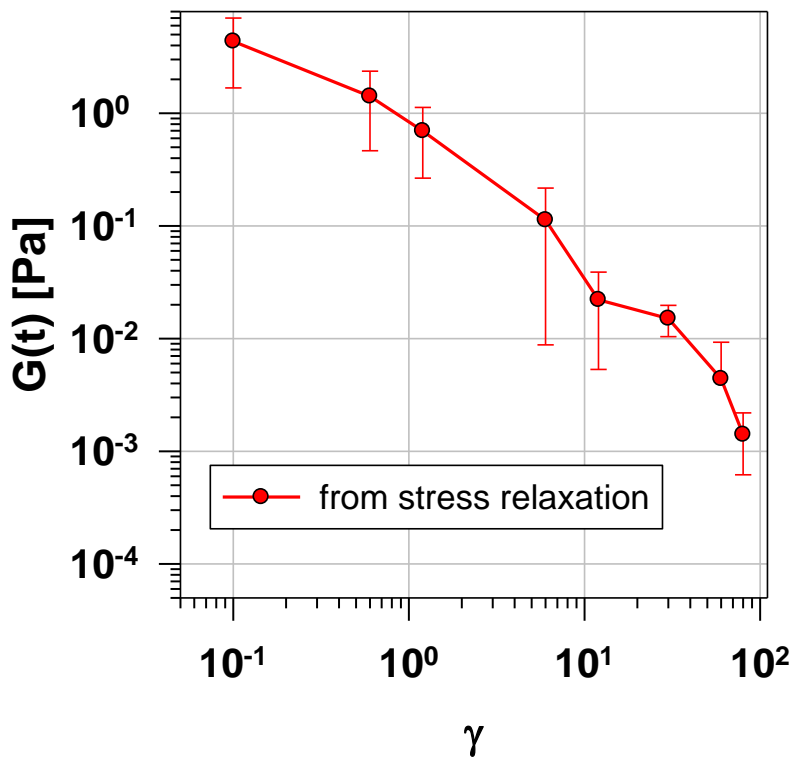


Figure 6.8. Stress relaxation raw data for all strains.



**Figure 6.9.**  $G_B$  defined as the Brownian stress measured immediately after the cessation of the step strain.

all particles (Figure 6.1) into equation 1 to calculate  $G'_{\text{micro}}$  of the yielded gels. For an arrested gel network, we use the plateau value of the MSD ( $\langle r^2 \rangle = 6.49 \times 10^{-4} \mu\text{m}^2$ ) to determine  $G'_{\text{micro}} = 0.612 \text{ Pa}$ . Because of our interest in the nonlinear aspect of yielding, the oscillatory elastic modulus  $G'(\gamma)$  at different  $\omega$  is normalized by the linear value,  $G'_{\text{lin}} = G'(\gamma = 0.1)$ , and the bulk Brownian stress  $G_{\text{B}}(\gamma)$  by  $G_{\text{B,lin}} = G_{\text{B}}(\gamma = 0.1)$ .

Figure 6.10 shows the normalized data points,  $G'/G'_{\text{lin}}$  and  $G_{\text{B}}/G_{\text{B,lin}}$ , plotted along the theoretically predicted values from MCT-PRISM. When we substitute the combined MSD values of both slow and fast particles into equation (6.1),  $G'_{\text{micro}}/G'_{\text{micro,lin}}$  (open triangles) shows good agreement with  $G'/G'_{\text{lin}}$  and  $G_{\text{B}}/G_{\text{B,lin}}$  ( $\gamma = 0.1$  and  $0.6$ ) but consistently over-predicts the linear contribution to the measured modulus at higher strains ( $\gamma = 6.0, 30, 80$ ). A much better agreement between theory and experiment is seen when we use only the slow MSD values in the prediction,  $G'_{\text{clust}}/G'_{\text{clust,lin}}$  (Figure 6.10, solid line), with the confidence intervals of the predictions (Figure 6.10, dashed line) plotted alongside to account for the error in the MSD values.

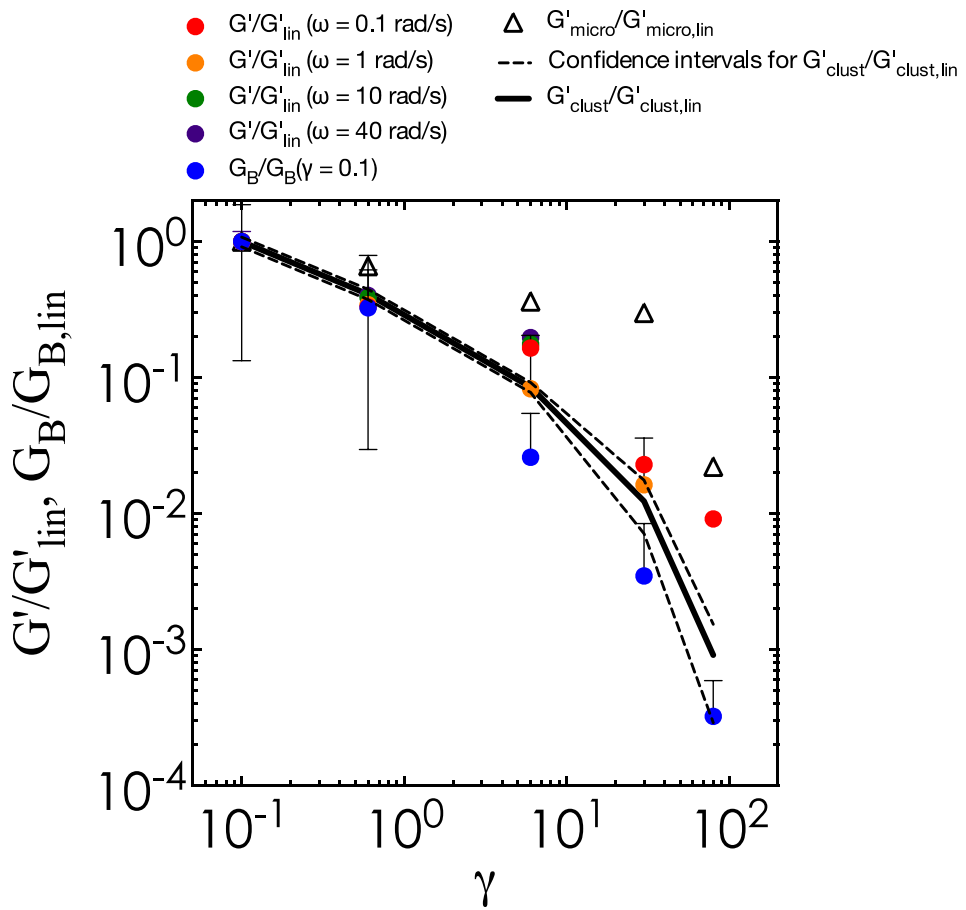


**Figure 6.10.** Comparison of bulk rheological measurements to theoretical predictions from MCT-PRISM. The experimental measurements consist of: 1) the elastic modulus from oscillatory strain sweep normalized by the linear value at  $\gamma = 0.1$ , for  $\omega = 0.1$  rad/s (red), 1.0 rad/s (orange), 10 rad/s (green), and 40 rad/s (purple); and 2) the Brownian stress from stress relaxation measurements, normalized by the linear value at  $\gamma = 0.1$ , after application of a step strain (blue closed symbols). Errors bars are standard deviations from the mean. The theoretical predictions are that from the combined MSD from slow and fast particles (open triangles), and from the MSD of the slow subpopulation (solid line) at  $\Delta t = 9.78$  s. Dashed line represents the confidence interval of the theoretical prediction based on standard deviations carried over from the MSD values.

The importance of our work is two-fold: 1) we provide experimental evidence that shearing weak depletion gels at intermediate volume fractions with large deformations and high shear rates causes an erosion of fast-moving aggregates from a slowly-diffusing rigid core; 2) we show that the range of prediction for ensemble-averaged theories, such as MCT-PRISM, can be extended by accounting for the microstructural and dynamical heterogeneities that often arise in cases of nonlinear flow with high shear rates. These models are excellent at predicting the linear elasticity of soft materials, particularly in homogenous glasses and gels. The overestimation in modulus arises at increasing flow rates due to the assumption that all particles contribute equally to the elasticity. In our study, MCT performs much better at  $\gamma = 0.1$  and  $0.6$ , where the divergence of the slow subpopulation from a quiescent gel network is small (Figure 6.3(a)). Here, the applied shear is insufficient to significantly alter the microstructure and dynamics of the gel. When the dynamical difference between the slow and fast subpopulations becomes significant at  $\gamma \geq 6$  (Figure 6.3 (b), (c)), the predicted modulus increasingly overestimates both  $G'/G'_{\text{lin}}$  and  $G_B/G_{B,\text{lin}}$ .

## 7. Conclusions

In this study, we tried to quantify the dynamical heterogeneities of the complex fluids such as bacterial community biofilms and depleting colloidal gels by applying the particle tracking microrheological method.

Firstly, we verified the set-up microrheological method with totally homogeneous system such as three kinds of polymer solution on various concentrations. When the  $G'$  and  $G''$  of polymer solution calculated using the Euler's equation and Maxwell model on the microrheological method, they were well corresponded with those from conventional rheometry.

Secondly, we tried to control and remove the biofilms with two kinds of approaches, depending on their position on developing process using microrheological method. The one is that the bacterial cells adhered to the surface were interrupted by the electric field. By tracking the bacterial cells on the surface, we evaluated the effects of current density and the ionic strength of the medium. The mean bacterial displacement was found to remain almost the same, irrespective of current density. However, the bacterial displacement distribution shows that as the current density increased, the bacteria were more likely to be oscillating in their adhered position. Also, as the ionic strength increased, the bacterial displacement decreased due to a stronger electrostatic interaction with the electrode. These



observations suggest that the motility of bacterial community under anodic polarization might restrict the biofilms growth. As the other approach, we tried to characterize the dynamical heterogeneities of biofilms exposed to different level of shear stress during growth phase. The importance in this research is that the biofilms shows strong dynamical heterogeneities on the micro scale when they have grown on the low shear stress conditions. The origin of dynamical heterogeneity on the micro scale is induced by the diversity of structure inside biofilms such as hollow void, void with freely bacterial cells, and the wide distribution of network density. The bacterial cells organize the different network structure (loose or dense density of EPS) depending on the shear stress during growth phase. Also, the strong heterogeneity provides fundamental of low local viscoelasticity when we have approached on micro-scale.

Fourthly, we provide experimental evidence that shearing weak depletion gels at intermediate volume fractions with large deformations and high shear rates causes a structural evolution of fast-moving aggregates from a slowly-diffusing rigid core. Also, we show that the range of prediction for ensemble-averaged theories, such as MCT-PRISM, can be extended by accounting for the microstructural and dynamical heterogeneities that often arise in cases of nonlinear flow with high shear rates.

Overall, the dynamical heterogeneity of complex fluids gives us an implication to characterize the structural heterogeneity under varied shear stress. When the dynamical heterogeneity gets high values, the microstructure within complex fluids have shown be different kinds. Finally, the findings in this study set the importance of dynamical heterogeneity in the rheology of complex fluids such as bacterial community biofilms and depleting colloidal gels.

# Bibliography

1. Palmer A, Xu J, Wirtz D: **High-frequency viscoelasticity of crosslinked actin filament networks measured by diffusing wave spectroscopy.** *Rheologica Acta* 1998, **37**(2):97-106.
2. Xu J, Tseng Y, Carriere CJ, Wirtz D: **Microheterogeneity and microrheology of wheat gliadin suspensions studied by multiple-particle tracking.** *Biomacromolecules* 2001, **3**(1):92-99.
3. Dasgupta BR, Tee S-Y, Crocker JC, Frisken BJ, Weitz DA: **Microrheology of polyethylene oxide using diffusing wave spectroscopy and single scattering.** *Physical Review E* 2002, **65**(5):051505.
4. Larsen TH, Furst EM: **Microrheology of the liquid-solid transition during gelation.** *Physical Review Letters* 2008, **100**:146001.
5. Willenbacher N, Oelschlaeger C: **Dynamics and structure of complex fluids from high frequency mechanical and optical rheometry.** *Current Opinion in Colloid & Interface Science* 2007, **12**(1):43-49.
6. Hassan PA, Bhattacharya K, Kulshreshtha SK, Raghavan SR: **Microrheology of wormlike micellar fluids from the diffusion of colloidal probes.** *The Journal of Physical Chemistry B* 2005, **109**(18):8744-8748.
7. Chae BS, Furst EM: **Probe surface chemistry dependence and local polymer network structure in F-actin microrheology.** *Langmuir* 2005, **21**(7):3084-3089.
8. Apgar J, Tseng Y, Fedorov E, Herwig MB, Almo SC, Wirtz D: **Multiple-particle tracking measurements of heterogeneities in**

- solutions of actin filaments and actin bundles.** *Biophysical Journal* 2000, **79**(2):1095-1106.
9. Tseng Y, Kole TP, Wirtz D: **Micromechanical mapping of live cells by multiple-particle-tracking microrheology.** *Biophysical Journal* 2002, **83**:3162–3176.
  10. Slopek RP, McKinley HK, Henderson CL, Breedveld V: **In situ monitoring of mechanical properties during photopolymerization with particle tracking microrheology.** *Polymer* 2006, **47**(7):2263-2268.
  11. Mason TG, Weitz DA: **Optical measurements of frequency-dependent linear viscoelastic moduli of complex fluids.** *Physical Review Letters* 1995, **74**(7):1250.
  12. Mason TG, Gang H, Weitz DA: **Rheology of complex fluids measured by dynamic light scattering.** *Journal of Molecular Structure* 1996, **383**(1-3):81-90.
  13. Mason TG, Gang H, Weitz DA: **Diffusing-wave-spectroscopy measurements of viscoelasticity of complex fluids.** *Journal of Optical Society America A* 1997, **14**(1):139-149.
  14. Xu J, Viasnoff V, Wirtz D: **Compliance of actin filament networks measured by particle-tracking microrheology and diffusing wave spectroscopy.** *Rheologica Acta* 1998, **37**(4):387-398.
  15. Breedveld V: **Microrheology as a tool for high-throughput screening.** *Journal of Materials Science* 2003, **38**:4461 – 4470.
  16. Hall-Stoodley L, Costerton JW, Stoodley P: **Bacterial biofilms: from the natural environment to infectious diseases.** *Nature Reviews Microbiology* 2004, **2**(2):95-108.
  17. Shaw T, Winston M, Rupp CJ, Klapper I, Stoodley P: **Commonality**

- of elastic relaxation times in biofilms.** *Physical Review Letters* 2004, **93**:098102.
18. Rasmussen B: **Filamentous microfossils in a 3,235-million-year-old volcanogenic massive sulphide deposit.** *Nature* 2000, **405**(6787):676-679.
  19. Donlan RM, Costerton JW: **Biofilms: survival mechanisms of clinically relevant microorganisms.** *Clinical Microbiology Review* 2002, **15**(2):167-193.
  20. Busscher HJ, van der Mei HC: **Microbial adhesion in flow displacement systems.** *Clinical Microbiology Review* 2006, **19**(1):127-141.
  21. Donlan RM: **Role of biofilms in antimicrobial resistance.** *ASAIO Journal* 2000, **46**(6):S47-S52.
  22. Yebra DM, Kiil S, Weinell CE, Dam-Johansen K: **Parametric study of Tin-free antifouling model paint behavior using rotary experiments.** *Industrial and Engineering Chemical Research* 2006, **45**(5):1636-1649.
  23. Xu H, Liu Y: **Control and cleaning of membrane biofouling by energy uncoupling and cellular communication.** *Environmental Science and Technology* 2011, **45**(2):595-601.
  24. Flemming HC: **Biofouling in water systems - cases, causes and countermeasures.** *Applied Microbiological Biotechnology* 2002, **59**(6):629-640.
  25. Ivanovic I, Leiknes TO: **The biofilm membrane bioreactor (BF-MBR)—a review.** *Desalination and Water Treatment* 2012, **37**(1-3):288-295.
  26. Kumar CG, Anand SK: **Significance of microbial biofilms in food**

- industry: a review.** *International Journal of Food Microbiology* 1998, **42**(1–2):9-27.
27. Bryers JD: **Medical biofilms.** *Biotechnology and Bioengineering* 2008, **100**(1):1-18.
28. Lim T-K, Murakami T, Tsuboi M, Yamashita K, Matsunaga T: **Preparation of a colored conductive paint electrode for electrochemical inactivation of bacteria.** *Biotechnology and Bioengineering* 2003, **81**(3):299-304.
29. van der Borden AJ, van der Werf H, van der Mei HC, Busscher HJ: **Electric current-induced detachment of Staphylococcus epidermidis biofilms from surgical stainless steel.** *Applied and Environmental Microbiology* 2004, **70**(11):6871-6874.
30. Hong SH, Jeong J, Shim S, Kang H, Kwon S, Ahn KH, Yoon J: **Effect of electric currents on bacterial detachment and inactivation.** *Biotechnology and Bioengineering* 2008, **100**(2):379-386.
31. Poortinga AT, Smit J, van der Mei HC, Busscher HJ: **Electric field induced desorption of bacteria from a conditioning film covered substratum.** *Biotechnology and Bioengineering* 2001, **76**(4):395-399.
32. Nakayama T, Wake H, Ozawa K, Kodama H, Nakamura N, Matsunaga T: **Use of a Titanium Nitride for electrochemical inactivation of marine bacteria.** *Environmental Science and Technology* 1998, **32**(6):798-801.
33. Pavlovsky L, Younger JG, Solomon MJ: **In situ rheology of Staphylococcus epidermidis bacterial biofilms.** *Soft Matter* 2013, **9**(1):122-131.
34. Lee S-H, Grier DG: **Holographic microscopy of holographically**

- trapped three-dimensional structures.** *Optical Express* 2007, **15**(4):1505-1512.
35. Klapper I, Rupp CJ, Cargo R, Purvedorj B, Stoodley P: **Viscoelastic fluid description of bacterial biofilm material properties.** *Biotechnology and Bioengineering* 2002, **80**(3):289-296.
36. Stewart EJ, Satorius AE, Younger JG, Solomon MJ: **Role of environmental and antibiotic stress on Staphylococcus epidermidis biofilm microstructure.** *Langmuir* 2013, **29**(23):7017-7024.
37. Aravas N, Laspidou CS: **On the calculation of the elastic modulus of a biofilm streamer.** *Biotechnology and Bioengineering* 2008, **101**(1):196-200.
38. Stoodley P, Cargo R, Rupp C, Wilson S, I; K: **Biofilm material properties as related to shear-induced deformation and detachment phenomena.** *Journal of Industrial Microbiology and Biotechnology* 2002, **29**:361 – 367.
39. Stoodley P, Lewandowski Z, Boyle JD, Lappin-Scott HM: **Oscillation characteristics of biofilm streamers in turbulent flowing water as related to drag and pressure drop.** *Biotechnology and Bioengineering* 1998, **57**(5):536-544.
40. Stoodley P, Lewandowski Z, Boyle JD, Lappin-Scott HM: **Structural deformation of bacterial biofilms caused by short-term fluctuations in fluid shear: An in situ investigation of biofilm rheology.** *Biotechnology and Bioengineering* 1999, **65**(1):83-92.
41. Huang Z, McLamore ES, Chuang HS, Zhang W, Wereley S, Leon JLC, Banks MK: **Shear-induced detachment of biofilms from**

- hollow fiber silicone membranes.** *Biotechnology and Bioengineering* 2013, **110**(2):525-534.
42. Towler BW, Rupp CJ, Cunningham AB, Stoodley P: **Viscoelastic properties of a mixed culture biofilm from rheometer creep analysis.** *Biofouling* 2003, **19**(5):279-285.
43. Liu Y, Tay J-H: **The essential role of hydrodynamic shear force in the formation of biofilm and granular sludge.** *Water Research* 2002, **36**(7):1653-1665.
44. Vieira MJ, Melo LF, Pinheiro MM: **Biofilm formation: Hydrodynamic effects on internal diffusion and structure.** *Biofouling* 1993, **7**(1):67-80.
45. Paris T, Skali-Lami S, Block J-C: **Effect of wall shear rate on biofilm deposition and grazing in drinking water flow chambers.** *Biotechnology and Bioengineering* 2007, **97**(6):1550-1561.
46. Rogers SS, van der Walle C, Waigh TA: **Microrheology of bacterial biofilms in vitro: Staphylococcus aureus and Pseudomonas aeruginosa.** *Langmuir* 2008, **24**(23):13549-13555.
47. Kang H, Shim S, Lee SJ, Yoon J, Ahn KH: **Bacterial translational motion on the electrode surface under anodic electric field.** *Environmental Science and Technology* 2011, **45**(13):5769-5774.
48. Kang H, Ahn KH, Lee SJ: **Rheological properties of dilute polymer solutions determined by particle tracking microrheology and bulk rheometry.** *Korea-Australia Rheology Journal* 2010, **22**(1):11-19.
49. Waigh TA: **Microrheology of complex fluids.** *Reports on Progress in Physics* 2005, **68**:685-742.
50. Han Y, Alsayed AM, Nobili M, Zhang J, Lubensky TC, Yodh AG:



- Brownian motion of an ellipsoid.** *Science* 2006, **314**(5799):626-630.
51. Dibble CJ, Kogan M, Solomon MJ: **Structure and dynamics of colloidal depletion gels: coincidence of transitions and heterogeneity.** *Physical Review E* 2006, **74**(4 Pt 1):041403-041403.
52. Drury JL, Mooney DJ: **Hydrogels for tissue engineering: scaffold design variables and applications.** *Biomaterials* 2003, **24**(24):4337-4351.
53. Helgeson ME, Moran SE, An HZ, Doyle PS: **Mesoporous organohydrogels from thermogelling photocrosslinkable nanoemulsions.** *Nature Materials* 2012, **advance online publication.**
54. Ingham B, Dickie S, Nanjo H, Toney MF: **In situ USAXS measurements of titania colloidal paint films during the drying process.** *Journal of Colloid and Interface Science* 2009, **336**(2):612-615.
55. Koh YK, Wong CC: **In situ monitoring of structural changes during colloidal self-assembly.** *Langmuir* 2005, **22**(3):897-900.
56. Lu Y, Ganguli R, Drewien CA, Anderson MT, Brinker CJ, Gong W, Guo Y, Soyez H, Dunn B, Huang MH *et al*: **Continuous formation of supported cubic and hexagonal mesoporous films by sol-gel dip-coating.** *Nature* 1997, **389**(6649):364-368.
57. Eberle APR, Wagner NJ, Castañeda-Priego R: **Dynamical arrest transition in nanoparticle dispersions with short-range interactions.** *Physical Review Letters* 2011, **106**(10):105704.
58. Hsiao LC, Newman RS, Glotzer SC, Solomon MJ: **Role of isostaticity and load-bearing microstructure in the elasticity of yielded colloidal gels.** *Proceedings of the National Academy of Sciences* 2012.

59. Koumakis N, Petekidis G: **Two step yielding in attractive colloids: transition from gels to attractive glasses.** *Soft Matter* 2011, **7**(6).
60. Rajaram B, Mohraz A: **Microstructural response of dilute colloidal gels to nonlinear shear deformation.** *Soft Matter* 2010, **6**(10):2246-2259.
61. Ramakrishnan S, Gopalakrishnan V, Zukoski CF: **Clustering and mechanics in dense depletion and thermal gels.** *Langmuir* 2005, **21**(22):9917-9925.
62. Sprakel J, Lindström SB, Kodger TE, Weitz DA: **Stress enhancement in the delayed yielding of colloidal gels.** *Physical Review Letters* 2011, **106**(24):248303.
63. Zaccarelli E, Poon WCK: **Colloidal glasses and gels: The interplay of bonding and caging.** *Proceedings of the National Academy of Sciences* 2009, **106**(36):15203-15208.
64. Pham KN, Puertas AM, Bergenholtz J, Egelhaaf SU, Moussaïd A, Pusey PN, Schofield AB, Cates ME, Fuchs M, Poon WCK: **Multiple glassy states in a simple model system.** *Science* 2002, **296**(5565):104-106.
65. Rajaram B, Mohraz A: **Dynamics of shear-induced yielding and flow in dilute colloidal gels.** *Physical Review E* 2011, **84**(1):011405.
66. Masschaele K, Franssaer J, Vermant J: **Flow-induced structure in colloidal gels: direct visualization of model 2D suspensions.** *Soft Matter* 2011, **7**(17):7717-7726.
67. Kegel WK, van Blaaderen A: **Direct observation of dynamical heterogeneities in colloidal hard-sphere suspensions.** *Science* 2000, **287**(5451):290-293.
68. Chen Y-L, Schweizer KS: **Microscopic theory of gelation and**

- elasticity in polymer--particle suspensions.** *The Journal of Chemical Physics* 2004, **120**(15):7212-7222.
69. Chung B, Ramakrishnan S, Bandyopadhyay R, Liang D, Zukoski CF, Harden JL, Leheny RL: **Microscopic dynamics of recovery in sheared depletion gels.** *Physical Review Letters* 2006, **96**(22):228301.
70. Zacccone A, Wu H, Del Gado E: **Elasticity of arrested short-ranged attractive colloids: homogeneous and heterogeneous glasses.** *Physical Review Letters* 2009, **103**(20):208301.
71. Puertas AM, Fuchs M, Cates ME: **Mode coupling and dynamical heterogeneity in colloidal gelation: a simulation study.** *The Journal of Physical Chemistry B* 2005, **109**(14):6666-6675.
72. Dibble CJ, Kogan M, Solomon MJ: **Structural origins of dynamical heterogeneity in colloidal gels.** *Physical Review E* 2008, **77**(5):050401.
73. Kilfoil ML, Pashkovski EE, Masters JA, Weitz DA: **Dynamics of weakly aggregated colloidal particles.** *Philosophical Transactions of the Royal Society of London Series A: Mathematical, Physical and Engineering Sciences* 2003, **361**(1805):753-766.
74. Pang CM, Hong P, Guo H, Liu W-T: **Biofilm formation characteristics of bacterial isolates retrieved from a reverse osmosis membrane.** *Environmental Science and Technology* 2005, **39**(19):7541-7550.
75. Vigeant M, Ford R: **Interactions between motile Escherichia coli and glass in media with various ionic strengths, as observed with a three-dimensional-tracking microscope.** *Appl Environ Microbiol* 1997, **63**(9):3474-3479.

76. Gopalakrishnan V, Zukoski CF: **Yielding behavior of thermo-reversible colloidal gels.** *Langmuir* 2007, **23**(15):8187-8193.
77. Doi M, Edwards SF: **The theory of polymer dynamics.** 1986.
78. Oppong FK, Rubatat L, Frisken BJ, Bailey AE, de Bruyn JR: **Microrheology and structure of a yield-stress polymer gel.** *Physical Review E* 2006, **73**(4).
79. Mason TG: **Estimating the viscoelastic moduli of complex fluids using the generalized Stokes–Einstein equation.** *Rheologica Acta* 2000, **39**(4):371-378.
80. Macosko CW: **Rheology principles, measurements, and applications.** 1994 VCH Publishers, Inc.
81. Kob W, Donati C, Plimpton SJ, Poole PH, Glotzer SC: **Dynamical heterogeneities in a supercooled Lennard-Jones liquid.** *Physical Review Letters* 1997, **79**(15):2827-2830.
82. Savin T, Doyle PS: **Static and dynamic errors in particle tracking microrheology.** *Biophysical Journal* 2005, **88**(1):623-638.
83. Crocker JC: **Methods of digital video microscopy for colloidal studies.** *Journal of Colloid and Interface Science* 1996, **179**:298–310.
84. Deziel E, Comeau Y, Villemur R: **Initiation of biofilm formation by *Pseudomonas aeruginosa* 57RP correlates with emergence of hyperpiliated and highly adherent phenotypic variants deficient in swimming, swarming, and twitching motilities.** *Journal of Bacteriology* 2001, **183**(4):1195-1204.
85. Scheaffer RL, Mulekar M, McClave JT: **Probability and statistics for engineers** *Wadsworth, INC* 1995.
86. Hu H, Larson RG: **One-step preparation of highly monodisperse micron-size particles in organic solvents.** *Journal of the American*

- Chemical Society* 2004, **126**(43):13894-13895.
87. Kogan M, Dibble CJ, Rogers RE, Solomon MJ: **Viscous solvent colloidal system for direct visualization of suspension structure, dynamics and rheology.** *Journal of Colloid and Interface Science* 2008, **318**(2):252-263.
  88. Cardinaux F, Gibaud T, Stradner A, Schurtenberger P: **Interplay between spinodal decomposition and glass formation in proteins exhibiting short-range attractions.** *Physical Review Letters* 2007, **99**(11):118301.
  89. Wang Y, Hansen FY, Peters GH, Hassager O: **Proof of the identity between the depletion layer thickness and half the average span for an arbitrary polymer chain.** *The Journal of Chemical Physics* 2008, **129**(7):-.
  90. Lekkerkerker HNW, Poon WCK, Pusey PN, Stroobants A, Warren PB: **Phase behaviour of colloid + polymer mixtures.** *Europhysics Letters* 1992, **20**(6):559.
  91. Shereda LT, Larson RG, Solomon MJ: **Local stress control of spatiotemporal ordering of colloidal crystals in complex flows.** *Physical Review Letters* 2008, **101**(3):038301.
  92. Lu Q, Solomon MJ: **Probe size effects on the microrheology of associating polymer solutions.** *Physical Review E* 2002, **66**(6):061504.
  93. Lukić B, Jeney S, Tischer C, Kulik AJ, Forró L, Florin EL: **Direct observation of nondiffusive motion of a brownian particle.** *Physical Review Letters* 2005, **95**(16):160601.
  94. Li G, Tam L-K, Tang JX: **Amplified effect of Brownian motion in bacterial near-surface swimming.** *Proceedings of the National*

- Academy of Sciences* 2008, **105**(47):18355-18359.
95. Frymier PD, Ford RM, Berg HC, Cummings PT: **Three-dimensional tracking of motile bacteria near a solid planar surface.** *Proceedings of the National Academy of Sciences of the United States of America* 1995, **92**(13):6195-6199.
96. Poortinga AT, Bos R, Busscher HJ: **Controlled electrophoretic deposition of bacteria to surfaces for the design of biofilms.** *Biotechnology and Bioengineering* 2000, **67**(1):117-120.
97. Trau M, Saville DA, Aksay IA: **Assembly of colloidal crystals at electrode interfaces.** *Langmuir* 1997, **13**(24):6375-6381.
98. Trau M, Saville DA, Aksay IA: **Field-induced layering of colloidal crystals.** *Science* 1996, **272**(5262):706-709.
99. Bard AJ, Faulkner LR: **Electrochemical methods: fundamentals and applications.** 2001.
100. Bos R, Mei HC, Busscher HJ: **Physico-chemistry of initial microbial adhesive interactions - its mechanisms and methods for study.** *FEMS Microbiology Reviews* 1999, **23**(2):179-230.
101. Poortinga AT, Bos R, Norde W, Busscher HJ: **Electric double layer interactions in bacterial adhesion to surfaces.** *Surface Science Reports* 2002, **47**(1):1-32.
102. Seviour T, Pijuan M, Nicholson T, Keller J, Yuan Z: **Understanding the properties of aerobic sludge granules as hydrogels.** *Biotechnology and Bioengineering* 2009, **102**(5):1483-1493.
103. Ganesan M, Stewart EJ, Szafranski J, Satorius AE, Younger JG, Solomon MJ: **Molar mass, entanglement, and associations of the biofilm polysaccharide of Staphylococcus epidermidis.** *Biomacromolecules* 2013, **14**(5):1474-1481.

104. Geresh S, Adin I, Yarmolinsky E, Karpasas M: **Characterization of the extracellular polysaccharide of *Porphyridium* sp.: molecular weight determination and rheological properties.** *Carbohydrate Polymers* 2002, **50**(2):183-189.
105. Wloka M, Rehage H, Flemming HC, Wingender J: **Structure and rheological behaviour of the extracellular polymeric substance network of mucoid *Pseudomonas aeruginosa* biofilms.** *Biofilms* 2005, **2**(04):275-283.
106. Houari A, Picard J, Habarou H, Galas L, Vaudry H, Heim V, Martino PD: **Rheology of biofilms formed at the surface of NF membranes in a drinking water production unit.** *Biofouling: The Journal of Bioadhesion and Biofilm Research* 2008, **24**(4):235 - 240.
107. Vinogradov AM, Winston M, Rupp CJ, Stoodley P: **Rheology of biofilms formed from the dental plaque pathogen *Streptococcus mutans*.** *Biofilms* 2004, **1**:49-56.
108. Wloka M, Rehage H, Flemming HC, Wingender J: **Rheological properties of viscoelastic biofilm extracellular polymeric substances and comparison to the behavior of calcium alginate gels.** *Colloid and Polymer Science* 2004, **282**(10):1067-1076.
109. Dogsa I, Kriechbaum M, Stopar D, Laggner P: **Structure of bacterial extracellular polymeric substances at different pH values as determined by SAXS.** *Biophysical Journal* 2005, **89**(4):2711-2720.
110. Gotoh T, Kaneda Y: **Effect of an infinite plane wall on the motion of a spherical Brownian particle.** *The Journal of Chemical Physics* 1982, **76**(6):3193-3197.
111. Zembrzycki K, Błoński S, Kowalewski TA: **Analysis of wall effect**

- on the process of diffusion of nanoparticles in a microchannel.** *Journal of Physics: Conference Series* 2012, **392**(1):012014.
112. Rocha C, Teixeira JA, Hilliou L, Sampaio P, Gonçalves MP: **Rheological and structural characterization of gels from whey protein hydrolysates/locust bean gum mixed systems.** *Food Hydrocolloids* 2009, **23**(7).
113. Varadan P, Solomon MJ: **Direct visualization of long-range heterogeneous structure in dense colloidal gels.** *Langmuir* 2002, **19**(3):509-512.
114. Larsen T, Schultz K, Furst EM: **Hydrogel microrheology near the liquid-solid transition.** 2008, **20**(3):165-173.
115. Schultz KM, Furst EM: **Microrheology of biomaterial hydrogelators.** *Soft Matter* 2012, **8**(23):6198-6205.
116. Hopkins P, Fortini A, Archer AJ, Schmidt M: **The van Hove distribution function for Brownian hard spheres: Dynamical test particle theory and computer simulations for bulk dynamics.** *The Journal of Chemical Physics* 2010, **133**(22):-.
117. Saltzman EJ, Schweizer KS: **Non-Gaussian effects, space-time decoupling, and mobility bifurcation in glassy hard-sphere fluids and suspensions.** *Physical Review E* 2006, **74**(6 Pt 1):061501.
118. Potanin AA, De Rooij R, Van den Ende D, Mellema J: **Microrheological modeling of weakly aggregated dispersions.** *The Journal of Chemical Physics* 1995, **102**(14):5845-5853.
119. Guo H, Ramakrishnan S, Harden JL, Leheny RL: **Connecting nanoscale motion and rheology of gel-forming colloidal suspensions.** *Physical Review E* 2010, **81**(5):050401.
120. Kobelev V, Schweizer KS: **Nonlinear elasticity and yielding of**



- depletion gels.** *Journal of Chemical Physics* 2005, **123**(16):164902.
121. Shah SA, Chen YL, Ramakrishnan S, Schweizer KS, Zukoski CF:  
**Microstructure of dense colloid–polymer suspensions and gels.**  
*Journal of Physics: Condensed Matter* 2003, **15**(27):4751.

# 국문 요약

## 변형에 의한 복잡유체의 동적불균일성 및 미세유변학적 특성에 관한 연구

강희경

서울대학교 대학원

화학생명공학부

복잡유체란 두 가지 상 사이에서 공존하는 이원 혼합물로서, 대표적으로 고체-유체의 조합인 입자현탁액, 액체-기체의 조합인 거품, 액체-액체의 조합인 유화액을 들 수 있다. 이러한 복잡유체에는 현재 잉크젯프린팅, 스크린프린팅, 건조공정 등 IT산업에서 활발하게 이용되고 있는 대부분의 물질이 포함된다. 이들은 상공존에 의해서 야기되는 기하학적 제한 때문에 외부에서 가해지는 응력 또는 변형에 의해 특이한 역학반응을 보인다고 알려져 있다. 현재 대부분의 공정은 정지상태가 아닌 흐름상태로 진행되기 때문에 복잡유체의 유변학적 물성의 측정에 대한 관심이 높아지고 있다. 복잡유체의 유변학적 물성은 무질서한 배열, 케이징, 입자의 뭉침과 같은 수많은 길이 단위에서의 구조적 특성에 기인할 뿐만 아니라, 구조적 특성으로부터 기인되는 유체의 불균일한 동역학과도 깊은 연관성을 보인다. 본 연구에서는 복잡유체 중 박테리아 공동체로부터 형성된 생물막과 감수폴

리머에 의해 형성된 콜로이드젤을 실험 물질로 선정하였다. 그리고 이들의 국부적 유변학적 물성을 측정하고, 동시에 직접 관찰을 통하여 동적 불균일성을 측정하기 위하여 기존의 유변물성측정장비 대신에 입자 추적 미세유변학적 방법론을 도입하였다. 기존의 방법론을 이용할 경우 야기되는 측정과정에서 물질의 구조체가 깨어질 수 있고, 또한 마이크론 단위에서 국부적인 구조의 차이 규명이 어려운 점을 미세유변학을 이용하여 보완하였다.

먼저, 생물막은 수분만 있다면 매우 광범위하고 비선택적으로 존재하며 의학적, 경제적으로 여러 가지 문제를 야기시킬 수 있다. 예를 들어, 산업시설에서 물질의 흐름을 방해하여 경제적 손실을 야기하고, 체내에 이식하는 의료장비에 형성될 경우 세균감염을 일으켜 인체에 치명적인 영향을 끼칠 수 있다. 따라서 생물막의 형성과정을 제어하고, 최종적으로 표면으로부터 이를 제거할 방법에 관한 많은 연구가 이루어지고 있다. 생물막은 먼저 미생물이 표면에 흡착하고, 이 미생물들이 세포외고분자물질을 내놓으면서 구조체를 형성하게 된다. 또한 생물막은 미생물과 고분자, 기포가 얽혀서 생기는 매우 불균일한 물질로서 이를 제어하기 위해서는 생물막의 국부적인 특성을 규명해야 할 필요가 있다. 이에 입자추적 미세유변학을 이용하여서 생물막이 형성되는 도중에 주입된 형광입자의 개별적인 움직임을 추적하여 동역학을 측정하였다. 이를 생물막이 형성되는 과정에서 가해지는 전단응력을 증가시키면서 반복하였을 때, 측정한 동적 불균일성이 감소하는 현상을 발견하였다. 낮은 벽전단 변형률에서 성장한 생물막의 국부적인  $G'$  과  $G''$ 을 구했을 때, 마이크론 길이 단위에서 형광입자가 생물막의 어느 위치에 있느냐에 따라서 점탄성계수의 크기와 개형이 달라졌으며, 이는 빈

공간과 네트워크 구조의 밀도가 다른 2가지 종류의 세포외고분자물질 그룹으로 분류할 수 있었다. 반면에, 높은 벽전단 변형률에서, 평균제곱변위는 낮은 벽전단 변형률을 가했을 때보다 더 좁게 분포하며, 이로부터 구조적으로 촘촘한 EPS 구조체를 형성함을 유추할 수 있었다. 이는 성장하면서 받는 전단 응력이 증가할 수록 EPS에 의해 형성되는 젤 네트워크 구조가 얇아지면서 뽀뽀해지고, 빈 공간의 비율이 감소하여 상대적으로 덜 불균일한 구조를 형성한다고 볼 수 있다. 이처럼 생물막은 성장과정에서 가해지는 전단응력을 달리했을 때, 구조적인 특징이 달라지고, 이로부터 동적 불균일성이 야기되는 시스템을 정량적으로 밝혀내었다.

두 번째로, 콜로이드 젤이란 특정한 용매에 분산된 입자계 현탁액에 짧은 거리에서 인력을 줄 수 있는 폴리스타이렌과 같은 작은 고분자를 첨가하여 네트워크 구조가 형성된 젤을 말한다. 감수 인력에 의해 형성된 콜로이드 젤에 높은 변형률로 변형의 크기를 달리하여서 전단 변형을 가하고, 직후의 젤의 동역학을 입자추적 미세유변학을 이용하여 측정하였다. 그 결과, 변형이 커짐에 따라서 입자들은 부확산적 운동을 보이면서 평균제곱변위가 증가하였다. 이 때, 콜로이드 젤에 적은 전단 변형이 가해 졌을 때, 강한 결합을 형성한 전체적인 네트워크구조는 유지된 채로 약한 결합으로 연결되어 있던 작은 길이 단위의 응집체가 깨져나와서 두 가지의 분리된 상을 형성하는 현상을 발견하였다. 이 때, 두 가지 상 중에서 느리게 움직이는 부분이 강한 뼈대를 형성하면서 물질의 잔여 응력에 기여한다고 보았다. 이를 토대로, 우리는 오직 느린 입자들의 국소 길이만을 고려하여 이론적 점탄성계수를 계산하고, 이를 기존의 회전형 유변물성 측정 장치로

구한 값과 비교하였다. 특히 동적 불균일성이 확연하게 나타나는 큰 변형이 가해졌을 때, 이론적으로 그리고 실험적으로 구한  $G'$ 이 더 부합함을 확인하였다.

본 연구에서 콜로이드젤과 생물막과 같은 복잡유체의 동역학을 분석하여 전단 응력이 가해지고 난 후의 동적 불균일성을 측정하고, 이로부터 구조적 불균일성을 추측할 수 있는 근거를 찾을 수 있었다. 또한 복잡유체의 국지적 유변 물성에 동적 불균일성이 어떤 역할을 하는지 보고하였다.

이름: 강희경

학번: 2007-21170

## Curriculum Vitae

# Heekyoung Kang

---

### Contact information

Current address: #302-618, School of Chemical and Biological Engineering,  
Seoul National University, Gwanak-ro, Gwanak-gu,  
Seoul 151-744, South Korea

Permanent address: Phone: (+82)-2-880-1879  
Fax: (+82)-2-871-8016  
Email: snowdrop0925@naver.com

---

### Education

#### **Ph.D. candidate**

Mar 2007 – present

Chemical and Biological Engineering, Seoul National University, Korea

Advisor: Prof. Kyung Hyun Ahn

#### **BS**

Mar 2003 –Feb 2007

Chemical and Biological Engineering, Seoul National University, Korea

### Publications

1. **Heekyoung Kang**, Lilian Hisiao, Kyung Hyun Ahn, Michael J. Solomon, The role of dynamical heterogeneity in nonlinear rheology of colloidal gels, *manuscript in preparation*.
2. **Heekyoung Kang**, Soojun Shim, Jeyong Yoon, Kyung Hyun Ahn, The dynamics and local viscoelastic behavior of biofilms determined by particle tracking microrheology, *manuscript in preparation*.
3. **Heekyoung Kang**, Soojin Shim, Jeyong Yoon, and Kyung Hyun Ahn, Bacterial Bacterial Translational Motion on the Electrode Surface under Anodic Electric Field,

- Environmental Science and Technology, 45 (13), 5769–5774, 2011
4. **Heekyoung Kang**, Kyung Hyun Ahn, and Seong Jong Lee, Rheological Properties of Dilute Polymer Solutions Determined by Particle Tracking Microrheology and Bulk Rheometry, *Korea-Australia Rheology Journal*, Korea-Australia Rheology Journal, Vol. 22, No. 1, March 2010 pp. 11-19
  5. Aayush A. Shah, **Heekyoung Kang**, Kevin L. Kohlstedt, Kyung Hyun Ahn, Sharon C. Glotzer, Charles W. Monroe, and Michael J. Solomon, Liquid Crystal Order in Colloidal Suspensions of Spheroidal Particles by Direct Current Electric Field Assembly, *Small*, 8, No. 10, 1551–1562, 2012.
  6. Seok Hoon Hong, Joonseon Jeong, Soojin Shim, **Heekyoung Kang**, Sunghoon Kwon, Kyung Hyun Ahn, and Jeyong Yoon, Effect of Electric Currents on Bacterial Detachment and Inactivation, *Biotechnology and Bioengineering* 100(2): 379-386, 2008.

#### Conference Presentations

1. **Heekyoung Kang**, Michael J. Solomon, Kyung Hyun Ahn, Stain-dependent dynamics and rheology of colloidal gels in shear flow, *World of Congress of Chemical Engineering, Seoul, Korea (Aug. 18-23, 2013)*, **Podium Presentation**.
2. **Heekyoung Kang**, Soojin Shim, Jeyong Yoon, Kyung Hyun Ahn, Seung Jong Lee, Heterogeneous microstructure of biofilm probed by particle tracking microrheology, *The Society of Rheology, Santafe, USA (Oct. 24-28, 2010)*, **Podium Presentation**
3. **Heekyoung Kang**, Soojun Shim, Jeyong Yoon, Kyung Hyun Ahn, Quantification translational displacement of bacteria near the anodic electrode surface , *The 5<sup>th</sup> International Workshop for Far East Asian Young Rheologists, Pusan, Korea (Jan. 25-27, 2010)*, **Podium Presentation**.
4. **Heekyoung Kang**, Soojin Shim, Jeyong Yoon, Kyung Hyun Ahn, Seung Jong Lee, Local viscoelastic behavior of biofilm formed from *Pseudomonas aeruginosa* using particle tracking microrheology, *Processes in Biofilms: Fundamentals to Applications*, Davis, USA (Sep. 13-16, 2009), **Podium Presentation**.
5. **Heekyoung Kang**, Soojin Shim , Kyung Hyun Ahn and Jeyong Yoon, Quantitative characterization of bacterial motion on anodically polarized surface, *Processes in Biofilms: Fundamentals to Applications*, Davis, USA (Sep. 13-16, 2009), **Poster**

### ***Presentation.***

6. **Heekyoung Kang**, Soojin Shim, Jeyoung Yoon, Kyung Hyun Ahn, Seung Jong Lee, Characterizing heterogeneous microstructure of biofilm using particle tracking microrheology, *The 4<sup>th</sup> International Workshop for Far East Asian Young Rheologists*, Nakhon Ratchasima, Thailand, (Jan. 25-27, 2009), ***Podium Presentation.***
7. **Heekyoung Kang**, Kyung Hyun Ahn, Seung Jong Lee, Characterizing microstructure of biofilm formed from *Pseudomonas aeruginosa* using particle tracking microrheology, *The 15<sup>th</sup> International Congress on Rheology*, Monterey, USA (Aug. 3-8, 2008), ***Poster Presentation.***
8. **Heekyoung Kang**, Soojin Shim, Nahn Ju Kim, Jeyoung Yoon, Kyung Hyun Ahn, and Seung Jong Lee, Characterizing biofilm formed from *Pseudomonas aeruginosa* using particle tracking microrheology, *The 13<sup>th</sup> International Congress of Biorheology & 6<sup>th</sup> Congress on Clinical Hemorheology*, State College, USA (Jul. 9-13, 2008), ***Poster Presentation.***
9. **Heekyoung Kang**, Kyung Hyun Ahn, Seung Jong Lee, Characterizing microstructure of extracellular polymeric substances (EPS) using particle tracking microrheology, *The 3<sup>rd</sup> International Workshop for Far East Asian Young Rheologists*, Shanghai, China (Jan. 25-27, 2008), ***Podium Presentation***
10. **Heekyoung Kang**, Yoonjae Yim, Kyung Hyun Ahn, Seung Jong Lee, Measuring viscoelastic behavior of dilute suspensions with particle tracking microrheology, *The 2<sup>nd</sup> International Workshop for Far East Asian Young Rheologists*, Kyoto, Japan (Jan. 26-28, 2007), ***Podium Presentation.***

### **Awards**

1. Best Oral Presentation at Processes in Biofilms: Fundamentals to Application Conference, Sep 13-16, 2009, UC Davis, USA.
2. Academic Achievement Scholarship (for graduate course): Seoul National University, 2007-2009.
3. Academic Achievement Scholarship (for undergraduate course): Seoul National University, 2003-2006.



### **Skills**

1. Particle tracking microrheological experimental skills – up/light inverted microscope, CCD camera, Confocal microscope
2. Rheometry of polymer solutions (ARES, AR-G2)
3. Image processing (using IDL language)
4. Handling bacterial sample solution to develop biofilm
4. Software: IDL, FORTRAN

### **Other activities**

1. Visiting to Prof. Michael J. Solomon Group, University of Michigan, MI, USA, 2010.10.-2011.9.
2. Teaching/Research Assistant for undergraduate experiment course: Seoul National University, Fluid mechanics, Mar 2007 – Jun 2007
3. Teaching/Research Assistant for undergraduate experiment course: Seoul National University, Basic experiments for chemical physics, Sep 2007 – Dec 2007

### **References**

1. Prof. Kyung Hyun Ahn  
School of Chemical and Biological Engineering, Seoul National University,  
599 Gwanangno, Gwanak-gu, Seoul 151-744, Korea  
**Tel:** 82-2-880-8322  
**Email:** ahnnet@snu.ac.kr
2. Prof. Seung Jong Lee  
School of Chemical and Biological Engineering, Seoul National University,  
599 Gwanangno, Gwanak-gu, Seoul 151-744, Korea  
**Tel:** 82-2-880-7410  
**Email:** sjlee@plaza.snu.ac.kr